Dissertation

submitted to the

Combined Faculty of Natural Sciences and Mathematics

of Heidelberg University, Germany

for the degree of

Doctor of Natural Sciences

Put forward by

Li-Hsin Chen

Born in: Taoyuan, Taiwan

Oral examination: 9th November 2022

Stars and star formation in the Milky Way system

Referees: Prof. Dr. Ralf S. Klessen

Prof. Dr. Eva K. Grebel

Abstract

Dwarf galaxies in the Milky Way (MW) system provide us with important information of the star formation in the early Universe. In particular, extremely metal-poor stars in them are likely to form in the environment that is directly influenced by the first stars. In this thesis, I utilise the semi-analytic code A-SLOTH to study the properties of these dwarf galaxies. A new star formation model that allows tracking of individual stars is implemented. The star formation efficiency is important in determining the stellar mass of ultra-faint galaxies at $z = 0$. To better quantify the goodness-of-fit of the physical models, I develop a new analysis method, which utilises the unsupervised clustering. With this method, the results suggest that the fiducial model cannot reproduce the mean metallicity of the dwarf galaxies. A temporary improvement of the model is implemented and the goodness-of-fit improves by a factor of 2, compared to the fiducial model. I further analyse the location of EMP stars of MW/M31-like systems in the hydrodynamical simulation TNG50. The analysis is based on the spatial and kinematic information of stars. I find that EMP stars reside mostly in the Stellar halo in the galaxy, regardless of the definition of EMP stars. The model and analysis methods introduced in this thesis provide a new framework for future works to understand dwarf galaxy formation and stars that reside in them.

Zusammenfassung

Die kleine Galaxien in das System des Milchstraße bieten uns wichtige Informationen über die Sternentstehung in dem Anfang des Universums an. Extrem metallarme Sterne der kleinen Galaxien formieren wahrscheinlich in der Umgebung, die direkt von den ersten Sterne beeinflusst. In dieser Arbeit verwende ich den semi-analytischen Code A-SLOTH, um die Eigenschaften dieser kleine Galaxien zu untersuchen. Ich habe ein neues Sternentstehungsmodell implementiert, dass eine Verfolgung der einzelnen Sterne möglich ist. Die Sternentstehungseffizienz ist wichtig in Bestimmung der Sternmasse der kleine Galaxien bei $z = 0$. Zur besseren Quantifizierung der Anpassungsgüte der physikalischen Modelle habe ich eine neue Analysemethode entwickelt, die verwendet das unüberwachte Clustering. Mit dieser Methode deuten die Ergebnisse darauf hin, dass die Das Bezugsmodell kann die mittlere Metallizität der Galaxien nicht reproduzieren. Eine temporäre Verbesserung des Modells wird implementiert und die Anpassungsgüte verbessert sich um den Faktor 2 im Vergleich zum Fiducial-Modell. Ich analysiere weiter den Standort von EMP-Sterne der MW/M31 Systems in der hydrodynamischen Simulation TNG50. Die Analyse basiert auf der räumliche und kinetische Information von Sternen. Ich finde, dass EMP-Sterne hauptsächlich in den Stellar halo der Galaxie liegen, unabhängig von der Definition der EMP-Sterne. Die vorgestellten Modell und Analysemethoden in dieser Arbeit bieten einen neuen Rahmen für zukünftige Arbeiten zum Verständnis der Entstehung von kleine Galaxien und Sterne, die in ihnen wohnen.

Contents

Abstract **i**

1 Introduction **1**

1.1 Cosmological context 1

1.1.1 Expansion of the Universe 2

1.1.2 Structure formation 3

1.2 Galaxy formation 3

1.2.1 Gravitational collapse of gas 4

1.2.2 Formation of molecular hydrogen 4

1.2.3 Efficiency of star formation 6

1.2.4 Radiative and kinetic feedback from massive stars 7

1.2.5 Chemical feedback of stars: source of metal production 11

1.3 Stellar population 12

1.3.1 Population III stars 12

1.3.2 Population II/I stars 13

1.4 Observational constraints 14

1.4.1 Milky Way and its satellites 14

1.4.2 Extremely metal-poor stars 15

1.5 Thesis outline 17

2 SMHM relation at redshift 0 **18**

2.1 Motivation 19

2.2 Semi-analytic model: A-SLOTH 20

2.2.1 Dark matter merger trees 20

2.2.2 Population III star formation model 21

2.2.3 Population II star formation model 23
2.2.4 Population II Stellar Feedback 29
2.2.5 Ionising and enriching volumes (internal/external enrichment) 37
2.3 Calibration 38
2.3.1 Observables used in calibration 38
2.3.2 Free parameters in the Pop II star formation model 40
2.4 Results 46
2.4.1 Main output 46
2.4.2 Slope of the Pop II initial mass function 48
2.4.3 LW background and baryonic streaming velocity 49
2.5 Discussion 55
2.5.1 A low-mass plateau in the stellar mass-to-halo mass relation. . 55
2.5.2 Uncertainty in critical masses of haloes 57
2.5.3 Caveats 58
2.6 Summary 59

3 Data analysis with unsupervised clustering 61
3.1 Motivation 62
3.2 Method 63
3.2.1 Observational data 63
3.2.2 Simulated MW satellites 67
3.2.3 Unsupervised clustering algorithm 68
3.2.4 Goodness of fit 68
3.3 Results 69
3.3.1 Application to Gaussian distributions 70
3.3.2 Clustering result and the p-value from our fiducial model . . . 72
3.4 Discussion 75
3.4.1 Properties of the simulated MW satellites 75
3.4.2 p-value vs. properties of the MW-like galaxies 78
3.4.3 Caveats 79
3.5 Summary 80

4 Extremely metal poor stars in TNG50 82
4.1 Motivation 83
4.2 Method 84
4.2.1 The TNG50 simulation 84
4.2.2 MW/M31-like systems in TNG50 85
4.2.3 Morphological decomposition with kinematics 86

4.2.4 EMP stars in TNG50 87
4.3 Results 88
4.3.1 Metallicity distribution function 88
4.3.2 Spatial distribution of EMP stars 90
4.3.3 EMP frequency in different components 94
4.4 Discussion 95
4.5 Summary 97

5 Conclusion and outlook **99**

Acknowledgement **102**

List of publications **103**

Appendices **104**
A List of commonly used acronyms 104
B List of softwares 104

References **105**

List of Tables

1.1 Observed physical properties of the MW at $z = 0$. From top to bottom: virial mass, virial radius, stellar mass, molecular mass, atomic mass, ionised mass, and star formation rate. References: (1) Posti and Helmi (2019), (2) McMillan (2017), (3) Ferrière (2001), (4) Chomiuk and Povich (2011), (5) Licquia and Newman (2015). 14

2.1 Definitions of the variables in the Pop II star formation model. . . . 24
2.2 Number of ionising stars and SNe v.s. $n_{\mathrm{bins,II}}$ 45
2.3 The main parameters in our model and their fiducial values. 45

3.1 Physical quantities of the observed MW satellites used in the analysis. 66
3.2 Example of contingency tables 69

List of Figures

2.1 Schematic plot of Pop II star formation model 25
2.2 Time evolution of mass conversion rate 31
2.3 SMHM relations of different star cluster assumption 33
2.4 MW properties with different parameter values 41
2.5 CSMF, $f_{\rm gal}$, and SMHM relation for the fiducial model 42
2.6 Determination of fiducial values 43
2.7 Main results with individual *Caterpillar* trees 48
2.8 Dependence on Pop II IMF assumption 49
2.9 Dependence on different LW models and baryonic streaming velocities 53
2.10 $M_{\rm crit}$ v.s. redshift 54
2.11 $M_{*,\rm pre\ SNe}$ v.s. $M_*(> z)$ for different $\eta_{\rm II}$ 56

3.1 p-value vs. number of clusters with different unsupervised clustering methods 72
3.2 Example of clustering results from A-SLOTH fiducial model 73
3.3 The p-values from 30 *Caterpillar* trees as individual dataset and the p-value from the Ensemble 74
3.4 Clustering result projected onto the [Fe/H]-M_* space for one *Caterpillar* tree. 75
3.5 p-value v.s. number of clusters from our fiducial model 76
3.6 Normalised, cumulative histogram of the five physical quantities used in the analysis 77
3.7 Individual p-values for 30 *Caterpillar* trees from the fiducial and the improved models 78
3.8 p-value vs. properties of MW-like galaxies from 30 *Caterpillar* trees . 79

4.1 Cartoon plot of the morphological decomposition of the main galaxy . 86
4.2 MDFs of MW analogues in TNG50 89
4.3 Spatial distribution of EMP stars in 16 MW/M31 analogues 90
4.4 Spatial distribution of stars in 16 MW/M31 analogues 91
4.5 Stellar circularity ϵ_{z} v.s the distance from the centre of the galaxy in 16 MW/M31 analogues 92
4.6 Radial profiles of $M_{\mathrm{EMP}}(r)$-to-M_* fraction and $M_{\mathrm{EMP}}(r)$-to-$M_{\mathrm{EMP,all}}$ fraction 93
4.7 Mass fraction of EMP stars in 198 TNG50 MW/M31-like systems in different morphological components 94
4.8 The mass fraction of EMP stars in individual satellites 95
4.9 $M_{\mathrm{EMP,comp}}$-to-$M_{\mathrm{EMP,all}}$ fraction in different morphological components with different metallicity threshold $[\mathrm{Fe/H}]_{\mathrm{th}}$ for $[\mathrm{Fe/H}]_{\mathrm{th}} = -3, -4, -5, -6$ 96
4.10 $M_{\mathrm{EMP,comp}}$-to-$M_{\mathrm{EMP,all}}$ fraction in different morphological components with different metallicity threshold $[\mathrm{Fe/H}]_{\mathrm{th}}$ for $[\mathrm{Fe/H}]_{\mathrm{th}} = -1, -2, -3$ 96

1

Introduction

Our understanding of the Universe starts with the Milky Way (MW), our host galaxy. Long before any theory has been formalised, human had been looking at the sky and discovered many interesting phenomena. With the development of observational technology, we are now able to look beyond the MW and observe the Universe at its different evolutionary stages. However, how exactly the MW along with its satellite galaxies form and evolve to what we observe today remains an unresolved problem. Despite efforts of many decades, new observational discoveries continue to challenge our understanding of galaxy formation and evolution. These new discoveries include but not limited to precise spatial distribution, kinetic information (Gaia Collaboration et al., 2016, 2022b) and elemental abundances (Gaia Collaboration et al., 2022a) of stars in the MW, and the abundance and properties of MW satellite galaxies (Muñoz et al., 2018; Simon, 2019; Battaglia and Nipoti, 2022, and the references therein). This thesis aims to understand the formation of stars in the MW and its satellites from the theoretical perspective.

1.1 Cosmological context

The widely-accepted and mostly used model that describes the composition of the Universe is the Λ Cold Dark Matter (ΛCDM) model. The Universe is homogeneous and isotropic on the large scale and can be divided into three main components: dark energy, dark matter, and baryons. With no observations of it to-date, the dark energy is responsible to explain the accelerating expansion of the Universe. Dark matter is assumed to only interact with other components through gravity and it is the dominant source of providing the gravitational field for galaxy formation. Observational support of the existence of dark matter is the rotational curve of galaxies that cannot be explained with all the baryons combined (Rubin et al., 1980). Baryons refers to all the matter that we can observe, such as stars, gas, and dusts.

1.1.1 Expansion of the Universe

From Einsteins's field equastions, Friedmann (1922) derived the following equations (the Friedmann equations):

$$\begin{aligned} H^2(t) + \frac{kc^2}{a^2} &= \frac{8\pi G\rho}{3} + \frac{\Lambda c^2}{3} \\ \frac{\ddot{a}}{a} &= -\frac{4\pi G}{3}\left(\rho + \frac{3p}{c^2}\right) + \frac{\Lambda c^2}{3} \end{aligned} \tag{1.1}$$

where $H(t) \equiv \dot{a}/a$ is the Hubble parameter, a is the time-dependent scale factor, k is the curvature parameter, G is the gravitational constant, ρ is the density where contribution from both the matter and radiation is considered ($\rho = \rho_m + \rho_r$), p is the pressure, c is the speed of light, and Λ is the cosmological constant. The Universe is in fact expanding, at a rate of $H_0 = 67.8\mathrm{kms}^{-1}\mathrm{Mpc}^{-1}$ currently (Planck Collaboration et al., 2020a). The farther away an object is from us, it is moving away at a higher rate. Since the Universe is expanding, the matter number density evolves inversely proportional to the volume, i.e. $\rho_m = \rho_{0,m}a^{-3}$. The photon energy evolves as a^{-1} because it is inversely proportional to the wavelength, which is stretched by the expansion. Therefore, we can write down the dependence of ρ_r on the scale factor $\rho_r = \rho_{0,r}a^{-4}$.

The critical density is defined that

$$\rho_{\mathrm{crit}} \equiv \frac{3H^2(t)}{8\pi G}. \tag{1.2}$$

Density parameters are then defined as $\Omega = \rho/\rho_{\mathrm{crit}}$ for matter and radiation, while Ω_Λ and Ω_k stay constant over time for a flat Universe.

$$\Omega_m = \frac{\rho_m}{\rho_{\mathrm{crit}}},\quad \Omega_r = \frac{\rho_r}{\rho_{\mathrm{crit}}},\quad \Omega_\Lambda = \Omega_{0,\Lambda} = \frac{\Lambda c^2}{3H_0^2},\quad \Omega_k = \Omega_{0,k} = kc^2, \tag{1.3}$$

where $\Omega_{0,\Lambda}$, $\Omega_{0,k}$, $\Omega_{0,m}$ and $\Omega_{0,r}$ are the density parameters for the cosmological constant, the curvature, the matter, and the radiation respectively. A more commonly used parameter that describes the evolutionary stage of the Universe is the redshift z. It is connected to the scale factor via $1/(1+z) = a$ and defined such that $z = 0$ and $a = 1$ for present-day Universe. Now the first Friedmann equation can be rewritten as

$$\frac{H^2(t)}{H_0^2} = \Omega_{0,\Lambda} + \Omega_{0,k}(1+z)^2 + \Omega_{0,m}(1+z)^3 + \Omega_{0,r}(1+z)^4. \tag{1.4}$$

It is observationally confirmed that the Universe is flat, i.e. $k = 0$ and $\Omega_k = 0$ (Planck Collaboration et al., 2020a).

1.1.2 Structure formation

Although the Universe is homogeneous on the large scale, there is a subtle density perturbation on the small scale. The initially over-dense regions accumulate more matter and the initially under-dense regions become even less dense over time. This density perturbation grows linearly at first until the over-dense region reaches the critical density that it decouples from the cosmic expansion. Dark matter then collapses into gravitationally bound haloes, which continue to grow in mass by accretion or mergers. Baryons accumulate inside these haloes and are trapped due to gravity. Finally, stars form inside the haloes and start to illuminate the Universe. The formation of dark matter haloes are self-similar and the structure grows hierarchically from the small scale to the large scale.

The structure of matter is filled with many filaments and knots that represent the over-dense regions. The 2dF Galaxy Redshift Survey (Peacock et al., 2001) showed that galaxies are clustered and the spatial distribution of them is indeed web-like. On the other hand, the cosmic microwave background (CMB) is the relic of the initial fluctuation and we are able to see the homogeneity of the Universe on the large scale. The present-day effective temperature of the CMB is $2.725\,\mathrm{K}$, while the fluctuation is on the order of $10^{-5}\,\mathrm{K}$. It was first discovered by Smoot et al. (1992) and modern surveys continue to provide more precise measurements (Planck Collaboration et al., 2020a,b).

1.2 Galaxy formation

By definition, galaxies are gravitationally bound objects that constitute of different components such as stars, planets, gases, and dusts. As discussed in the last section, they form in the over-dense regions in the Universe. These regions are dominated by dark matter, which provide the gravitational potential wells to allow galaxy formation and sustain galaxies in them. In the following sections, I describe some important physical processes of galaxy formation.

1.2.1 Gravitational collapse of gas

Not only the structure of the dark matter but also the baryons is heavily influenced by gravity. In star formation theory, one often needs to consider the competition between gravity and pressure, where gravity allows the gas density to grow and pressure pushes gas outward and decreases the gas density. Jeans (1902) studied the collapse of spherical, isothermal gas cloud. He found that if the cloud mass exceeds a certain mass, gravity dominates and the cloud will start to collapse. To derive this critical mass, we start from the virial theorem: $2K + U = 0$, where K is the kinetic energy and U is the potential energy of the gas. For a spherical gas cloud,

$$\begin{aligned} U &= \frac{-3GM^2}{5R}, \\ K &= \frac{3Mk_\mathrm{B}T}{2\mu m_\mathrm{H}}, \end{aligned} \tag{1.5}$$

where $G = 6.67 \times 10^{-8}\mathrm{cm}^{-3}\mathrm{g}^{-1}\mathrm{s}^{-2}$ is the gravitational constant, M is the mass of the cloud in the unit of g, R is the radius of the sphere in the unit of cm, $k_\mathrm{B} = 1.38 \times 10^{-16}\mathrm{cm}^2\mathrm{gs}^{-2}\mathrm{K}^{-1}$ is the Boltzmann constant, T is the gas temperature in the unit of K, $\mu \approx 1.22$ is the mean weight for atomic gas and $\mu \approx 2.33$ for molecular gas, and $m_\mathrm{H} = 1.67 \times 10^{-24}\mathrm{g}$ is the proton mass. Taking $M = 4\pi R^3 \rho_\mathrm{gas}/3$ into account, we can solve the equation $2K + U = 0$ for R that

$$R = \sqrt{\frac{15k_\mathrm{B}T}{4G\pi\rho_\mathrm{gas}\mu m_\mathrm{H}}}, \tag{1.6}$$

where ρ_gas is the gas mass density in units of gcm^{-3}. The corresponding mass is therefore termed the Jeans mass

$$M_\mathrm{J} = \left(\frac{5k_\mathrm{B}T}{G\mu m_\mathrm{H}}\right)^{3/2} \left(\frac{3}{4\pi\rho_\mathrm{gas}}\right)^{1/2}. \tag{1.7}$$

The lower the temperature or the higher the gas density, the smaller the M_J is.

1.2.2 Formation of molecular hydrogen

The onset of star formation is often in the molecular clouds, i.e., that the gas is in the form of molecules instead of atoms. Hydrogen (H) is the most abundant element in the Universe. Naturally, molecular hydrogen H_2 occupies the largest fraction of molecular gas mass in the cloud. Here I describe a few H_2 formation channels. In the gas phase, the probability of direct formation via collision is small, even more so for H_2 because it lacks a permanent dipole moment and any possible radiation occurs at a very low rate. Another mechanism is the three-body formation,

$$\mathrm{H} + \mathrm{H} + \mathrm{H} \text{ or } \mathrm{H}_2 \longrightarrow \mathrm{H}_2 + \mathrm{H} \text{ or } \mathrm{H}_2, \tag{1.8}$$

where the third H atom or the existing H_2 molecule brings the released energy away to stabilise the newly formed H_2. The reaction rate of the three-body formation depends on the H density and is still not efficient enough with typical interstellar medium densities. A mechanism with higher reaction rates is via chain reactions, e.g.,

$$\begin{aligned} &\mathrm{H} + e^- \longrightarrow \mathrm{H}^- + \gamma \\ &\mathrm{H}^- + \mathrm{H} \longrightarrow \mathrm{H}_2 + e^-, \end{aligned} \tag{1.9}$$

which is order of magnitudes more efficient than the direct formation via collision. This process is referred to as association detachment and the electron simply acts as a catalyst. There are other possibilities of forming H_2 in the gas phase (Galli and Palla, 1998; Omukai, 2000). However, they are all not very efficient. On top of that, H_2 can be destroyed by ultra violet radiation from the stars.

If dust (solid form of heavy elements) exists, it acts as a catalyst of H_2 formation and the reaction rate is much higher than those in the gas phase (Gould and Salpeter, 1963; Hollenbach and Salpeter, 1970). H atoms adhere to the dust grain surface due to the van der Waals force. When there are enough H atoms on the surface, they interact with each other and form H_2 molecules. The released energy is absorbed by both H_2 and the dust grains, which allows H_2 to leave the dust grain and return to gas phase, but not enough to destroy the molecule. The production rate of H_2 on the dust grain follows the following form (Hollenbach and McKee, 1979; Hirashita and Ferrara, 2002),

$$R_{\mathrm{H}_2,\mathrm{dust}} = f_0 n_\mathrm{H} n_\mathrm{dust} \pi a^2 \bar{v}_\mathrm{ther} S_\mathrm{d} \epsilon_{\mathrm{H}_2}, \tag{1.10}$$

where f_0 is the fraction of neutral hydrogen, n_H is the number density of hydrogen nuclei, n_dust is the number density of dust grains, a is the radius of the grain (assuming spherical grains with smooth surface), $\bar{v}_\mathrm{ther}$ is the thermal speed of hydrogen, S_d is the sticking coefficient, and ϵ_{H_2} is the H_2 formation efficiency on the dust grain.

The thermal speed is given by (Spitzer, 1978)

$$\bar{v}_{\rm ther} = \sqrt{\frac{8k_{\rm B}T}{\pi m_{\rm H}}} = 1.4 \times 10^5 \left(\frac{T}{100{\rm K}}\right)^{1/2}, \tag{1.11}$$

where $k_{\rm B}$ is the Boltzmann constant, $m_{\rm H}$ is the atomic mass of hydrogen, and T is the gas temperature. If we assume $\epsilon_{\rm H_2} \sim 1$, we find that (Hirashita and Ferrara, 2005),

$$R_{\rm H_2,dust} \propto S_{\rm d} a^{-1} n_{\rm H} n_{\rm dust} T^{1/2}. \tag{1.12}$$

Given the same dust mass, the smaller the grains are, the faster the H_2 formation. The dust and grain size evolution thus plays a role in galaxy evolution, which is illustrated by recent hydrodynamical simulations. The details is beyond the scope of this thesis. I therefore refer interested readers to earlier works such as Yamasawa et al. (2011); Hou et al. (2017); Chiaki and Wise (2019); Aoyama et al. (2020); Relaño et al. (2022).

1.2.3 Efficiency of star formation

The Jeans mass describes the criterion of cloud collapse, after which gas free falls. One can estimate the star formation rate (SFR) by considering the free-fall time of the gas.

$$t_{\rm ff} = \sqrt{\frac{3\pi}{32G\rho_{\rm gas}}}, \tag{1.13}$$

where G is the gravitational constant and $\rho_{\rm gas}$ is the gas mass density. If we take $\rho_{\rm gas} = 1.67 \times 10^{-22}\,{\rm gcm^{-3}}$ then $t_{\rm ff} \sim 5 \times 10^6\,{\rm yr}$. Given the mass of collapsing gas, SFR is determined by

$$\mathrm{SFR} = \frac{M_{\rm gas}}{t_{\rm ff}}. \tag{1.14}$$

Take the MW for example, the current molecular gas mass is roughly $10^9\,M_\odot$. If all the gas just turns into stars continuously and smoothly, we would expect a SFR of $200\,M_\odot{\rm yr}^{-1}$. However, from recent observation, the current SFR of the MW is only $< 2M_\odot{\rm yr}^{-1}$ (Chomiuk and Povich, 2011; Licquia and Newman, 2015). Other physical processes or mechanisms must be considered to explain the discrepancy between this simple estimate and the observed SFR of the MW. Firstly, the above estimate is based on the assumption that the entire cloud collapses into one core and all the gas mass is converted to stars, regardless of the cloud size. However, it is likely that the cloud has structures. Federrath and Klessen (2012) showed that turbulence creates inhomogeneous structures in the molecular cloud and that the solenoidal forcing suppresses star formation. Magnetic field also provides additional support to the cloud and keeps it from collapsing. Secondly, star formation is assumed to be continuous in Eq. 1.14. In reality, stars that have formed earlier influence the ambient medium and further star formation in the cloud may be regulated. In the next section, I describe different stellar feedback mechanisms in more details.

1.2.4 Radiative and kinetic feedback from massive stars

The gas where stars from is important in determining the stellar properties. Stars also impact their surrounding regions, the stellar feedback. In this section I describe a few important stellar feedback mechanisms.

Stellar Wind

The radiation pressure from the stellar core transfers momentum to the material on the surface through the metal absorption lines or scattering (Lucy and Solomon, 1970; Castor et al., 1975). This ejection of materials is called stellar wind and the corresponding rate of stellar mass change is termed the mass-loss rate ($\dot{M}_{\rm loss}$). Intuitively, the mass-loss rate and the speed of the stellar wind depend on the zero-age main-sequence mass $M_{\rm ZAMS}$, because the stellar luminosity is highly dependent on the stellar mass ($L \propto m^{3.1}$ for stars around $10\,M_\odot$). The stellar wind speed can reach a few thousand kms^{-1} and $\dot{M}_{\rm loss} \sim 10^{-5}\,M_\odot{\rm yr}^{-1}$ for O-type stars. Moreover, Mokiem et al. (2007) found that the mass-loss rate depends on stellar metallicity (Z_*) and an empirical relation $\dot{M}_{\rm loss} \propto Z_*^{0.86}$ is obtained from O and early B-type stars in the Magellanic Clouds. As the stellar wind expands outward, it collides with the ambient medium and creates a bubble-like structure around the star. One-dimensional analytic models of the stellar wind bubble structure were provided as early as in the 1970s (Avedisova, 1972; Weaver et al., 1977). Complementary semi-analytic models and numerical simulations were carried out later (Rogers and Pittard, 2013; van Marle et al., 2015; Rahner et al., 2017, 2019; Haid et al., 2018). In particular, Calura et al. (2015) found that nearly 40% of the initial mass of a proto-globular cluster is removed by stellar winds after a few Myr.

Photoionisation

Since there is still medium surrounding the star, the photons emitted by the stars do not travel freely outward. If the photons have high enough energy, they are likely to be absorbed by the gas and the electrons are excited to a higher state, i.e. the neutral gas is ionised. The regions around the stars where gas is ionised are called the H II regions. Here I describe the expansion of H II region and its dependence on stellar properties.

The first assumption is that the gas is composed of pure Hydrogen with uniform density, at rest and in equilibrium, for simplicity. Therefore, the number of ionising photons emitted should equal to the number of recombination within the H II region,

$$Q = \frac{4\pi}{3} n^2 \alpha_{\rm rec} R_{\rm st}, \tag{1.15}$$

where Q is the number of photons emitted by the star per second, n is the number density of the nuclei in gas, $\alpha_{\rm rec}$ is the recombination rate, and $R_{\rm st}$ is the radius of the H II region. The size of the H II region it then easily determined by rearranging the above equation

$$R_{\rm st} = \left(\frac{3Q}{4\pi n^2 \alpha_{\rm rec}} \right)^{1/3}. \tag{1.16}$$

This was first dervied by Strömgren (1939), thus, the radius is termed the Strömgren radius. The time-scales for the H II region to reach the size of $R_{\rm st}$ is few hundred to few thousand years, assuming $n \sim 100 {\rm cm}^{-3}$.

However, as the gas gets ionised by the photons, the temperature also increases. Therefore, there is an outward pressure caused by the temperature difference between the ionised gas and the neutral gas. The expansion rate of the ionising front (I-front) can be described by the following equation

$$\frac{dR_{\rm I}}{dt} = \frac{1}{4\pi R_{\rm I}^2 n} \left(Q - \frac{4\pi n^2 \alpha_{\rm rec} R_{\rm I}}{3} \right), \tag{1.17}$$

where $R_{\rm I}$ denotes the position of the I-front from the star here. We denote the neutral gas ahead of the I-front as region 1 and the ionised gas as region 2. There are two critical velocities, $v_{\rm R} \sim 2c_{\rm s,2}$ and $v_{\rm D} \sim c_{\rm s,1}^2/(2)c_{\rm s,2}$, where $c_{\rm s,1}$ is the sound speed of region 1 and $c_{\rm s,2}$ is the sound speed of region 2. If the velocity of the I-front $v_{\rm I} \geq v_{\rm R}$, then it is called the R-type I-front. If $v_{\rm I} \leq v_{\rm D}$, it is called the D-type I-front. The R-type phase ends when the H II region reaches the Strömgren radius and the

I-front enters the D-type phase. The time and distance it requires are denoted as t_{D} and $R_{\mathrm{D}} = R_{\mathrm{st}}$. The expansion rate of D-type I-front is written as (Draine, 2011)

$$R_{\mathrm{I}}(t) = R_{\mathrm{D}} \left(1 + \frac{7}{4} \sqrt{\frac{4}{3}} \frac{c_{\mathrm{s},2}(t - t_{\mathrm{D}})}{R_{\mathrm{D}}} \right)^{4/7} . \tag{1.18}$$

The expansion of H II region stops completely when the pressure of the ionised gas equals the pressure of the neutral gas. This is only reached if R_{st} is small.

Supernovae

In this section I list a few typical supernovae (SNe), which are the Type Ia, core-collapse (CC), and pair-instability (PI) SNe and describe the expansion of supernova remenants (SNRs).

- **Type Ia SNe** The distinctive observational feature of Type Ia SNe is that they do not show any hydrogen lines in their spectra. A popular theory of the origin of Type Ia SNe is a binary system that consists of a white dwarf and a main sequence star with small separation. The main sequence star acts as a ”donar” and materials are accreted onto the white dwarf. As the mass of the white dwarf approaches the Chandrasekhar mass (Chandrasekhar, 1931, $\approx 1.4\,M_{\odot}$), a new round of nuclear reaction is ignited and increased temperature only speeds up the process. Finally, the energy release is strong enough to destroy the system and results in a supernova.

- **Core-collapse SNe** The energy produced by the nuclear reaction in the star has been supporting the stellar structure and prevent the star from collapsing. However, to synthesise elements heavier than iron, one needs to inject energy to ignite the reaction. Once the iron core forms, the fusion at the centre of the star stops and the star loses the support. The contraction of the stellar core continues until the density is so high that a rebound shock occurs. The shock passes through and compresses the outer shells of the star, resulting in a new series of nuclear reactions. These nuclear reactions release an enormous amount of energy and destroys the stellar structure. This kind of SNe is thus named core-collapse SNe.

- **Pair-instability SNe** In the core of very massive stars ($M \gtrsim 100\,M_{\odot}$ (Heger et al. (2003)), the pair production of positrons and electrons occur when the nuclei collides with gamma-rays as the temperature reaches $\sim 10^{9}\,\mathrm{K}$. The pressure that is supporting the core structure drops and leads to a collapse.

> The following burning in the cores leads to a thermonuclear explosion and the star is destroyed completely without remnants. The theory of PI SNe is proposed in the 1960s (Fowler and Hoyle, 1964; Bisnovatyi-Kogan et al., 1967; Rakavy and Shaviv, 1967). Due to the requirement of the M_{ZAMS}, most of the theoretical studies assume that the progenitor stars of PI SNe are metal-free stars (Heger and Woosley, 2002, 2010; Dessart et al., 2013, see Sec. 1.3.1 for discussion for discussion on metal-free stars).

Despite the difference in how different types of SNe occur, the expansion of their remnants is similar. The initial velocity of the ejecta can be estimated by considering the SN energy and the mass of the ejecta that

$$v_{\mathrm{ej}} = \left(\frac{2E_{\mathrm{SN}}}{M_{\mathrm{ej}}}\right)^{1/2}, \tag{1.19}$$

which is on the order of $10^4\,\mathrm{kms}^{-1}$ for $E_{\mathrm{SN}} \sim 10^{51}\mathrm{erg}$ and $M_{\mathrm{ej}} \sim M_{\odot}$. The first phase of the SNR expansion is the free-expansion phase, where the radius of the SNR R_{SN} expands proportionally to time t. The free-expansion phase ends when the gas mass swept by the SN can no longer be ignored at a radius of $R_1 = (3M_{\mathrm{ej}}/4\pi\rho_0)^{1/3}$, where ρ_0 is the mass density of the un-swept gas. The time it takes to end the free-expansion phase is very short (on the order of hundred years) and is roughly proportional to $E_{\mathrm{SN}}^{-1/2}\rho_0^{-1/3}$.

In the next phase, the Sedov-Taylor phase, the expansion is dominated by E_{SN} and ρ_0. The expansion can be described by

$$R_{\mathrm{SN}}(t) \propto \left(\frac{E_{\mathrm{SN}}t^2}{\rho_0}\right)^{1/5} \propto t^{2/5}. \tag{1.20}$$

This formula was first derived by Taylor (1941) and Sedov (1946) in the 1940s (hence the name).

The expansion rate of SNR continues to decrease and the importance of radiative cooling in the swept-up material becomes important. The time it takes to this is t_{cool}, which is on the order of ten thousand years. The thermal energy is no longer converged and the expansion is now driven by the pressure difference. The next phase is therefore termed the pressure-driven snowplow phase and R_{SN} is now proportional to $t^{2/7}$. At the end of the pressure-driven phase, the pressure difference drops to the degree that the momentum stays roughly constant. The final phase is called the momentum-driven phase. Since the mass enclosed within the SNR is proportional to R_{SN}^3, the velocity in this phase evolves inversely proportional to R_{SN}

that $v_{\rm SN} \propto R_{\rm SN}^{-3}$. By taking $v_{\rm SN} = dR_{\rm SN}/dt$ and computing the integration, we have

$$R_{\rm SN} \propto t^{1/4}, \text{ and } v_{\rm SN} \propto t^{-3/4}. \tag{1.21}$$

The expansion of SNR stops completely when $v_{\rm SN}$ drops to the sound speed of the ambient medium. The time for the SNR to halt is on the order of million years.

The above mentioned feedback mechanisms may happen at the same time in different places of the galaxy. The combined effect is non-linear and there are no analytic models to describe them altogether. The study of these mechanisms and their relative importance to galaxy formation therefore relies heavily on numerical simulations.

1.2.5 Chemical feedback of stars: source of metal production

On top of the nucleosynthesis that happens inside the star continues throughout the stellar lifetime, there are other physical processes which produce elements heavier than He. In this section I describe three important mechanisms that are responsible for the metal production and the enrichment of the interstellar medium.

Supernovae

As described in Sec. 1.2.4, supernova (SN) is one of the most energetic astronomical events. It triggers further nuclear reaction and synthesise heavy elements much faster than the nuclear reaction in the stellar core. The energy and momentum that SN carries can bring the metals to as far as a few hundred parsecs and mixes with the ambient gas. Stars that form in the supernova remnants therefore contain different elemental abundances that can be trace back to the SNe (Kobayashi et al., 2020). For example, Type Ia SNe are responsible for most of the production of the iron-peak elements (Cr, Mn, Fe, Ni, Co, Cu, and Zn). On the other hand, CC SNe produce much more α elements (O, Mg, Si, S, and Ca). The progenitors of Type Ia SNe are white dwarfs, that are the end result of stars with $M_{\rm ZAMS} \lesssim 10\,M_\odot$. Compared to the progenitor stars of CC SNe which typcially have $M_{\rm ZAMS} \geq 10\,M_\odot$, the time-scales of Type Ia SNe are much longer than the CC SNe. By analysing the $[\alpha/{\rm Fe}]$ ratio of stars, it is possible to constrain the time-scales and the environment of the star formation (Taylor and Kobayashi, 2015; Vincenzo et al., 2018). Heger and Woosley (2002) found that PI SNe produce much more elements with even atomic number than those with odd atomic number. This is due to the lack of neutron capture in the event of PI SNe.

Asymptotic giant branch (AGB) star

At the final stage for stars that have M_{ZAMS} in the range of $\sim 0.8 - 8\,M_{\odot}$, they use up the hydrogen in the centre and the He core forms (Busso et al., 1999; Karakas and Lattanzio, 2014). The core contracts while the outer layer expands. The luminosity and temperature of the star increases, approaching the giant branch in the Hertzsprung–Russell diagram, which is the origin of the name asymptotic giant branch. During this phase, it is thought that the slow process of neutron-capture (s-process) occurs (at time-scales on the order of thousand years). The s-process is responsible for $\sim$ 50% of the production of elements heavier than iron, especially the Ba and Ce (Sneden et al., 2008).

Neutron star merger

In contrast to the s-process, the r-process (rapid neutron-capture process) occurs in an extremely neutron dense environment ($n_{\mathrm{n}} > 10^{24}\,\mathrm{cm}^{-3}$. Among the astrophysical events, it is believed that the CCSNe and the neutron star merger are the most likely ones. Some SNe destroy the stellar structure completely, while some destroy the outer layer only. The stellar core continues to collapse but nuclear fusion is no longer ignited. Without the pressure support, the core reaches extremely high density forming a neutron star. In the merger event of two neutron stars, neutron capture occurs at a much shorter time-scale than the one in s-process. The r-process is responsible for most of the Xe, Eu, and Au production (Sneden et al., 2008).

1.3 Stellar population

The Universe has evolved for a very long time that many different physical processes occur at different times, places, and rates. Stars therefore have different properties depending on the environment they form in. In this section, I briefly describe categories of stellar population.

1.3.1 Population III stars

The very first stars form in gases where only H and He are existent. Therefore, these stars are also referred to as metal-free or Population III (Pop III) stars. The gas only cools via rotational-vibrational transitions of H_2 (Bromm and Larson, 2004) down to $\sim$ 100 K. If we assume a number density of $100\mathrm{cm}^{-3}$, the Jeans mass is on the scale of ten thousand solar masses. This implies that the masses of Pop III stars are much more massive than the sun and they are short-lived. To date, there is yet direct observation of Pop III stars. The formation of these stars are studied mainly through numerical simulations. Earlier studies suggested values from few tens to hundreds of $M_\odot$ (Greif et al., 2010; Stacy et al., 2010, 2016; Hirano et al., 2015; Hirano and Bromm, 2017; Ishigaki et al., 2018).

Despite the non-detection, Pop III stars leave behind important footprints, i.e. the metal yields produced by their SNe. Pop III stars in the mass range $10-40\,M_\odot$ die as CC SNe and in the mass range $140-260\,M_\odot$ they die as PI SNe Heger and Woosley (2002, 2010). After the explosion of SNe, metals mix with the surrounding pristine gas and provide a more efficient cooling channel. Stars that formed in the metal-enriched gas therefore typically have smaller masses than Pop III stars. These metal-enriched stars, especially those that form inside the Pop III supernova remnants, thus carry crucial information that could help us understand the Pop III stars.

1.3.2 Population II/I stars

The metal-enriched stars can be further divided into two categories, which are the metal-poor (Population II or Pop II) stars and metal-rich (Population I or Pop I) stars. The distinction between these two categories is not well defined. Throughout this thesis I will refer all metal-enriched stars as Pop II stars.

Due to the efficient cooling induced by metals, Pop II stars are less massive than Pop III stars, which are typically $< 1\,M_\odot$. The mass distribution of Pop II stars are thought to follow a bottom-heavy initial mass function (IMF). There are a few commonly adopted IMFs in modern simulations:

- **Salpeter IMF** (Salpeter, 1955), a power-law IMF that

  $$\frac{dN}{dM_{\rm star}} \propto M_{\rm star}^{-2.35}, \tag{1.22}$$

  where N is the number of stars and $M_{\rm star}$ is the mass of the star.

- **Kroupa IMF** (Kroupa, 2001), a broken power-law IMF that

  $$\frac{dN}{dM_{\rm star}} \propto M_{\rm star}^{-\alpha}, \tag{1.23}$$

  where $\alpha = 2.3$ for $M_{\rm star}/M_\odot \geq 1$, $\alpha = 1.3$ for $0.08 < M_{\rm star}/M_\odot <= 0.5$, and $\alpha = 0.3$ for $M_{\rm star}/M_\odot <= 0.08$.

- **Chabrier IMF** (Chabrier, 2003), a log-normal IMF that a Salpeter IMF is adopted for $M_{\rm star} \geq 1\,M_\odot$ and for $M_{\rm star} < 1\,M_\odot$

$$\frac{dN}{dM_{\rm star}} \propto 0.158 \times \exp\left\{-\frac{(\log M_{\rm star} - \log(0.079))^2}{1.38^2}\right\}, \tag{1.24}$$

in units of pc^{-3}.

1.4 Observational constraints

So far in this chapter I mainly discuss about the galaxy and star formation from the theoretical perspective. In this section, I introduce important observational discoveries that not only inspire the studies but also provide important constraints to the theoretical models.

1.4.1 Milky Way and its satellites

MW is a spiral galaxy with a bar in the centre and a size of $\sim 30\,\text{kpc}$ (in diameter). In Table 1.1, I list a few observed physical quantities of the MW at $z = 0$: virial mass $M_{\rm vir}$, virial radius $r_{\rm vir}$, stellar mass M_*, molecular mass $M_{\rm mol}$, atomic mass $M_{\rm ato}$, ionised mass $M_{\rm ion}$, and star formation rate (SFR). The nearest galaxy that has a mass similar to the MW is the Andromeda Galaxy (M31), which is $\sim 750\,\text{kpc}$ away and of a virial mass of $[1.5 - 2.5] \times 10^{12}\,M_\odot$. The MW system and the M31 system together are often referred to as The Local Group.

Property	Value	Reference
$M_{\rm vir}$	$1.3 \pm 0.3 \times 10^{12}\,M_\odot$	(1)
$r_{\rm vir}$	$287^{+22}_{-25}\,\text{kpc}$	(1)
M_*	$5.43 \pm 0.57 \times 10^{10}\,M_\odot$	(2)
$M_{\rm mol}$	$[1.3 - 2.5] \times 10^9\,M_\odot$	(3)
$M_{\rm ato}$	$\gtrsim 6 \times 10^9\,M_\odot$	(3)
$M_{\rm ion}$	$\gtrsim 1.6 \times 10^9\,M_\odot$	(3)
SFR	$[1.65 - 1.9]\,M_\odot/\text{yr}$	(4), (5)

Table 1.1: Observed physical properties of the MW at $z = 0$. From top to bottom: virial mass, virial radius, stellar mass, molecular mass, atomic mass, ionised mass, and star formation rate. References: (1) Posti and Helmi (2019), (2) McMillan (2017), (3) Ferrière (2001), (4) Chomiuk and Povich (2011), (5) Licquia and Newman (2015).

MW is surrounded by many smaller galaxies, the satellites. There are nearly 60 MW satellites observed so far, and the stellar masses of them range from few hundred solar masses to $> 10^9\,M_\odot$ (McConnachie, 2012; Muñoz et al., 2018; Newton et al., 2018; Erkal et al., 2019). The smallest satellites ($L < 10^5\,L_\odot$) are mostly dark matter dominated (Simon, 2019). The estimate of their virial masses is difficult because there are too few stars in them. A know problem of the ΛCDM model it the difference between theoretical prediction of number of satellites and the number of the observed ones, the ”missing satellite problem” (Kauffmann et al., 1993; Moore et al., 1999; Klypin et al., 1999). A solution is proposed to reolve the discrepancy by taking the detection efficiency into account (Kim et al., 2018).

1.4.2 Extremely metal-poor stars

Extremely metal-poor (Beers and Christlieb, 2005, EMP) stars are defined as stars with metallicity [Fe/H][1] < -3 and are thought be the best candidates to study the properties of Pop III stars and star formation enviroment of high redshift Universe (Frebel and Norris, 2015). Searches of EMP stars have been carried out mostly within the MW system (Lai et al., 2008; Yong et al., 2013; Roederer et al., 2014; Hansen et al., 2020). The number of EMP detection increases and the metallicity floor has been pushed to lower and lower, thanks to the development of larger telescopes in the past decades. Large surveys in the past few years report the detection of EMP stars on the order of ten-thousand (Hayden et al., 2014; Starkenburg et al., 2017; Chiti et al., 2021c,a). In particular, Nordlander et al. (2019) found a star that has $[\mathrm{Fe/H}] = -6.2$ and Keller et al. (2014) presented the discovery of a star that has an metallicity of $[\mathrm{Fe/H}] < -7.1$. Some of these EMP stars can be explained with a mono-enrichment or metal-enrichment by a handful of Pop III stars (Ishigaki et al., 2014; Keller et al., 2014; Tominaga et al., 2014; Ji et al., 2015; Placco et al., 2015, 2016; Fraser et al., 2017; Ishigaki et al., 2018; Magg et al., 2018; Hartwig et al., 2018). Detail analysis of the elemental abundances of these stars lead to finer categorisations. In the following sections, I describe two special populations of EMP stars, which are the carbon-enhanced metal-poor (CEMP) stars and r-process enhanced metal-poor stars.

Carbon-enhanced metal-poor stars

Decades ago, CEMP stars have been discovered and found to take a big fraction of the metal-poor stars (Beers et al., 1992; Christlieb, 2003). Following the definition in Beers and Christlieb (2005), CEMP stars are defined as stars with $[\mathrm{C/Fe}] \gtrsim +1.0$.

---

[1] The notation of [X/Y] is defined as the number ration of X element to Y element relatively to the solar ratio in the log space, i.e. $[\mathrm{X/Y}] \equiv \log_{10}(\mathrm{X/Y}) - \log_{10}((\mathrm{X/Y}))_\odot$. The solar abundances are adopted from Asplund et al. (2009).

An updated definition of CEMP stars with [C/Fe] $\gtrsim +0.7$ was proposed by (Aoki et al., 2007). In the extreme cases, stars with [C/Fe] > 4 are found (Norris et al., 2013), which means that the carbon abundance is more than 10000 times more than iron. CEMP stars can be further put into sub-groups based on their neutron-capture elemental abundances (Beers and Christlieb, 2005): CEMP-r ([Eu/Fe] $> +1.0$), CEMP-s ([Ba/Fe] $> +1.0$ and [Ba/Eu] $> +0.5$), CEMP-r/s ($0.0 <$ [Ba/Eu] $< +0.5$), CEMP-no ([Ba/Fe] < 0). Again, the definition of these sub-groups is updated or even new sub-groups are defined by different authors (Abate et al., 2016; Frebel, 2018; Hansen et al., 2019).

The distribution of these CEMP sub-groups in the MW is not uniform. Among analysing 323 metal-poor stars, Carollo et al. (2014) found that more than half of the CEMP stars in the inner halo of the MW are CEMP-s stars. In the outer halo of the MW, the fraction of CEMP-s stars drop to 30%. This implies that the origin of CEMP-s and CEMP-no stars are different. By definition, CEMP-s stars should form in an environment with neutron. One possible channel is that these stars accrete material from nearby AGB stars Lucatello et al. (2005). On the other hand, CEMP-no stars show no enhancement of neutron-capture elements. Since they occupy the lower end of the metallicity distribution (Norris et al., 2013), they are thought to be possible "second-generation" stars that form under the direct influence of Pop III SNe (Sarmento et al., 2017).

r-process enhanced metal-poor stars

The key element that is mostly used to determine whether a metal-poor star is r-process enhanced is the europium (Eu) with a commonly used criterion [Eu/Fe] $> +0.7$ (Roederer et al., 2018). These stars are also classified as r-II stars. Ji et al. (2016) found that 7 out of 9 spectroscopically resolved stars in the ultra-faint dwarf galaxy Reticulum II are r-process enhanced. This discovery implies that the r-II stars that are found in the Galactic halo may have formed initially in the dwarf galaxies. They later migrated into the Galactic halo because the original dwarf galaxies merged with the MW. The sample in Reticulum II is further expanded in Ji et al. (2022) and they found that more than 70% of the stars are r-processed enhanced.

The discovery of neutron star-neutron star merger event detected by LICO/Virgo (GW170817, Abbott et al., 2017) inspired the extensive search of r-II stars in the MW halo such as The R-process Alliance (Hansen et al., 2018; Sakari et al., 2018; Ezzeddine et al., 2020; Holmbeck et al., 2020), and extension to other elements for some of the metal-poor stars, (Cain et al., 2020; Roederer et al., 2022).

1.5 Thesis outline

In this chapter, I describe the theoretical background of star formation and galaxy formation, the current understanding of the observed Milky Way system, properties of the observed extremely metal poor stars and their implication on the star formation in the early Universe. In the following chapters, I describe the works that have been carried out during the course of this thesis in order to understand the star formation in the MW system. Note that I change the narrative in the following chapters from *I* to *we* to highlight the contributions from the listed coauthors, in terms of providing scientific insights and suggestions of the phrasing.

Chapter 2 The implementation of a new star formation model in the semi-analytic code A-SLOTH is described. The star formation is no longer in the form of star clusters but individual stars. The stellar mass-to-halo mass relation at $z = 0$ down to the ultra-faint regime (M_*) of Milky Way-like systems is shown and its implication is discussed. The work is published as Chen et al. (2022).

Chapter 3 I describe a new analysis method which utilises the unsupervised clustering algorithm. The comparison between the simulated and observed galaxies is performed in high-dimensional (in this work, 5D) data space. A goodness-of-fit is determined for the A-SLOTH fiducial model. This new method helps with the improvement of the model and can be easily applied to different types of data.

Chapter 4 Locations of extremely metal-poor stars in Milky Way/M31-like galaxies in the Illustris TNG50 simulation are analysed and discussed. The galaxies are decomposed into different components based on the spacial information and stellar kinematics. Quantification of the frequency of extremely metal-poor stars in different components and the implication are presented and discussed.

Chapter 5 Finally, I summarise the new methods and findings presented in this thesis. I further discuss about outlooks of the models with respect to understanding the formation of dwarf satellites of the Milky Way.

2

Stellar mass-to-halo mass relation of Milky Way satellites at redshift 0

This chapter is based on the paper published by MNRAS in 2022 as Chen et al. (2022). I am the first author and I conduct all the simulations and analysis presented in the paper and in this chapter. Physical insights and suggestions are provided from all the listed co-authors. The text is primarily written by me with feedback and suggestions from all listed coauthors. Specifically, Mattis Magg contributed to the text of external enrichment and ionizing volumes and Tilman Hartwig contributed to the text of adaptive time-step.

Abstract

We study the stellar mass-to-halo mass relation at $z = 0$ in 30 Milky Way-like systems down to the ultra-faint ($M_* < 10^5 M_\odot$) regime using the semi-analytic model A-SLOTH. A new model allows us to follow star formation and the stochastic stellar feedback from individually sampled Pop II stars. Our fiducial model produces consistent results with the stellar mass-to-halo mass relation derived from abundance matching and the observed cumulative stellar mass function above the observational completeness. We find a plateau in the stellar mass-to-halo mass relation in the ultra-faint regime. The stellar mass of this plateau tells us how many stars formed before supernovae occur and regulate further star formation, which is determined by the Pop II star formation efficiency. We also find that the number of luminous satellites increases rapidly as M_* decreases until $M_* \approx 10^4 M_\odot$. Finally, we find that the relative streaming velocity between baryons and dark matter at high redshift is important in determining the number of ultra-faint dwarf galaxies at $z = 0$. The new model in A-SLOTH provides a framework to study the stellar properties and the formation history of metal-poor stars in Milky Way and its satellites.

2.1 Motivation

Galaxy formation depends heavily on properties and evolution of the host dark matter halo. The most straightforward connection between them is perhaps the stellar mass-to-halo mass (SMHM) relation. Previous studies have found that for systems with stellar masses $M_* > 10^5 M_\odot$ (Shankar et al., 2006; Drlica-Wagner et al., 2020; Garrison-Kimmel et al., 2014, 2017; Jethwa et al., 2018; Salucci, 2019; Nadler et al., 2020), the galaxies and their host haloes follow a tight SMHM relation. However, whether this relation still holds for ultra-faint dwarf galaxies ($M_* < 10^5 M_\odot$, UFDs) is still unclear. In recent years, numerous UFDs around the MW have been discovered by large surveys (Willman, 2010; Drlica-Wagner et al., 2015, 2020; Koposov et al., 2015; Torrealba et al., 2016, 2018). Despite the low completeness of UFD discoveries, these UFDs already provide us with constraints on the SMHM relation and the underlying galaxy formation model.

There have been many recent cosmological zoom-in simulations of MW-like systems or isolated UFDs (e.g. Hopkins et al., 2014; Wetzel et al., 2016; Wheeler et al., 2019; Libeskind et al., 2020; Font et al., 2020, 2021; Engler et al., 2021). These simulations still cannot resolve the smallest dwarf galaxies in the MW system. Due to the high spatial and mass resolutions that are needed to properly simulate UFDs, the required time and computational resource is immense. Semi-analytic models provide an opportunity to explore different physical processes and a wider range of parameters. For example, de Bennassuti et al. (2014, 2017) utilised the semi-analytic code GAMETE to investigate the metallicity distribution function in the Galactic halo and the carbon-enhanced metal-poor stars. Their model is based on the Extended Press–Schechter formalism (Press and Schechter, 1974; Lacey and Cole, 1993) and includes the transition between metal-free and metal-enriched star formation following metal and dust evolution. Salvadori et al. (2015) and Rossi et al. (2021) employed GAMETE to study the carbon-enhanced metal-poor stars in the dwarf galaxies in the Local Group. Visbal et al. (2018, 2020) studied the metal-free star formation rate down to $z = 6$, including physical processes such as photo-ionisation, Lyman-Werner (LW) radiation, and metal enrichment. Kravtsov and Manwadkar (2022) used GRUMPY to study the stellar mass-to-halo mass relation and stellar mass-metallicity relations in the dwarf galaxies. However, they do not include metal-free star formation in their model.

2.2 Semi-analytic model: A-SLOTH

In this work, we use our semi-analytic galaxy formation code A-SLOTH (Ancient Stars and Local Observables by Tracing haloes (Hartwig et al., 2022; Magg et al., 2022) to study the SMHM relation in satellites of MW-like systems. A-SLOTH has been used to study various problems, such as the lower limit of IMF of metal-free stars (Hartwig et al., 2015), the connection between the metal-poor stars in the MW and their progenitors (Hartwig et al., 2018, 2019), the probability of finding metal-free survivors in the MW (Magg et al., 2018), and the inhomogeneous mixing of metals in the interstellar medium (Tarumi et al., 2020). In these previous studies, A-SLOTH only tracked the total mass of metal-enriched stars forming in each system, rather than tracing the formation and evolution of the stars individually. Therefore, the corresponding stellar feedback was considered to be continuous and computed using IMF-averaged quantities. In this paper, we introduce a new model in A-SLOTH that allows metal-enriched stars to be traced individually. This enables A-SLOTH to properly follow the detailed star formation activity in individual systems and the impact of stellar feedback.

A complete description of the physical processes accounted for in A-SLOTH is given in (Hartwig et al., 2022). Here, we focus on the parts of the model that are the most important for our current study.

2.2.1 Dark matter merger trees

A-SLOTH uses dark matter halo merger trees drawn from the LX14 run of the *Caterpillar* project (Griffen et al., 2016), which is a dark-matter-only cosmological simulation suite focusing on the assembly of MW-sized haloes and their satellite galaxies. The dark matter particles in the LX14 run have masses of $\sim 3 \times 10^4 M_\odot$ and the gravitational softening length is $76h^{-1}$pc. It is based on the Planck Collaboration et al. (2014) cosmological parameters in a 100 h^{-1}Mpc box. MW-like systems are selected at $z = 0$ if the main haloes fulfill the following criteria:

1. Virial mass in range $0.7 \times 10^{12} M_\odot \leq M_{\rm vir,peak} \leq 3 \times 10^{12} M_\odot$.
2. There is no halo with $M_{\rm vir,peak} \geq 7 \times 10^{13} M_\odot$ within 7 Mpc.
3. There are no other haloes with $M_{\rm vir,peak} \geq 0.5 \times M_{\rm main}$ within 2.8 Mpc of the main halo.

Dark matter haloes are identified with ROCKSTAR (Behroozi et al., 2013) and we define $M_{\rm vir,peak}$ as the maximum virial mass along the main branch a halo ever attains up to the current redshift, that is computed with the evolution of the virial relation from Bryan and Norman (1998). We adopt their notation here. Griffen et al. (2016) extracted the full merger history of these MW-like systems, including dark matter and spatial information of the haloes and global time-steps between the snapshots, Δt_z, which is $\approx$ 5Myr down to $z = 6$ and $\approx$ 50Myr at $z = 6 - 0$. We have verified in an earlier study that the mass resolution of these merger trees is sufficient to model Pop III star formation at high redshift and using higher resolution merger trees yields converged results (see Appendix A of Magg et al. 2018). In this work, we select 30 merger trees from their sample. A-SLOTH walks through these merger trees and determines the baryonic contents of each halo in the merger tree based on the implemented physics. We describe the physical processes in the following sections.

2.2.2 Population III star formation model

We follow the same metal-free (Pop III) star formation (SF) model as in our previous works (Magg et al., 2018; Tarumi et al., 2020). We briefly summarise the model here. Pop III stars are assumed to form when H_2 can cool primordial gas efficiently, which means that a halo needs to exceed a critical mass, $M_{\rm crit}$. In A-SLOTH, Pop III stars form instantly in a single star burst in a mini-halo (haloes below the atomic cooling threshold ($T_{\rm vir} = 10000\,{\rm K}$) as soon as its virial mass exceeds $M_{\rm crit}$. By default, we follow the prescriptions given in Schauer et al. (2021, their Eqs. 9 and 10) and Hummel et al. (2012, their Eq. 1) to determine $M_{\rm crit}$. Schauer et al. (2021) showed that the critical mass is dependent on the LW background and the large-scale streaming velocity of the baryons relative to the dark matter:

$$\log_{10} M_{\rm crit,S21} = 6.0174\,(1.0 + 0.166\sqrt{J_{21}}) + 0.4159\frac{v_{\rm BC}}{\sigma_{\rm rms}}. \tag{2.1}$$

Here, $M_{\rm crit,S21}$ is the critical mass in units of solar masses, J_{21} is the strength of LW background in units of $10^{-21}\,{\rm erg\,s^{-1}\,cm^{-2}\,Hz^{-1}\,sr^{-1}}$, $v_{\rm BC}$ is the large-scale streaming velocity of the baryons relative to the dark matter in units of $\sigma_{\rm rms}$, and $\sigma_{\rm rms}$ is the root-mean-squared value of the streaming velocity. We denote this default model hereafter as S21. We do not self-consistently follow the build-up of the LW background, because the effective volume of our MW-like merger trees is too small to obtain a cosmologically representative estimate of the LW background. Instead, we adopt the simple redshift-dependent fitting formula,

$$J_{21} = 10^{2-z/5}, \tag{2.2}$$

which is based on the work in Greif and Bromm (2006). We take $v_{\rm BC} = 0.8\,\sigma_{\rm rms}$ as the fiducial baryonic streaming velocity, since this is the most likely value to be present at a randomly selected point in the Universe (Schauer et al., 2021). The impact of varying our treatment of both of these effects is explored in Section 2.4.3.

In addition, we assume that gas can cool down efficiently and form stars in haloes that have virial temperatures above the atomic cooling limit ($T_{\rm vir} \geq 10^4$K) when there is no strong ionising radiation field (Visbal et al., 2017). Therefore, we consider haloes that have virial masses larger than $M_{\rm crit,10^4K}$ can form Pop III stars, where $M_{\rm crit,10^4K}$ is computed by

$$M_{\rm crit,10^4K} = 10^{7.5}\left(\frac{1+z}{10}\right)^{-1.5}. \tag{2.3}$$

The final critical mass is then determined by $M_{\rm crit,fin} = {\rm MIN}(M_{\rm crit,S21}, M_{\rm crit,10^4K})$.

Cold gas is converted to Pop III stars in haloes with $M_{\rm halo} \geq M_{\rm crit}$ at a fixed efficiency $\eta_{\rm III}$, defined such that $M_{*,\rm III} = \eta_{\rm III}\Omega_{\rm b}M_{\rm halo}/\Omega_{\rm m}$, where $M_{\rm halo}$ is the current virial mass of the halo, $\Omega_{\rm b}$ is the baryon density parameter today, and $\Omega_{\rm m}$ is the matter density parameter today. We adopt $\Omega_{\rm b} = 0.0486$ and $\Omega_{\rm m} = 0.3089$ (Planck Collaboration et al., 2016). We follow the Pop III model in Tarumi et al. (2020) and sample stars stochastically from an IMF with a slope of $dN/d(\rm logM) \propto M^{0.5}$ in the mass range of $2 < M_* < 180 M_\odot$. Further SF is halted when the total mass of newly-formed Pop III reaches $M_{*,\rm III}$.

We calculate the stellar lifetimes of Pop III stars by interpolating between values assembled from several previous studies: Marigo et al. (2001) for stars in the mass range 0.7-100$M_\odot$; Schaerer (2002) for stars in the mass range 5-500$M_\odot$ (and note that we consider their models without mass loss); and Ekström et al. (2008) for stars in the mass range 9-200$M_\odot$. If the stellar lifetime of a star is provided by multiple works, we use the mean value. Pop III stars die as core-collapse supernovae (CCSNe) in the range of 10-40$M_\odot$ and as pair-instability supernovae (PISNe) in the range of 140-260$M_\odot$ (Heger and Woosley, 2002, 2010). Following Tarumi et al. (2020), we further assume that 30% ($f_{\rm faint} = 0.3$) of the Pop III CCSNe explode as faint supernovae. We use the tabulated metal yields provided in Kobayashi et al. (2011) and Nomoto et al. (2013) for PISNe and normal CCSNe, and the yields in Ishigaki et al. (2014, 2018) for faint CCSNe. We assume that a fraction $f_{\rm fallback} = 0.2$ (Ritter et al., 2015) of the metals remains in the mini-halo after the supernovae have exploded, with the remaining fraction $(1 - f_{\rm fallback})$ gaining enough energy from the SNe to escape from the gravitational well of the mini-halo. Tarumi et al. (2020) calibrated the Pop III SF efficiency ($\eta_{\rm III}$), $f_{\rm faint}$ and $f_{\rm fallback}$ to reproduce the observed MW metallicity distribution function (MDF). The main focus of this work is on the stellar masses of the dwarf galaxies and our model does not heavily depend on metallicity. Therefore, we adopt the same values of $\eta_{\rm III}$, $f_{\rm faint}$ and $f_{\rm fallback}$ as in Tarumi et al. (2020) without investigating the effects of these parameters in detail.

Following the initial Pop III star burst, we assume that any future star formation in the same halo will be in the form of metal-enriched stars. However, stellar feedback will have heated the gas in the mini-halo and ejected a fraction of it. Therefore, further SF is suppressed until the gas re-accumulates and cools down. We denote this time between the Pop III star burst and the onset of further star formation as $t_{\rm rec}$, known as the recovery time, which was calibrated by Tarumi et al. (2020).

2.2.3 Population II star formation model

We implement an improved Pop II SF model, which is based on the models in Magg et al. (2018) and Tarumi et al. (2020). The explanations of important variables in the Pop II SF model are listed in Table 2.1. We assume that the baryons initially associated with a given dark matter halo are located either in cold gas ($M_{\rm cold}$), in hot gas ($M_{\rm hot}$), in a Pop II stellar component ($M_{*,\rm II}$), or have been lost from the halo in an outflow ($M_{\rm out}$). The initial baryonic mass of a halo with virial mass $M_{\rm vir,peak}$ is assumed to be $(\Omega_{\rm b}/\Omega_{\rm m})M_{\rm vir,peak}$. Therefore, by construction

$$M_{\rm vir,peak}\frac{\Omega_{\rm b}}{\Omega_{\rm m}} = M_{\rm cold} + M_{\rm hot} + M_{*,\rm II} + M_{\rm out} \tag{2.4}$$

is always maintained in the model. Note that in our model, hot gas is any gas that is not cold, i.e. it corresponds to the sum of the warm and hot phases of the ISM in the usual three-phase description (Cowie et al., 1981; Klessen and Glover, 2016). We do not account for Pop III stars in the mass budget because the small value we adopt for $\eta_{\rm III}$ means that they never represent more than a small fraction of they baryonic mass in any halo. Additionally, they occupy a negligible fraction of the stellar mass at $z = 0$ and the Pop III stars that remain on the main sequence after $t_{\rm rec}$ are too low mass to contribute significantly to the stellar feedback.

Unlike Pop III SF, we assume that Pop II stars can form in multiple epochs, and so we further divide the global time-steps (Δt_z) from the merger tree into smaller ones. In other words, we have subcycles in our Pop II SF model. The subcycle time-step is denoted as δt_i, and we describe how we determine it in our simulation at the end of this section. A halo is labeled to trigger Pop II SF if the time since it experienced Pop III SF equals or exceeds $t_{\rm rec}$ or if it is externally enriched by supernovae from nearby haloes. Prior to the subcycling of Pop II SF, we initialise

Name	Definition
$M_{\mathrm{vir,peak}}$	peak virial mass of the halo up to current z
M_{cold}	cold gas mass
M_{hot}	hot gas mass
M_{out}	cumulative outflow mass
$M_{*,\mathrm{II}}$	total Pop II stellar mass
M_{disk}	disk mass, including gas and stars
δM_{out}	outflow mass
$\delta M_{\mathrm{out,cold}}$	cold gas mass that enters outflow
$\delta M_{\mathrm{out,hot}}$	hot gas mass that enters outflow
δM_{heat}	mass that transfers from cold gas to hot gas
$\delta M_{*,\mathrm{II}}$	Pop II stellar mass that is formed
$\delta M_{\mathrm{acc,hot}}$	hot gas mass that is accreted from IGM
i	step i in the subcycle
$n_{\mathrm{bins,II}}$	number of Pop II IMF bins
$M_{\mathrm{bound,II}}$	lower and upper limits of Pop II stellar mass
$n_{\mathrm{cold}}^{\mathrm{den}}$	number density of dense gas
v_{BC}	relative streaming velocity between baryon and dark matter
η_{II}	Pop II star formation efficiency
α_{II}	slope of the Pop II IMF
γ_{out}	outflow efficiency (Eq. 2.35)
α_{out}	exponent in γ_{out}
M_{norm}	normalisation mass in γ_{out}
Δt_z	time difference between each snapshot in the merger tree
δt_i	adaptive time-step i in the SF subcycle
t_{dyn}	dynamical time scale of the halo
$t_{\mathrm{cold,ff}}$	free-fall time scale of cold gas
t_{star}	stellar formation time scale
t_{cool}	cooling time scale
t_{acc}	hot gas accretion time scale

Table 2.1: Definitions of the variables in the Pop II star formation model.

the halo by inheriting the baryonic contents from all of its progenitors, which gives us $M^0_{\rm cold}$, $M^0_{\rm hot}$, $M^0_{*,\rm II}$, and $M^0_{\rm out}$. Then, in time-step i of the subcycle, the baryonic quantities are updated with the following equations:

$$\begin{aligned} M^{i+1}_{\rm cold} &= M^i_{\rm cold} + \frac{\delta t_i M^i_{\rm hot}}{t_{\rm dyn}} - \delta M^i_{\rm out,cold} - \delta M^i_{\rm heat} - \delta M^i_{*,\rm II}, \\ M^{i+1}_{\rm hot} &= M^i_{\rm hot} - \frac{\delta t_i M^i_{\rm hot}}{t_{\rm dyn}} - \delta M^i_{\rm out,hot} + \delta M^i_{\rm heat} + \delta M^i_{\rm acc,hot}, \\ M^{i+1}_{\rm out} &= M^i_{\rm out} + \delta M^i_{\rm out,cold} + \delta M^i_{\rm out,hot}. \end{aligned} \tag{2.5}$$

We start from $i = 0$ and make sure the last time-step in the subcycle always ends exactly at the next global time-step of the merger trees.

There are several physical processes that enter the above equations. We show the connections between these processes and the baryonic contents in our Pop II SF model in Figure 2.1:

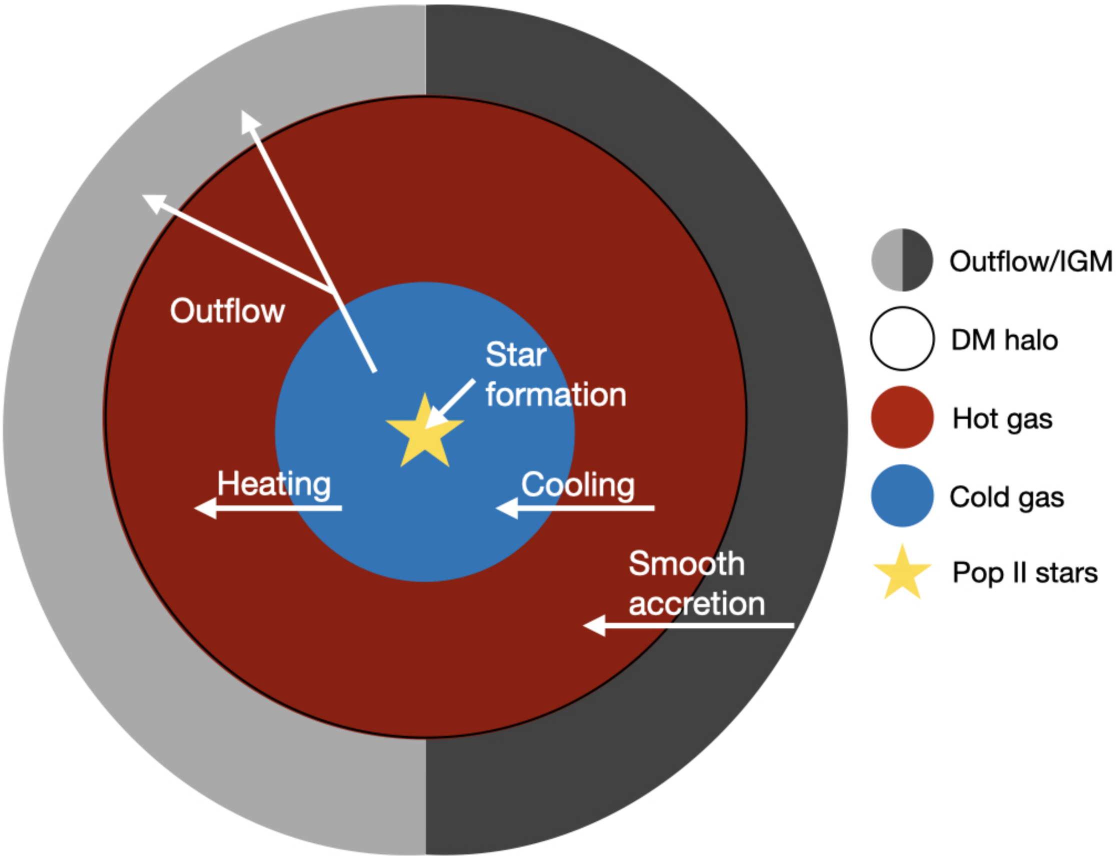

Figure 2.1: We show the connections between different components of our Pop II SF model in this cartoon plot. Note that we do not re-accrete outflow material. Therefore we use separate colours for outflow and IGM.

1. **Cooling of hot gas**

   We assume that hot gas cools on a timescale equal to the dynamical time of the stellar disk, $t_{\rm dyn}$. Therefore, during the subcycle time-step δt_i, a mass of gas $M^i_{\rm hot}\delta t_i/t_{\rm dyn}$ is transferred from the hot gas reservoir to the cold gas reservoir. We assume that cold gas and stars reside in a central region of the halo with a radius of R_s, where $R_{\rm s} = R_{\rm vir}/c_{\rm dm}$ and $c_{\rm dm}$ is the halo's concentration. We follow the fitting functions of $c_{\rm dm}$ in Correa et al. (2015), which are also provided here:
   when $z < 4$,

$$\begin{aligned}
&\log_{10}c_{\rm dm} = a + b\log_{10}(M_{\rm vir})\left(1 + cM^2_{\rm vir}\right)\\
&a = 1.7543 - 0.2766(1+z) + 0.02039(1+z)^2\\
&b = 0.2753 + 0.00351(1+z) - 0.3038(1+z)^{0.0269}\\
&c = -0.01537 + 0.02102(1+z)^{-0.1475}
\end{aligned} \tag{2.6}$$

   and when $z \geq 4$,

$$\begin{aligned}
&\log_{10}c_{\rm dm} = a + b\log_{10}(M_{\rm vir})\\
&a = 1.3081 - 0.1078(1+z) + 0.00398(1+z)^2\\
&b = 0.0223 - 0.0944(1+z)^{-0.3907}.
\end{aligned} \tag{2.7}$$

   The dynamical time scale of the central region of the halo is computed with $t_{\rm dyn} = R_{\rm s}/v_{\rm dyn}$ and that the velocity is computed with $v_{\rm dyn} = \sqrt{G(M_* + M_{\rm cold})/R_{\rm s}}$.

2. **Heating of cold gas and gas removal by photoionisation**

   We consider the effects of photoionisation feedback from massive stars, $\delta M^i_{\rm heat}$. In haloes below the atomic cooling limit ($T_{\rm vir} = 10000$K), $\delta M^i_{\rm heat}$ is added directly to the outflow, whereas in haloes above the atomic cooling limit, an amount of gas with a mass of $\delta M^i_{\rm heat}$ is removed from the cold gas reservoir and added to the hot gas reservoir. The derivation of $\delta M^i_{\rm heat}$ is given in Section 2.2.4.

3. **Accretion of hot gas**

   We assume that hot gas is continuously accreted from the intergalactic medium. In time-step i, an amount of hot gas

$$\delta M^i_{\rm acc,hot} = \left(\frac{\Omega_{\rm b}}{\Omega_{\rm m}} M_{\rm vir,peak} - M^0_{\rm cold} - M^0_{\rm hot} - M^0_{*,\rm II} - M^0_{\rm out}\right) \frac{\delta t_i}{\Delta t_z}, \tag{2.8}$$

   is added to the hot gas reservoir.

4. **Ejection of hot and cold gas**

   We account for the loss of both hot and cold gas from the halo due to the effects of stellar feedback, as described in Section 2.2.4.

5. **Pop II star formation**

   We assume that Pop II stars form with an IMF given by Kroupa (2001) in the mass range $0.01 - 100 M_\odot$. We sample this IMF using $4095 + 1$ logarithmically-spaced bins ($n_{\rm bins,II} = 4096$). Stars with masses $\leq 0.81 M_\odot$ have stellar lifetimes larger than the age of Universe (Marigo et al., 2001) and they do not contribute significantly to stellar feedback. Therefore, we use only a single mass bin to represent long-lived stars and adopt a finer mass resolution for $M_{\rm star} > 0.81$ $M_\odot$.

   To estimate how much cold gas is converted into stars during a subcycle time-step, we first calculate

$$M^i_{*\rm II,est} = \eta_{\rm II} M^i_{\rm cold} \frac{\delta t_i}{t^i_{\rm cold,ff}}, \tag{2.9}$$

   where $\eta_{\rm II}$ is the Pop II SF efficiency, $t^i_{\rm cold,ff} = (G\rho^i_{\rm cold})^{-1/2}$ is the free-fall time of the cold gas, $\rho^i_{\rm cold} = M^i_{\rm cold}/V_{\rm cold}$ is the mean cold gas density of the halo, $M^i_{\rm cold}$ and $V_{\rm cold}$ are the cold gas mass and volume that cold gas occupies, respectively. We assume that the cold gas and stars occupy only the innermost 5% (in radius) of the halo, which is fixed during the subcycle, and so

$$V_{\rm cold} = \frac{4\pi}{3}(0.05\, R_{\rm vir})^3.$$

   Next, we compute the number of stars in each IMF mass bin j if they follow exactly the Kroupa IMF, $n_{j,\mathrm{avg}}$, which can be computed from $M^i_{*\mathrm{II,est}}$ by

$$n_{j,\mathrm{avg}} = \frac{C_{\mathrm{II}} m^{\alpha_{\mathrm{II}}}_{j,\mathrm{star}}}{\Sigma^{N_{\mathrm{bin}}}_{j=1} C_{\mathrm{II}} m^{\alpha_{\mathrm{II}}+1}_{j,\mathrm{star}}} M^i_{*\mathrm{II,est}}, \tag{2.10}$$

where $m_{j,\mathrm{star}}$ is the stellar mass of one star in IMF bin j, α_{II} is the slope and C_{II} is the coefficient: $C_{\mathrm{II}} = 1$ and $\alpha_{\mathrm{II}} = 0.7$ in the mass range $0.08M_\odot < m_{j,\mathrm{star}}$, $\alpha_{\mathrm{II}} = -0.3$ and $C_{\mathrm{II}} = 0.08$ in the mass range $0.08M_\odot \leq m_{j,\mathrm{star}} < 0.5M_\odot$, and $\alpha_{\mathrm{II}} = -1.3$ and $C_{\mathrm{II}} = 0.04$ in the mass range $0.5M_\odot \leq m_{j,\mathrm{star}}$ (Kroupa, 2001).

We calculate the averaged mass of stars with masses $< 0.81M_\odot$ which leads to $m_{1,\mathrm{star}} = 0.174M_\odot$ and $n_{1,\mathrm{avg}} = 2.454M^i_{*\mathrm{II,est}}/M_\odot$. We then compute

$$n_{j,\mathrm{avg}} = \frac{0.573(m_{j,\mathrm{star}})^{-1.3}}{\Sigma^{4096}_{j=2}(m_{j,\mathrm{star}})^{-0.3}} M^i_{*\mathrm{II,est}} \tag{2.11}$$

for stars with masses $\geq 0.81M_\odot$.

Finally, if $n_{j,\mathrm{avg}} \leq 10$, we randomly generate a number, $n_{j,\mathrm{poi}}$ of stars via Poisson sampling. Poisson sampling has the advantage that with a constant SF rate, we can still form the correct number of stars over a time-period even if the time-steps are so small that far less than one star forms per sub-time-step (Sormani et al., 2017). We deactivate the Poisson sampling if $n_{j,\mathrm{avg}} > 10$ and use $n_{j,\mathrm{avg}}$ directly because Poisson sampling is computationally expensive and the difference between $n_{j,\mathrm{avg}}$ and $n_{j,\mathrm{poi}}$ when $n_{j,\mathrm{avg}} > 10$ is small. The total mass of newly formed Pop II stars in each step i is then $\delta M^i_{*,\mathrm{II}} = \Sigma m_{j,\mathrm{star}} n_j$, where n_j is the number of stars in bin j. Throughout the simulation, we track massive stars ($> 8M_\odot$) individually because their stellar feedback is important to subsequent SF.

We adopt $\eta_{\mathrm{II}} = 2$ as our fiducial value and explain the calibration in Section 2.3.

Finally, we adopt adaptive time-steps in the subcycles, which means that δt_i varies. The adaptive time-step guarantees that all physical processes are accurately resolved when the relative change in any component of the baryonic mass budget is fast, and that we save computational time where the relative change is slow. We calculate three additional timescales:

$$\begin{aligned} t_{\mathrm{star}} &= \frac{M_{*,\mathrm{II}}}{M_{\mathrm{cold}}} t_{\mathrm{cold,ff}}, \\ t_{\mathrm{cool}} &= \frac{M_{\mathrm{cold}}}{M_{\mathrm{hot}}} t_{\mathrm{dyn}}, \\ t_{\mathrm{acc}} &= \frac{M_{\mathrm{hot}}}{\frac{\Omega_{\mathrm{b}}}{\Omega_{\mathrm{m}}} M_{\mathrm{vir,peak}} - \left(M^0_{\mathrm{cold}} + M^0_{\mathrm{hot}} + M^0_{*,\mathrm{II}} + M^0_{\mathrm{out}}\right)} \Delta t_z. \end{aligned} \tag{2.12}$$

Using these, we set the subcycle time-step following:

$$\delta t_i = 0.25 \min(\mathrm{t_{star}}, \mathrm{t_{cold}}, \mathrm{t_{acc}}, \mathrm{t_{dyn}}, \Delta \mathrm{t_z}). \tag{2.13}$$

The number of subcycle time-steps (N_{sub}) is then determined by the above mentioned physical processes. We make sure that $\Sigma_{i=1}^{N_{\mathrm{sub}}} \delta t_i = \Delta t_z$ in the code. If the computed $\delta t_{\mathrm{final}}$ leads to $\Sigma_{i=1}^{N_{\mathrm{sub}}} \delta t_i > \Delta t_z$, we then force $\delta t_{\mathrm{final}} = \Delta t_z - \Sigma_{i=1}^{N_{\mathrm{sub}}-1} \delta t_i$. Our use of adaptive time-steps for the subcycles guarantees that mechanical and radiative feedback are sufficiently resolved in time, but significantly reduces the computational cost compared to what would be required using a small fixed time-step.

2.2.4 Population II Stellar Feedback

During their stellar lifetime, massive stars ($> 8 M_\odot$) emit copious amount of ionising photons. Furthermore, stars with masses in the range $10 - 40 M_\odot$ die as CCSNe (Heger and Woosley, 2002, 2010). Each CCSN produces an amount of energy $E_{\mathrm{SN}} = 10^{51}$ erg and the energy is injected into the interstellar medium (ISM). Here we describe how the photons emitted by massive stars and the energy from SNe affect the ISM in our model.

1. **Photoheating**

   The ionising photons heat up the dense cold gas surrounding the star forming region. For stars with different masses, we calculate a time-averaged mass conversion rate, $\langle \dot{M}_{\mathrm{heat}} \rangle$, over their lifetimes.

   Firstly, the mass which is enclosed in the H II region of a D-type I-front can be described as a function of t

   $$M_{\mathrm{H\,II}} = m_{\mathrm{H}} \frac{4\pi}{3} R_{\mathrm{I}}^3(t) n_{\mathrm{H\,II}}(t) \ (\mathrm{g}), \tag{2.14}$$

   where $n_{\mathrm{H\,II}}(t)$ is the number density at time t inside the H II region and m_{H} is the atomic mass. For simplicity, we ignore helium. The number density inside the HII region is computed by

$$n_{\text{HII}}(t) = n_{\text{cold}}^{\text{den}} \left(\frac{R_{\text{D}}}{R_{\text{I}}(t)} \right)^{3/2} (\text{cm}^{-3}), \tag{2.15}$$

where $n_{\text{cold}}^{\text{den}}$ is the number density of the dense gas. The radius that the I-front reaches at time t, $R_{\text{I}}(t)$ is computed by (Spitzer, 1978)

$$R_{\text{I}}(t) = R_{\text{D}} \left[1 + \frac{7}{4} \frac{c_{\text{s}}(t - t_{\text{D}})}{R_{\text{D}}} \right]^{4/7} (\text{cm}), \tag{2.16}$$

where $c_{\text{s}} = 11.4 \left(\frac{\text{T}_{\text{ion}}}{T_4} \right)^{1/2} \times 10^5 \text{cms}^{-1}$ is the sound speed and we assume for simplicity a fixed temperature $T_{\text{ion}} = 10^4\text{K}$. The distance that the I-front reaches when it enters D-type expansion, R_{D}, is

$$R_{\text{D}} = \left(\frac{3Q}{4\pi (n_{\text{cold}}^{\text{den}})^2} \alpha_{\text{B}} \right)^{1/3} (\text{cm}), \tag{2.17}$$

and the time it needs to reach this distance, t_{D}, is given by

$$t_{\text{D}} = \ln \left(\frac{842}{23} \left(\frac{Q}{10^{48}} \right)^{1/3} \left(\frac{n_{\text{cold}}^{\text{den}}}{10^3} \right)^{1/3} \right) \tau(\text{s}), \tag{2.18}$$

where $\tau = (\alpha_{\text{B}} n_{\text{cold}}^{\text{den}})^{-1}\text{s}$ is the recombination time.

We can then express $M_{\text{HII}}(t)$ as

$$\begin{aligned} &M_{\text{HII}}(t) \\ &= \frac{4\pi m_{\text{H}}}{3} R_{\text{D}}^3 \left[1 + \frac{7}{4} \frac{c_{\text{s}}(t - t_{\text{D}})}{R_{\text{D}}} \right]^{12/7} n_{\text{cold}}^{\text{den}} \left(\frac{R_{\text{D}}}{R_{\text{I}}(t)} \right)^{3/2} \\ &= m_{\text{H}} n_{\text{cold}}^{\text{den}} \frac{4\pi}{3} R_{\text{D}}^3 \left[1 + \frac{7}{4} \frac{c_{\text{s}}(t - t_{\text{D}})}{R_{\text{D}}} \right]^{6/7} (\text{g}). \end{aligned} \tag{2.19}$$

Finally, we can use the expression above to write down the rate at which gas is incorporated into the HII region, converting it from the cold phase in our model to the hot phase. This is essentially the time derivative of Eq. 2.19 and we obtain the instantaneous mass conversion rate of a massive star

$$\begin{aligned}\dot{M}_{\rm heat} &= 10^{-25} m_{\rm H} n_{\rm cold}^{\rm den} R_{\rm D}^2 c_{\rm s} \\ &\left[1 + \frac{7}{4}\frac{c_{\rm s}(t - t_{\rm D})}{R_{\rm D}}\right]^{-1/7} \quad [M_\odot {\rm yr}^{-1}],\end{aligned} \tag{2.20}$$

where $m_{\rm H} = 1.66 \times 10^{-24}$ g is the mass of a hydrogen atom, $n_{\rm cold}^{\rm den} = 10^3$ cm^{-3} is the number density, $c_{\rm s,ion} = 11.4\,({\rm T_{ion}}/10^4)^{1/2} \times 10^5$ cm/s is the sound speed, and ${\rm T_{ion}} = 10^4$K is the temperature of the ionised gas. We denote the distance between the ionising front and the star, and the time it takes when the I-front reaches D-type expansion, as $R_{\rm D}$ and $t_{\rm D}$, respectively.

As an example, we show the mass conversion rates for 10, 25 and 63$M_\odot$ stars over the course of their lives in Figure 2.2. These values were computed assuming a cold gas density $n_{\rm cold}^{\rm den} = 1000$ cm^{-3}, but are only weakly sensitive to this choice. After a decrease in a small fraction of the stellar lifetime, $\dot{M}_{\rm heat}$ stays almost constant until the end of the stellar lifetime. Based on Table 6 in Schaerer (2002), we find that the ionising photon rate Q of massive stars (7-150$M_\odot$) can be well described with the following equation,

$$\begin{aligned}\log_{10} Q = 27.8 &+ 30.68\left(\frac{M_{\rm star}}{M_\odot}\right) \\ &- 14.8\left(\frac{M_{\rm star}}{M_\odot}\right)^2 + 2.59\left(\frac{M_{\rm star}}{M_\odot}\right)^3.\end{aligned} \tag{2.21}$$

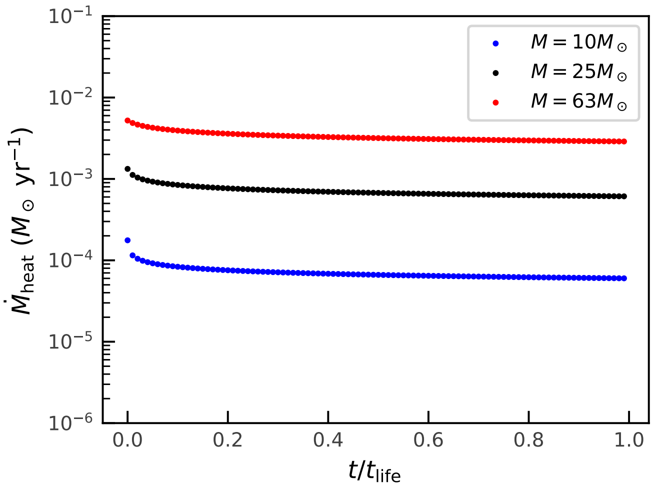

Figure 2.2: Mass conversion rate of 10, 25, and 63 $M_\odot$ stars throughout their lifetimes. These values are computed using Equation 2.20 with an assumed cold gas density of $n_{\rm cold}^{\rm den} = 1000\,{\rm cm}^{-3}$.

We note that $R_{\rm D}^2$, $t_{\rm D}$ and therefore $\dot{M}_{\rm heat}$ show a non-linear behaviour with the ionising photon emission rate. Stars that form in a cluster are less efficient at heating their ambient medium than isolated stars. Since there is no spatial information inside the halo available from the *Caterpillar* trees, we assume that 90% of the massive stars form in the very central region of the halo that can be considered as one big star cluster. We add the ionising photons from these 90% of massive stars and calculate one $\dot{M}_{\rm heat,cl}$. For the rest of massive stars (10%), we assume that they form in isolation and calculate a $\dot{M}_{\rm heat,iso}$ for each of them. In time-step i, we sum up the contributions from all of the massive stars to calculate the mass that is converted from cold phase to hot phase,

$$\delta M_{\rm heat,i} = \left(\dot{M}_{\rm heat,cl} + \Sigma_{j=1}^{N_{\rm iso}} \langle \dot{M}^{j}_{\rm heat,iso} \rangle \right) \delta t_i. \tag{2.22}$$

As shown above, $\dot{M}_{\rm heat}$ does not depend linearly on the number of ionising photons. Therefore, whether stars are in clusters or isolation may be important to the stellar feedback. We show two extreme cases of star clustering: 1) all stars reside in the very central region and can be considered as one cluster, and 2) all stars are in isolation. The resulting SMHM relations of these two cases are shown in Figure 2.3. The distinct difference lies in the most massive haloes, i.e., the MW in each *Caterpillar* tree. In such haloes, the number of massive stars is bigger and therefore the importance of $\dot{M}_{\rm heat}$ emerges.

In mini-haloes with $T_{\rm vir} < 10000$ K, the mass heated by ionisation is added directly to the outflow. To determine $T_{\rm vir}$, we use the expression

$$T_{\rm vir} = \frac{G M_{\rm vir,peak} m_{\rm H}}{R_{\rm vir} k_{\rm B}}, \tag{2.23}$$

$G = 6.67 \times 10^{-8}\,{\rm cm^3\,g^{-1}\,s^{-2}}$ is the gravitational constant, $M_{\rm vir,peak}$ is the largest virial mass that the halo ever attains up to the current redshift, and $k_{\rm B} = 1.38 \times 10^{-16}\,{\rm cm^2\,g\,s^{-2}\,K^{-1}}$ is the Boltzmann constant. The reasoning behind this approximation is that these haloes are not massive enough to gravitationally bind ionised gas, as the escape velocity from these haloes is smaller than the speed of sound in the ionised gas. Sufficiently strong ionising radiation has been shown to cause efficient outflows in such haloes, quickly removing most of the gas from them (Whalen et al., 2008; Chiaki et al., 2018; Schauer et al., 2017). Visbal et al. (2017) demonstrated that haloes above the atomic cooling limit can bind ionised gas and collapse under their own gravity.

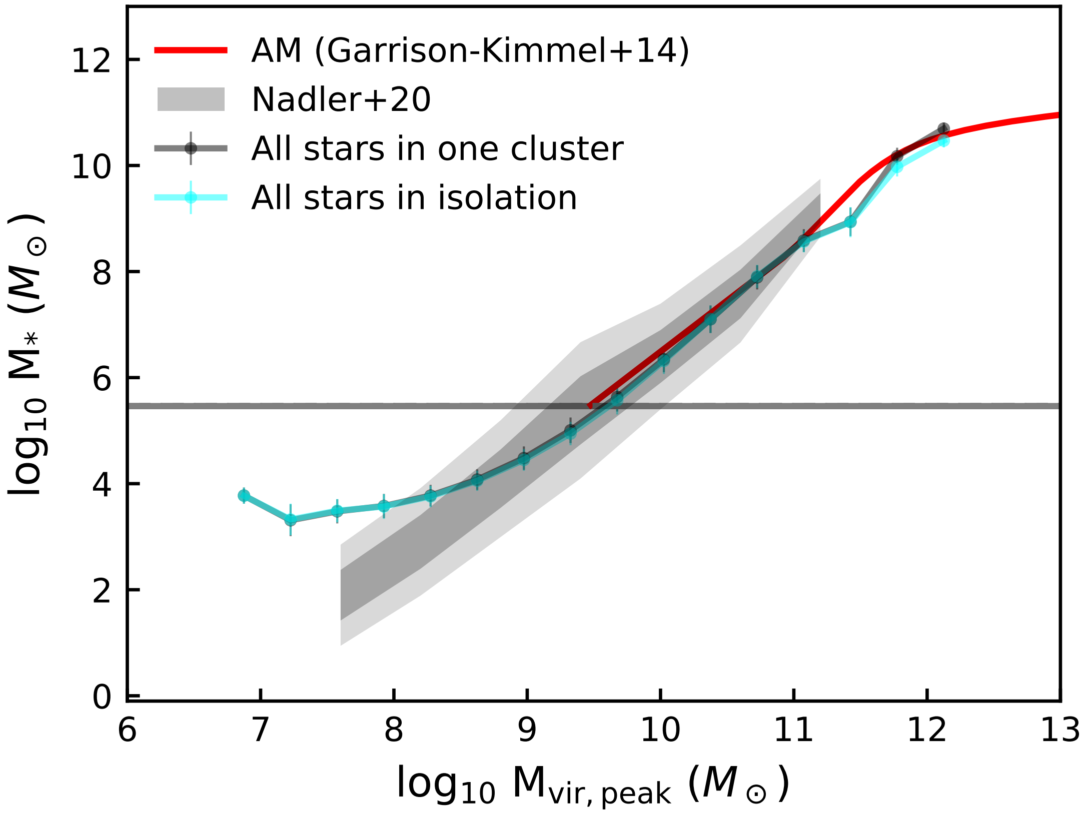

Figure 2.3: We show the SMHM relation from 30 *Caterpillar* trees if we assume that all massive stars reside in one big cluster in black and that all massive stars form in isolation in cyan.

2. **Supernovae**

Since we do not have spatial information on the gas inside a halo, we assume that a fraction of the gas absorbs the supernovae energy and is then unbound from the halo, i.e., gas is preferentially lost entirely rather than recycled via a galactic fountain. We compare the total supernovae energy deposited in the gas during time-step i with the gravitational binding energy of gas in order to determine how much gas is ejected during the time-step, i.e., $\delta M^i_{\rm out,cold}$ and $\delta M^i_{\rm out,hot}$.

We assume a uniform density inside each baryonic content. There are four components that contribute to the total binding energy: the dark matter halo, the cold gas, the hot gas and the stars. Stars and cold gas reside in the same region, that we define as the disk (at a radius of $R_{\rm rs}$). The contribution from each component can be calculated separately and summed up later, i.e.,

$$\begin{aligned} &E_{\mathrm{bind,hot}} \\ &= \int_0^{R_{\mathrm{vir}}} dM_{\mathrm{hot}} U(r) \\ &= E_{\mathrm{hot,DM}} + E_{\mathrm{hot,disk}} + E_{\mathrm{hot,hot}}, \end{aligned} \tag{2.24}$$

and

$$\begin{aligned} &E_{\mathrm{bind,cold}} \\ &= \int_0^{R_{\mathrm{s}}} dM_{\mathrm{cold}} U(r) \\ &= E_{\mathrm{cold,DM}} + E_{\mathrm{cold,stellar}} + E_{\mathrm{cold,cold}} + E_{\mathrm{cold,hot}}, \end{aligned} \tag{2.25}$$

where U is the potential energy. We first write down the detailed derivation of the three components in Eq. 2.24.

$$\begin{aligned} &\mathrm{E}_{\mathrm{hot,hot}} = \int_0^{R_{\mathrm{vir}}} \frac{\mathrm{G} M_{\mathrm{hot}}(r) dM_{\mathrm{hot}}}{R} \\ &= \int_0^{R_{\mathrm{vir}}} \frac{\mathrm{G} \frac{4}{3}\pi r^3 \rho_{\mathrm{hot}} 4\pi r^2 \rho_{\mathrm{hot}} dr}{r} \\ &= \frac{3}{5}\frac{\mathrm{G} M_{\mathrm{hot}}^2}{R_{\mathrm{vir}}}. \end{aligned} \tag{2.26}$$

$$\begin{aligned} &\mathrm{E}_{\mathrm{hot,disk}} = \int_0^{R_{\mathrm{vir}}} dM_{\mathrm{hot}} \int_r^{\infty} \frac{\mathrm{G} M_{\mathrm{disk}}(R)}{R^2} dR \\ &= \int_0^{R_{\mathrm{s}}} dM_{\mathrm{hot}} \left[\int_r^{R_{\mathrm{s}}} \frac{\mathrm{G} M_{\mathrm{disk}}(R)}{R^2} + \int_{R_{\mathrm{s}}}^{\infty} \frac{\mathrm{G} M_{\mathrm{disk}}}{R^2} \right] dR + \int_{R_{\mathrm{s}}}^{R_{\mathrm{vir}}} dM_{\mathrm{hot}} \frac{\mathrm{G} M_{\mathrm{disk}}}{r} \\ &= 4\pi \rho_{\mathrm{hot}} \mathrm{G} \left[\frac{2\pi(\frac{R_{\mathrm{s}}^5}{3} - \frac{R_{\mathrm{s}}^5}{5})\rho_{\mathrm{disk}}}{3} + \frac{R_{\mathrm{s}}^3}{3}\frac{M_{\mathrm{disk}}}{R_{\mathrm{s}}} \right] + 2\pi \rho_{\mathrm{hot}} (R_{\mathrm{vir}}^2 - R_{\mathrm{s}}^2) G M_{\mathrm{disk}} \\ &= \left(\frac{3R_{\mathrm{s}}}{2R_{\mathrm{vir}}} - \frac{13 R_{\mathrm{s}}^3}{30 R_{\mathrm{vir}}^3} \right) \frac{\mathrm{G} M_{\mathrm{hot}} M_{\mathrm{disk}}}{R_{\mathrm{s}}}, \end{aligned} \tag{2.27}$$

where $M_{\mathrm{disk}} = M_{\mathrm{stellar}} + M_{\mathrm{cold}}$.

$$\begin{aligned}
\mathrm{E}_{\mathrm{hot,DM}} &= \int_0^{R_{\mathrm{vir}}} dM_{\mathrm{hot}} \int_r^{\infty} \frac{\mathrm{G}M_{\mathrm{DM}}(R)}{R^2} dR \\
&= \int_0^{R_{\mathrm{vir}}} dM_{\mathrm{hot}} \int_r^{\infty} \frac{\mathrm{G}}{R^2} dR \int_0^{R} 4\pi r'^2 \frac{\rho_0}{\frac{r'}{R_{\mathrm{s}}}\left(1+\frac{r'}{R_{\mathrm{s}}}\right)^2} dr' \\
&= 4\pi \mathrm{G}\rho_0 R_{\mathrm{s}}^3 \int_0^{R_{\mathrm{vir}}} dM_{\mathrm{hot}} \int_r^{\infty} \frac{dR}{R^2} \int_0^{R} \frac{r'}{\left(R_{\mathrm{s}}+r'\right)^2} dr' \\
&= 16\pi^2 \mathrm{G}\rho_0\rho_{\mathrm{hot}} R_{\mathrm{s}}^3 \int_0^{R_{\mathrm{vir}}} r\left(\ln\left(R_{\mathrm{s}}+r\right) - \ln R_{\mathrm{s}}\right) dr \\
&= \frac{3\mathrm{G}M_{\mathrm{vir,peak}}M_{\mathrm{hot}}}{R_{\mathrm{vir}}\left[\frac{-R_{\mathrm{vir}}}{R_{\mathrm{s}}+R_{\mathrm{vir}}} + \ln\frac{R_{\mathrm{s}}+R_{\mathrm{vir}}}{R_{\mathrm{s}}}\right]} \left[\left(\frac{1}{2} - \frac{R_{\mathrm{s}}^2}{2R_{\mathrm{vir}}^2}\right)\ln\left(\frac{R_{\mathrm{s}}+R_{\mathrm{vir}}}{R_{\mathrm{s}}}\right) + \frac{R_{\mathrm{s}}}{2R_{\mathrm{vir}}} - \frac{1}{4}\right]
\end{aligned} \tag{2.28}$$

Similarly, the four components in Eq. 2.25 are shown in Eqs. 2.29-2.32.

$$\begin{aligned}
E_{\mathrm{cold,stellar}} &= \int_0^{R_{\mathrm{s}}} dM_{\mathrm{cold}} \int_r^{\infty} \frac{\mathrm{G}M_*(R)}{R^2} dR \\
&= \int_0^{R_{\mathrm{s}}} dM_{\mathrm{cold}} \left[\int_r^{R_{\mathrm{s}}} \frac{\mathrm{G}M_*(R)}{R^2} dR + \int_{R_{\mathrm{s}}}^{\infty} \frac{\mathrm{G}M_*(R)}{R^2} dR\right] \\
&= \int_0^{R_{\mathrm{s}}} 4\pi r^2 \rho_{\mathrm{cold}} dr \left[\frac{\mathrm{G}2\pi\rho_{\mathrm{star}}(R_{\mathrm{s}}^2 - r^2)}{3} + \frac{\mathrm{G}M_*}{R_{\mathrm{s}}}\right] \\
&= 4\pi\rho_{\mathrm{cold}} \left[\frac{\mathrm{G}2\pi\rho_{\mathrm{star}}(\frac{{R_{\mathrm{s}}}^3}{3}R_{\mathrm{s}}^2 - \frac{{R_{\mathrm{s}}}^5}{5})}{3} + \frac{\mathrm{G}M_*{R_{\mathrm{s}}}^3}{3R_{\mathrm{s}}}\right] \\
&= \frac{6\mathrm{G}M_{\mathrm{cold}}M_*}{5R_{\mathrm{s}}}
\end{aligned} \tag{2.29}$$

$$
\begin{aligned}
E_{\mathrm{cold,hot}} &= \int_0^{R_{\mathrm{s}}} dM_{\mathrm{cold}} \int_r^{\infty} \frac{\mathrm{G}M_{\mathrm{hot}}(R)}{R^2} dR \\
&= \int_0^{R_{\mathrm{s}}} dM_{\mathrm{cold}} \left[\int_r^{R_{\mathrm{vir}}} \frac{\mathrm{G}M_{\mathrm{hot}}(R)}{R^2} dR + \int_{R_{\mathrm{vir}}}^{\infty} \frac{\mathrm{G}M_{\mathrm{hot}}(R)}{R^2} dR \right] \\
&= \int_0^{R_{\mathrm{s}}} \rho_{\mathrm{cold}} 4\pi r^2 dr \left[\frac{\mathrm{G}\rho_{\mathrm{hot}} 2\pi (R_{\mathrm{vir}}^2 - r^2)}{3} + \frac{\mathrm{G}M_{\mathrm{hot}}}{R_{\mathrm{vir}}} \right] \\
&= \rho_{\mathrm{cold}} 4\pi \left[\frac{\mathrm{G}\rho_{\mathrm{hot}} 2\pi (\frac{R_{\mathrm{s}}^3}{3} R_{\mathrm{vir}}^2 - \frac{R_{\mathrm{s}}^5}{5})}{3} + \frac{\mathrm{G}M_{\mathrm{hot}} R_{\mathrm{s}}^3}{3 R_{\mathrm{vir}}} \right] \\
&= \frac{\mathrm{G}M_{\mathrm{hot}} M_{\mathrm{cold}}}{R_{\mathrm{vir}}} \left(\frac{3}{2} - \frac{3 R_{\mathrm{s}}^2}{10 R_{\mathrm{vir}}^2} \right)
\end{aligned}
\tag{2.30}
$$

$$
\begin{aligned}
E_{\mathrm{cold,DM}} &= \int_0^{R_{\mathrm{s}}} dM_{\mathrm{cold}} \int_r^{\infty} \frac{\mathrm{G}M_{\mathrm{DM}}(R)}{R^2} dR \\
&= 16\pi^2 \mathrm{G} \rho_0 \rho_{\mathrm{cold}} R_{\mathrm{s}}^3 \int_0^{R_{\mathrm{s}}} r \left(\ln\left(R_{\mathrm{s}} + r\right) - \ln R_{\mathrm{s}} \right) dr \\
&= \frac{3\mathrm{G}M_{\mathrm{vir,peak}} M_{\mathrm{cold}}}{4 R_{\mathrm{s}} \left[\frac{-R_{\mathrm{vir}}}{R_{\mathrm{s}} + R_{\mathrm{vir}}} + \ln \frac{R_{\mathrm{s}} + R_{\mathrm{vir}}}{R_{\mathrm{s}}} \right]}
\end{aligned}
\tag{2.31}
$$

$$
E_{\mathrm{cold,cold}} = \frac{3\mathrm{G}M_{\mathrm{cold}}^2}{5 R_{\mathrm{s}}}
\tag{2.32}
$$

Finally, the total binding energy of hot gas can be described by the following analytic equation,

$$
\begin{aligned}
\mathrm{E}_{\mathrm{bind,hot}}^{i} &= \frac{3\mathrm{G}M_{\mathrm{vir,peak}} M_{\mathrm{hot}}^{i}}{R_{\mathrm{vir}} \left[\frac{-R_{\mathrm{vir}}}{R_{\mathrm{s}} + R_{\mathrm{vir}}} + \ln \frac{R_{\mathrm{s}} + R_{\mathrm{vir}}}{R_{\mathrm{s}}} \right]} \times \\
&\left[-\frac{1}{4} + \frac{1}{2} \left(1 - \frac{R_{\mathrm{s}}^2}{R_{\mathrm{vir}}^2} \right) \ln \frac{R_{\mathrm{s}} + R_{\mathrm{vir}}}{R_{\mathrm{s}}} + \frac{1}{2} \frac{R_{\mathrm{s}}}{R_{\mathrm{vir}}} \right] \\
&+ \left(\frac{3 R_{\mathrm{s}}}{2 R_{\mathrm{vir}}} - \frac{13 R_{\mathrm{s}}^3}{30 R_{\mathrm{vir}}^3} \right) \frac{\mathrm{G}M_{\mathrm{disk}}^{i} M_{\mathrm{hot}}^{i}}{R_{\mathrm{s}}} + \frac{3}{5} \frac{\mathrm{G}(M_{\mathrm{hot}}^{i})^2}{R_{\mathrm{vir}}},
\end{aligned}
\tag{2.33}
$$

where $M_{\mathrm{vir,peak}}$ is the virial halo mass a halo ever attains up to the current redshift, R_{s} is the scale radius of the dark matter halo, which we assume to follow an NFW profile (Navarro et al., 1996), R_{vir} is the virial radius of the halo and $M^i_{\rm disk}$ is the mass of the disk. Similarly, the binding energy of cold gas can be described by

$$\begin{aligned}
\mathrm{E}^i_{\rm bind,cold} = & \frac{3\mathrm{G}M_{\rm vir,peak}M^i_{\rm cold}}{4R_{\rm s}\left[\frac{-R_{\rm vir}}{R_{\rm s}+R_{\rm vir}}+\ln\frac{R_{\rm s}+R_{\rm vir}}{R_{\rm s}}\right]} \\
& + \frac{6\mathrm{G}M^{\mathrm{i}}_{\rm cold}M_*}{5R_{\rm s}} + \frac{\mathrm{G}M^{\mathrm{i}}_{\rm hot}M^{\mathrm{i}}_{\rm cold}}{R_{\rm vir}}\left(\frac{3}{2}-\frac{3R_{\rm s}^2}{10R_{\rm vir}^2}\right) \\
& + \frac{3\mathrm{G}(M^{\mathrm{i}}_{\rm cold})^2}{5R_{\rm s}}.
\end{aligned} \tag{2.34}$$

We adopt an outflow efficiency with a functional form of

$$\gamma_{\rm out} = \left(\frac{M_{\rm vir,peak}}{M_{\rm norm}}\right)^{\alpha_{\rm out}}, \tag{2.35}$$

where $M_{\rm norm}$ is the normalisation mass. Both $M_{\rm norm}$ and $\alpha_{\rm out}$ are free parameters in our model. We adopt fiducial values of $M_{\rm norm} = 10^{10.5}M_\odot$ and $\alpha_{\rm out} = 0.72$ and explain their calibration in Section 2.3. Supernovae are assumed to explode in warm, low density regions created by prior photoionisation. Therefore, we first calculate how much hot gas will be removed,

$$\delta M^i_{\rm out,hot} = \min\left(\frac{E^i_{\rm SNe}/\gamma_{\rm out}}{E^i_{\rm bind,hot}}M^i_{\rm hot}, M^i_{\rm hot}\right), \tag{2.36}$$

where $E^i_{\rm SNe}$ is the sum of supernovae energies that occur in this time-step. If $E^i_{\rm SNe}/\gamma_{\rm out} > E^i_{\rm bind,hot}$, we then calculate a "leftover" supernovae energy $E^i_{\rm SNe,left}/\gamma_{\rm out} = E^i_{\rm SNe}/\gamma_{\rm out} - E^i_{\rm bind,hot}$. In other words, we only consider the ejection of cold gas if $E^i_{\rm SNe,left} > 0$ and obtain

$$\delta M^i_{\rm out,cold} = \min\left(\frac{E^i_{\rm SNe,left}/\gamma_{\rm out}}{E^i_{\rm bind,cold}}M^i_{\rm cold}, M^i_{\rm cold}\right). \tag{2.37}$$

2.2.5 Ionising and enriching volumes (internal/external enrichment)

Reionisation feedback and external enrichment are modelled according to the description in Magg et al. (2018). Each star-forming halo has an ionised bubble around it. These bubbles are launched at the virial radius and change their sizes based on the ionising photon budget, i.e., they expand if the halo emits more ionising photons and shrink if there are more recombination events than ionising photons emitted.

The volume V of the ionised region is therefore updated from a time-step i to the next time-step $i+1$ as

$$V_{i+1} = \left(V_i + \frac{\dot{N}_{\mathrm{ion}} \Delta t}{n} \right) \left(1 + \Delta t n \alpha_{\mathrm{B}} C\right)^{-1}, \tag{2.38}$$

where $\dot{N}_{\mathrm{ion}}$ is the emission rate of ionising photons, n is the mean IGM nucleon number density, $C = 3$ is the clumping factor of the IGM (Robertson et al., 2013) and $\alpha_{\mathrm{B}} = 2.6 \times 10^{-13}\,\mathrm{cm}^3\,\mathrm{s}^{-1}$ is the case B recombination rate coefficient of hydrogen at 10^4 K (Draine, 2011). When haloes merge the volumes of the ionised bubbles are added up, as the sum conserves the number of ionisations.

Furthermore, each halo has a metal-enriched region around it. The expansion of the metal-enriched shell is modelled by a momentum driven snowplough, where the momentum is calculated based on the assumption that all ejected material has a constant velocity of $v_{\mathrm{out}} = 110\,\mathrm{km\,s}^{-1}$ and slows down by sweeping up the intergalactic medium. This assumption leads to an expansion velocity of

$$v_{\mathrm{II}} = v_{\mathrm{out}} \frac{M_{\mathrm{out}}}{M_{\mathrm{out}} + \frac{4}{3}\pi \rho_b \left(R_{\mathrm{enr}}^3 - R_{\mathrm{vir}}^3\right)}, \tag{2.39}$$

where ρ_b is the mean IGM mass density and R_{enr} is the radius of the currently enriched region around the halo. Derivations and more details of the implementation of both of the methods can be found in Magg et al. (2018).

2.3 Calibration

In this section, we study the influence of the free parameters in our Pop II SF model and describe how we determine their fiducial values. These parameters are Pop II SF efficiency η_{II} (Eq. 2.9), exponent α_{out}, and normalisation mass M_{norm} in the outflow efficiency γ_{out} (Eq. 2.35), which are defined in Section 2.2.1. In simulations other than the fiducial one, only one parameter is varied.

2.3.1 Observables used in calibration

1. **MW properties at $z = 0$**

   We calibrate our model to the observed MW properties at $z = 0$, which are its stellar mass M_* (stars that survive until $z = 0$) and cold gas mass M_{cold}.

2. **Cumulative stellar mass function (SMF) of the satellites**

   The SMHM relation connects the host halo and the galaxy, but it does not provide direct information on how many satellites there are in the MW system. Therefore, we compare the cumulative stellar mass function obtained from A-SLOTH simulated satellites with the one from observed MW satellites (McConnachie, 2012; Muñoz et al., 2018). To quantify the difference, we perform a two-sample Kolmogorov-Smirnov (K-S) test (Kolmogorov, 1933; Smirnov, 1939; Massey, 1951) on our cumulative stellar mass function and the observed one. We retrieve the KS statistic from the two-sample K-S test, which represents the maximal distance between the two stellar mass functions and is normalised to have a value between 0 and 1. The smaller the KS statistic, the more-alike the two distributions are. Additionally, we retrieve a p-value from the same two-sample K-S test, which tells us whether we can reject the hypothesis that the two distributions are the same. The higher the p-value, the less certain we are to reject the hypothesis.

3. **Stellar mass-to-halo mass relation**

   We compare the SMHM relation produced by A-SLOTH with the one derived by Garrison-Kimmel et al. (2014) (hereafter GK14), who used the abundance matching (AM) to derive their SMHM relation. The underlying assumption of the AM technique is that the number of galaxies with stellar masses above a certain mass is the same as the number of haloes with virial masses above a certain mass (Kravtsov et al., 2004; Tasitsiomi et al., 2004; Vale and Ostriker, 2004; Conroy et al., 2006; Conroy and Wechsler, 2009; Guo et al., 2010; Behroozi et al., 2010). To quantify the difference between our SMHM relation and the one in GK14, we apply a mean-squared-error analysis. Due to observational completeness, the SMHM relation in GK14 is robust in the range $M_* = 10^5 - 10^8 M_\odot$. For A-SLOTH simulated galaxies with stellar masses in this range, we calculate their expected stellar mass if they follow the SMHM relation in GK14, $\mathrm{AM}(M_{\mathrm{vir,peak}})$. The mean-squared-error χ^2 is then

$$\chi^2 = \frac{1}{N_{\mathrm{gal}}} \sum_{i=1}^{N_{\mathrm{gal}}} \left(M_{*,i} - \mathrm{AM}(\mathrm{M_{vir,i}})\right)^2, \tag{2.40}$$

where

$$\begin{aligned} \log_{10}(\mathrm{AM}(\mathrm{M}_*)) = (&\log_{10}(5.457 \times 10^{10}\ \mathrm{M}_*)+ \\ &f_{\mathrm{bwc}}(\log_{10}(\mathrm{M}_*/3.266 \times 10^{11}\ \mathrm{M}_*)) - \mathrm{f}_{\mathrm{bwc}}(0)), \end{aligned} \tag{2.41}$$

and $M_{\mathrm{vir,i}}$ and $M_{*,i}$ are given in solar masses. The fitting function f_{bwc} is given in Behroozi et al. (2013) that

$$\begin{aligned} f_{\mathrm{bwc}}(x) = &- \log_{10}(10^{\alpha \mathrm{x}} + 1)+ \\ &3.508(\log_{10}(1 + \exp(\mathrm{x})))^{0.316/(1+\exp(10^{-\mathrm{x}}))}. \end{aligned} \tag{2.42}$$

We adopt $\alpha = 1.92$ following GK14. We further compare the SMHM relation produced by A-SLOTH with the one in Nadler et al. (2020) (hereafter N20), which was inferred from the fit of satellite population discovered by the Dark Energy Survey (DES) and the Panoramic Survey Telescope and Rapid Response System Pan-STARRS1 (PS1).

2.3.2 Free parameters in the Pop II star formation model

Here we explore how A-SLOTH produced observables depend on the free parameters of our Pop II SF model. These observables are the MW properties (Figure 2.4), the SMHM relation, halo occupation fraction (fraction of haloes at given $M_{\mathrm{vir,peak}}$ that hosts a galaxy at $z = 0$), and cumulative SMF of the satellites at $z = 0$ (Figure 2.5). The quantification of differences in the observables are shown in Figure 2.6.

1. **Pop II star formation efficiency**

   We explore Pop II SF efficiency η_{II} with 5 discrete values: [0.1, 0.5, 2.0, 5.0, 10.0]). In Figure 2.4, we observe that the MW stellar mass is similar among the five simulations. On the other hand, the MW cold gas mass has a clear dependence on η_{II}, where the highest η_{II} gives the lowest MW cold gas mass. In Figure 2.5, we observe that the SMHM relations with different η_{II} are all consistent with the one in GK14 and the one in N20 above the observational completeness. Below the observational completeness, haloes with similar $M_{\mathrm{vir,peak}}$ host smaller galaxies at $z = 0$ if we adopt lower η_{II}. Similarly, the difference in the cumulative SMF at $z = 0$ among the five simulations only appears below the observational completeness, where the lowest η_{II} gives the fewest satellites. In Figure 2.6, we observe that η_{II} has a relative small influence on the p-value and χ^2. This indicates that the SF in satellites is mostly feedback regulated,

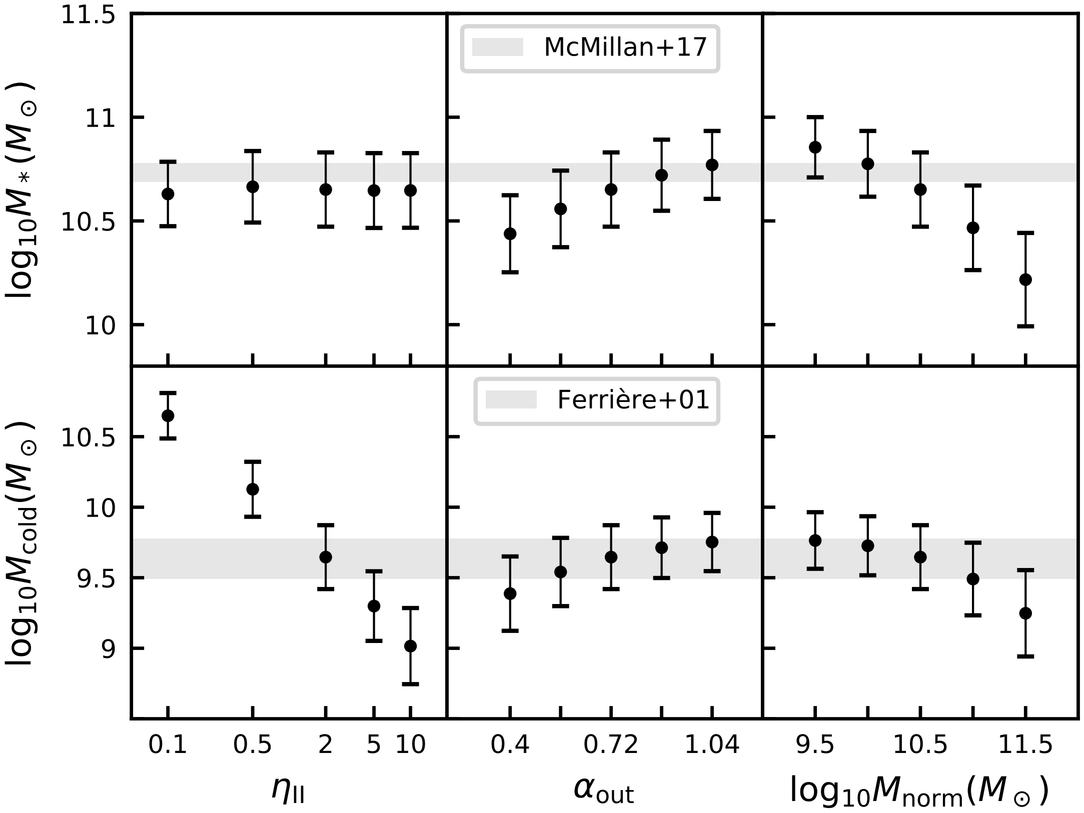

Figure 2.4: We show the mean values and standard deviations of M_* (top panels) and $M_{\rm cold}$ (bottom panels) from 30 *Caterpillar* trees in different simulations, where we tune one of the main parameters in the Pop II SF model. From left to right: Pop II star formation efficiency, exponent, and normalisation mass in the outflow efficiency. The upper and lower grey bands show the observational constraints: $[4.86-6]\times10^{10}M_\odot$ for the observed MW stellar mass and $[3.1-6]\times10^{9}M_\odot$ for the observed MW cold gas mass, respectively.

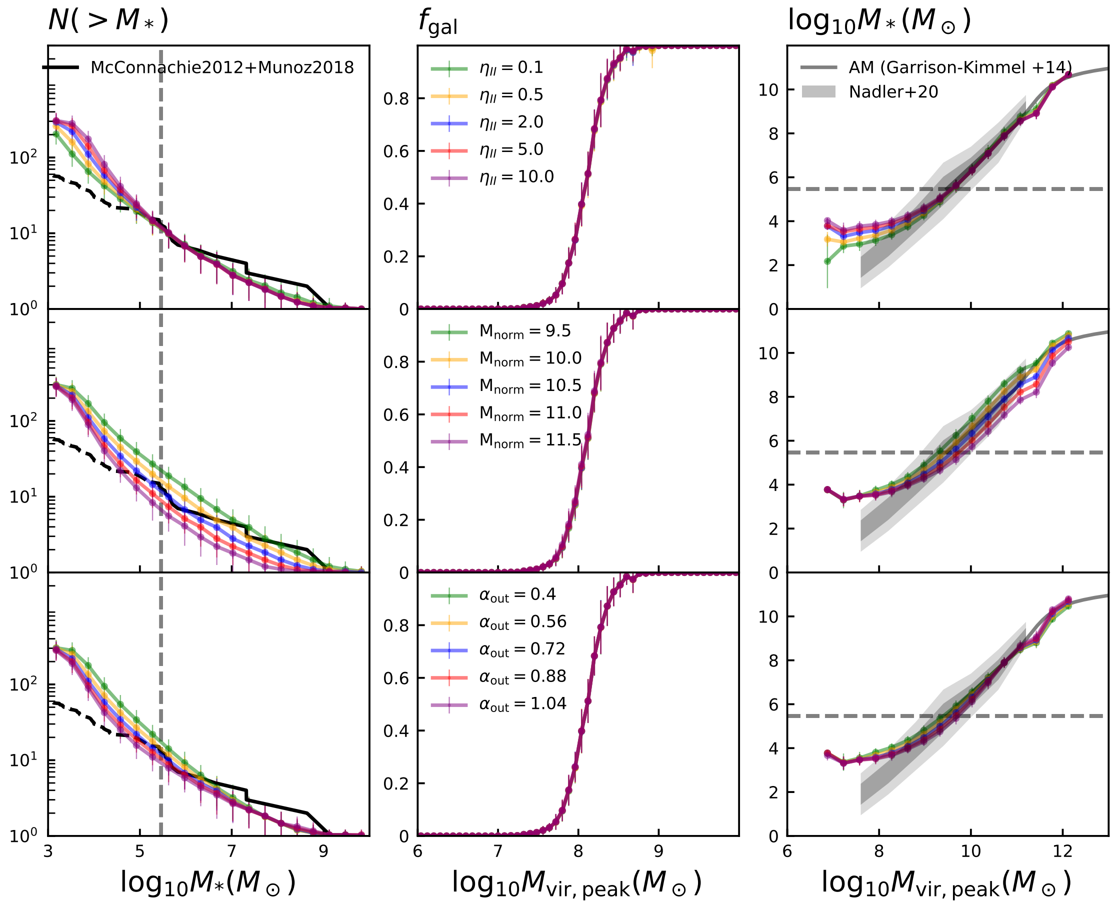

Figure 2.5: From left to right: cumulative SMF of satellites at $z = 0$, halo occupation fraction (fraction of haloes at a given $M_{\rm vir,peak}$ that hosts a galaxy at $z = 0$), and the SMHM relation at $z = 0$. From top to bottom: Pop II star formation efficiency, normalizaton mass, and exponent in the outflow efficiency. In the cumulative SMF panels, we plot the observed one (McConnachie, 2012; Muñoz et al., 2018) in black curve. The solid curve shows the cumulative SMF above the observational completeness, while the dashed curve shows the one below the observational completeness. In the SMHM panels, we plot the SMHM relation in GM14 in grey solid curve and the SMHM relation in N20 in grey contour. The dark grey shows 1 σ region and the light grey contour shows the 2 σ region of their best-fit relation.

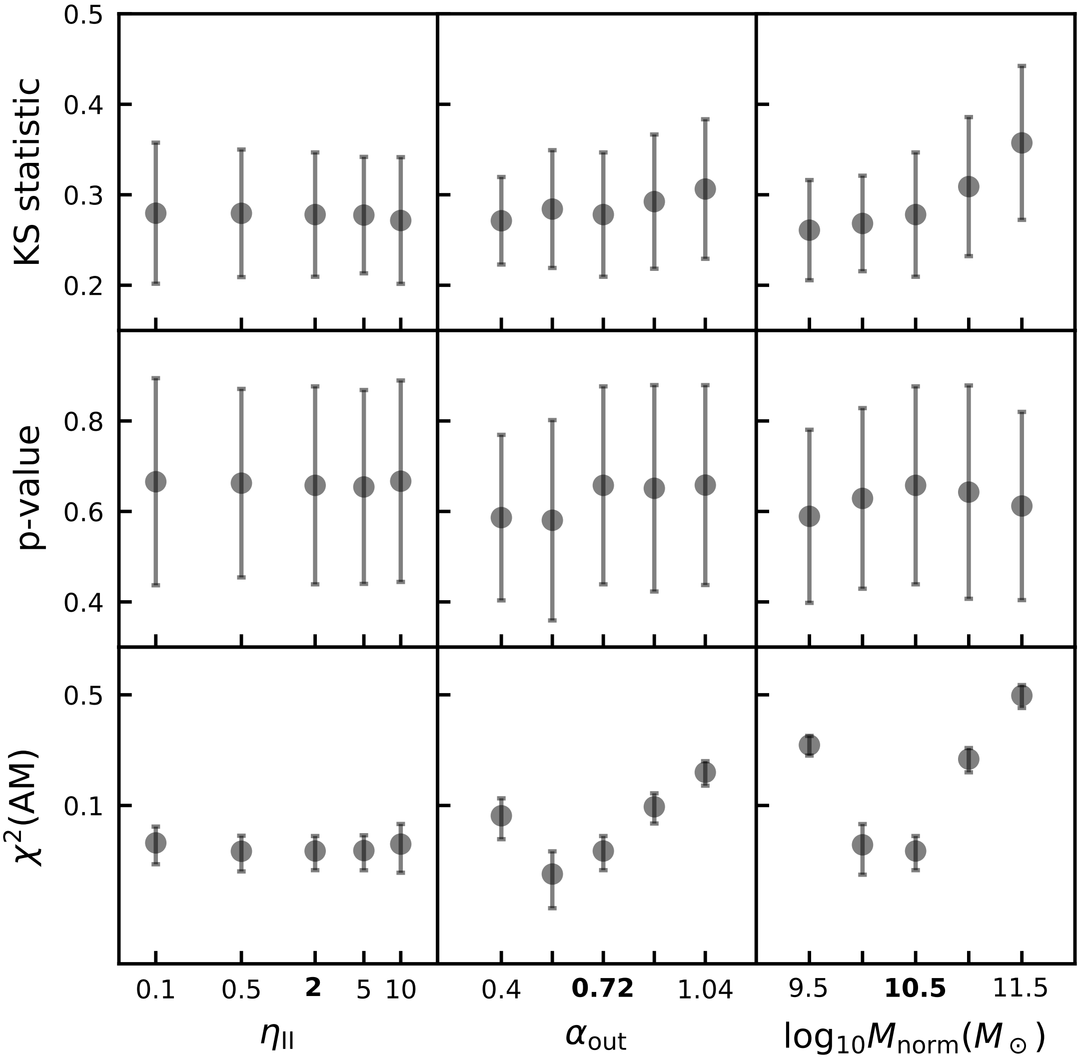

Figure 2.6: Dependence of results on the main parameters. From left to right: the Pop II SF efficiency $\eta_{\rm II}$, the exponent $\alpha_{\rm out}$ and the normalisation mass $M_{\rm norm}$ in the outflow efficiency. We calibrate our model with the observed MW properties, the SMHM relation (mean-squared-error χ^2), and the observed cumulative SMF (p-value and KS statistic). The mean values $\pm 1\sigma$ (standard deviation among 30 *Caterpillar* trees) are shown and the fiducial value is highlighted with bold font.

because they have a shallow potential. The satellites grow slower than the MW throughout the merger histories, therefore, they are less resistant to the stellar feedback. On the other hand, the MW has a much deeper potential and is more capable of retaining gas.

2. **Outflow efficiency**

   As described in Section 2.2.4, the amount of gas removed by SNe is determined by comparing the binding energy of gas and the energy of SNe. We introduce $\gamma_{\mathrm{out}} = (M_{\mathrm{vir,peak}}/M_{\mathrm{norm}})^{\alpha_{\mathrm{out}}}$ such that given the same amount of SN energy, A-SLOTH removes relatively more gas in smaller haloes than in the bigger ones. Here we examine the importance of the normalisation mass M_{norm} and the exponent α_{out}.

   We study 5 different values of M_{norm} spaced regularly in log-space between $10^{9.5} M_{\odot}$ and $10^{11.5} M_{\odot}$. In contrary to η_{II}, we observe that changing M_{norm} leads to a change in the slope of the SMHM above the observational completeness. The slope steepens when M_{norm} decreases, but the stellar mass in the plateau is similar among the five simulations. We also find that adopting $M_{\mathrm{norm}} = 10^{9.5} M_{\odot}$ produces the most luminous satellite while adopting $M_{\mathrm{norm}} = 10^{11.5} M_{\odot}$ produces the least. There is a monotonic decrease in $\overline{M_*}$ and $\overline{M_{\mathrm{cold}}}$ as M_{norm} increases. This is expected because higher M_{norm} gives lower outflow efficiency at fixed $M_{\mathrm{vir,peak}}$ and α_{out}, which means that the halo is less resistant to the SNe. For the exponent α_{out}, we study 5 different values distributed regularly in linear space between 0.40 and 1.04. We find that α_{out} has an impact on the overall slope of the SMHM relation and lower α_{out} gives a flatter SMHM relation. When $\alpha_{\mathrm{out}} > 0$, the gas is more resistant to the SNe in haloes more massive than M_{norm}. Thus, we observe a monotonous increase in $\overline{M_*}$ and $\overline{M_{\mathrm{cold}}}$ as α_{out} increases.

   The slope of the SMHM relation above the observational completeness is mainly influenced by α_{out} and M_{norm} plays the role of the anchor point. On the other hand, the stellar mass in the SMHM plateau is mainly influenced by the Pop II star formation efficiency η_{II}. This leads to flattening of the SMHM relation occurring at different $M_{\mathrm{vir,peak}}$.

3. **Choice of number of Pop II IMF bins**

   We show the averaged number of ionising stars and SNe we get out of every $1000 M_{\odot}$ of stars in our model in Table 2.2 with different number of Pop II

IMF bins $n_{\rm bins,II}$. The difference between 4096 and 8192 bins is less than 0.1% in $\rm N_{ion}$ and identical in $\rm N_{SNe}$. Therefore, we adopt $n_{\rm bins,II} = 4096$ in our model.

$n_{\rm bins,II}$	$\rm N_{ion}$	$\rm N_{SNe}$
128	10.69	7.85
256	10.55	7.75
512	10.48	7.71
1024	10.51	7.73
2048	10.49	7.74
4096	10.49	7.74
8192	10.48	7.74
16384	10.48	7.74

Table 2.2: Averaged number of ionising stars and SNe that we draw from the IMF given a total stellar mass of $1000 M_\odot$.

Based on Figures 2.4-2.6, we find that the following combination of parameters gives the best overall results: $\eta_{\rm II} = 2.$, $\alpha_{\rm out} = 0.72$, and $M_{\rm norm} = 10^{10.5} M_\odot$. The fiducial values of our Pop II SF model are listed in Table 2.3.

Parameter	Fiducial value
$\eta_{\rm II}$	2
$n_{\rm bins,II}$	4096
$M_{\rm bound,II}$ ($M_\odot$)	(0.01, 100)
$M_{\rm crit}$	S21
$\alpha_{\rm out}$	0.72
$M_{\rm norm}$ ($M_\odot$)	$10^{10.5}$
$n^{\rm den}_{\rm cold}$ ($\rm cm^{-3}$)	1000
$v_{\rm BC}$ ($\sigma_{\rm rms}$)	0.8

Table 2.3: The main parameters in our model and their fiducial values.

2.4 Results

2.4.1 Main output

In this section we discuss about the MW properties, cumulative stellar mass function, halo occupation fraction, and SMHM relation from our fiducial model in more details and the scatter among the 30 *Caterpillar* trees.

1. **MW properties at $z = 0$**

   From our fiducial model, we obtain $\overline{M_{\rm cold}} = 5 \times 10^9 M_\odot$, and $\overline{M_*} = 4.84 \times 10^{10} M_\odot$. The corresponding standard deviations are $\sigma_{M_{\rm cold}} = 2.29 \times 10^9 M_\odot$, and $\sigma_{M_*} = 1.77 \times 10^{10} M_\odot$, respectively. Our $\overline{M_*}$ is at the lower limit of the estimate by McMillan (2017) ($[4.86 - 6] \times 10^{10} M_\odot$). The scatter in M_* among the 30 *Caterpillar* trees, $1.77 \times 10^{10} M_\odot$, is larger than the observational uncertainty, $0.57 \times 10^{10} M_\odot$. Since there is no distinction between atomic and molecular phase in our model, we compare our $\overline{M}_{\rm cold}$ with the combination of molecular and cold atomic masses estimated by Ferrière (2001). They estimated a value in the range $[3.1 - 6] \times 10^9 M_\odot$, which covers our result of $\overline{M_{\rm cold}} = 5 \times 10^9 M_\odot$.

2. **Cumulative satellite stellar mass function**

   In Figure 2.7, we show the cumulative stellar mass function (SMF) of MW satellite galaxies from our fiducial model in grey and the observed one (McConnachie, 2012; Muñoz et al., 2018) in blue. The scatter among the 30 *Caterpillar* trees is larger at high mass end but decreases as M_* decreases. The number of satellites increases rapidly when stellar mass goes below the observational completeness but converges at $\approx 10^3 - 10^4 M_\odot$. The discrepancy between the number of satellites below the observation limit is known to exist between observations and Λ cold dark matter numerical simulations, the "missing satellite problem" (Kauffmann et al., 1993; Moore et al., 1999; Klypin et al., 1999).

3. **Halo occupation fraction**

   In the middle panel of Figure 2.7 we plot individual halo occupation fractions (fraction of haloes at given $M_{\rm vir,peak}$ that hosts a galaxy at $z = 0$) from 30

Caterpillar trees and find only a small scatter among them. This fraction plummets at $M_{\rm vir,peak} \approx 10^8 - 10^{8.5} M_\odot$ and stays constant while the presence and value of the stellar mass plateau changes. Thus, the presence of a plateau due to stochastically populated haloes suggested by Sawala et al. (2015) is not the only reason for such a break.

4. **Stellar mass-to-halo mass relation**

   In Figure 2.7, A-SLOTH simulated galaxies are plotted with coloured points, where the colour indicates the data density in a 2-dimensional phase space. The cyan triangles are the MWs in the 30 *Caterpillar* trees. Our fiducial model gives excellent consistency with the SMHM relation in GK14 and the one in N20. An interesting result of our model is that we predict a flattening in the SMHM relation below $M_{\rm vir,peak} \approx 10^9 M_\odot$. Two main factors are responsible for this plateau. 1) The outflow efficiency $\gamma_{\rm out}$, which is proportional to the peak virial mass of a halo (Eq. 2.35). In our model, one SN event ejects more gas in smaller haloes than in larger ones. In other words, gas is more easily retained in larger haloes, leading to more star formation. 2) The star formation efficiency. In Figure 2.5, we observe that the turn occurs at different $M_{\rm vir,peak}$ for different $\eta_{\rm II}$ and the mass of the plateau increases when $\eta_{\rm II}$ increases. This is because the higher the star formation efficiency, the more stars form before the SNe feedback kicks in and regulate further star formation. We fit the SMHM relation from our fiducial model with a broken power-law

   $$M_* \propto M_{\rm vir,peak}^{1.80} \qquad \text{for} \quad M_{\rm vir,peak} \geq 10^9 M_\odot, \tag{2.43}$$

   and

   $$M_* \propto M_{\rm vir,peak}^{0.66} \qquad \text{for} \quad M_{\rm vir,peak} < 10^9 M_\odot. \tag{2.44}$$

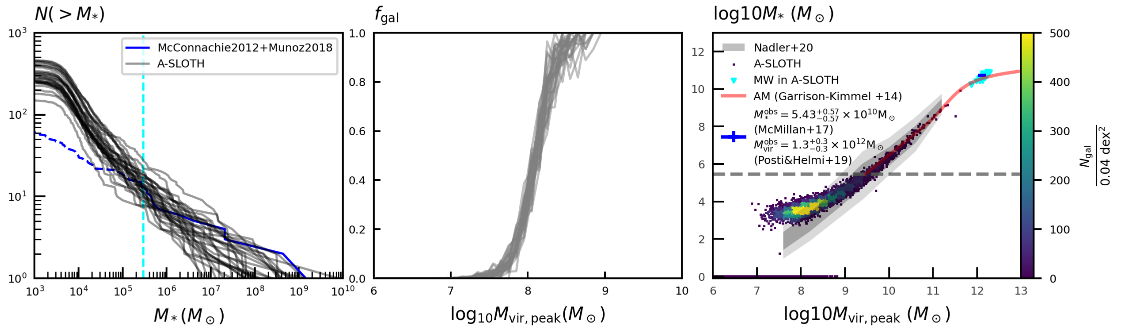

Figure 2.7: In the left panel, A-SLOTH simulated SMFs from 30 *Caterpillar* trees are shown in grey solid curves and the observed SMF (McConnachie, 2012; Muñoz et al., 2018) is plotted in blue, where the dashed curve indicates that the stellar mass is below the observational completeness (shown in the cyan dashed line). In the middle panel, the halo occupation fractions from A-SLOTH simulated galaxies are shown as grey solid curves. In the right panel, each data point represents one A-SLOTH simulated galaxy and its colour indicates the data density in the parameter space. The red solid curve represents the AM relation from GK14, which is robust at $M_* > 2.9\times10^5 M_\odot$. The grey contour shows the SMHM relation from N20, where the $1\,\sigma$ contour is shown in dark grey and the $2\,\sigma$ contour is shown in light grey. The grey dashed line indicates the observational completeness and below this M_*, we enter the prediction region of our model. We identify the simulated MWs with cyan triangles and the blue cross marks the observed values of MW with upper and lower limits. The MW stellar mass is estimated by McMillan (2017) and the MW virial halo mass is estimated by Posti and Helmi (2019). We show satellites with zero surviving stars at the bottom of the figure.

2.4.2 Slope of the Pop II initial mass function

Here we discuss how different Pop II IMFs change our main results. To simplify the problem, we only change the slope of the Pop II IMF $\alpha_{\rm II}$ in the mass range $M_{\rm star} \geq 0.5M_\odot$. Other than the fiducial value from the Kroupa IMF, $dN/d\log M \propto M^{-1.3}$, we examine two different slopes, which are $dN/d\log M \propto M^{-0.3}$ and $dN/d\log M \propto M^{-2.3}$, corresponding to a more top-heavy and bottom-heavy IMF, respectively. The resulting changes in the cumulative SMF, halo occupation fraction , and SMHM relation are shown in Figure 2.8. Green, orange, and blue represent $\alpha_{\rm II} = -0.3$, -1.3 and -2.3, respectively.

We find that flattening the Pop II IMF at $M_{\rm star} \geq 0.5M_\odot$ leads to lower stellar mass at $z = 0$ in all haloes. The cumulative SMF is therefore below the observed one at all M_*. In contrary, steepening the Pop II IMF at $M_{\rm star} \geq 0.5M_\odot$ makes the flattening of the cumulative SMF occur at higher M_*, compared to the fiducial model, and the SMF is entirely above the observed one. We find a universal turning point at $M_{\rm vir,peak} \approx 10^9 M_\odot$ and that flattening the Pop II IMF at $M_{\rm star} \geq 0.5M_\odot$

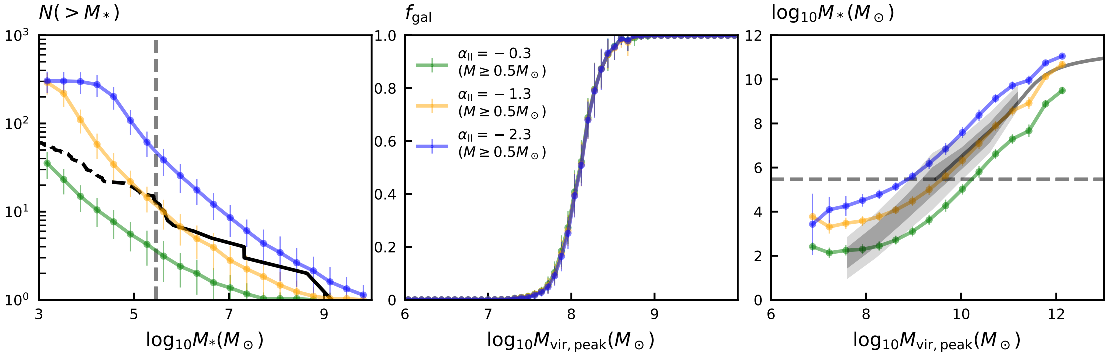

Figure 2.8: Similar to Figure 2.5, but we show the cumulative SMF, halo occupation fraction, and SMHM relation from different simulations where we adopt different slopes of Pop II IMF at the high mass end ($M_{\rm star} > 0.5M_\odot$).

leads to a flatter SMHM relation at $M_{\rm vir,peak} < 10^9M_\odot$, but does not change the slope of SMHM relation at $M_{\rm vir,peak} \geq 10^9M_\odot$ significantly.

Changing the Pop II IMF at the high mass end is equivalent to changing the fraction of massive stars at a fixed total stellar mass. Smaller haloes ($M_{\rm vir,peak} < 10^9M_\odot$) are less resistant to the stellar feedback, therefore, not only the slope of the SMHM depends more heavily on the slope of the Pop II IMF, but also the overall distribution of stellar masses of these haloes at $z = 0$ depends on the slope of the Pop II IMF, leading to different cumulative SMFs. The influence of different Pop II IMFs on the halo occupation fraction is negligible.

Since we only vary the slope of the Pop II IMF in these simulations, there is the possibility that we can tune the free parameters in our model to find another "good" model, which produces consistent results with the observation. However, it is not the main focus of this work to study how different Pop II IMFs influence the results. We therefore leave this exploration for future studies.

2.4.3 LW background and baryonic streaming velocity

As described in Section 2.2.2, the strength of the LW background (J_{21}) and baryonic streaming velocities ($v_{\rm BC}$, in units of root-mean-squared value $\sigma_{\rm rms}$) affect the critical mass $M_{\rm crit}$ of a halo. Here we compare different $M_{\rm crit}$ models with the fiducial one and examine the influence of $v_{\rm BC}$.

1. **S21**

   This is our fiducial model where we follow Eqs. 9 and 10 in Schauer et al. (2021) (see Section 2.2.2 for details). The critical mass of a halo is

   $$\log_{10} M_{\rm crit} = 6.0174\,(1.0 + 0.166\sqrt{J_{21}}) + 0.4159\frac{v_{\rm BC}}{\sigma_{\rm rms}}, \tag{2.45}$$

   where J_{21} depends on redshift via $J_{21} = 10^{2-z/5}$. We note that we adopt constant $v_{\rm BC}$ throughout the simulation.

2. **OHS**

   In our previous work, we compute $M_{\rm crit}$ by considering prescriptions in O'Shea and Norman (2008), Hummel et al. (2012), and Stacy et al. (2011). Thus, we denote this model as OHS. First, we follow O'Shea and Norman (2008) and assume that $M_{\rm crit}$ depends only on J_{21}. We denote this critical mass as $M_{\rm crit,O}$ that

   $$M_{\rm crit,O} = 4\left(1.25 \times 10^5 + 8.7 \times 10^5\,(4\pi J_{21})^{0.47}\right). \tag{2.46}$$

   Second, we follow Hummel et al. (2012) and assume that when a halo reaches the critical virial temperature, $T_{\rm crit} = 2200$ K, the gas reaches high density and collapses to form Pop III stars. We denote this critical mass as $M_{\rm crit,H}$ and compute its value

   $$M_{\rm crit,H} = 10^6\left(\frac{T_{\rm crit}}{1000{\rm K}}\right)^{1.5}\left(\frac{1+z}{10}\right)^{-1.5}. \tag{2.47}$$

   Finally, we follow Stacy et al. (2011) and assume that the gas in a halo collapses and starts to form stars when the virial mass of the halo reaches a critical value. We denote this mass as $M_{\rm crit,S}$ and

   $$M_{\rm crit,S} = \frac{\pi v_{\rm eff}^3}{6G^{3/2}\rho^{1/2}}, \tag{2.48}$$

   where $v_{\rm eff} = \sqrt{v_{\rm BC}(z)^2 + c_{\rm s}^2}$ is the effective velocity of the gas, the redshift-dependent streaming velocity is given by

   $$v_{\rm BC}(z) = v_{\rm BC} \times \frac{6 \times 10^5}{201} \times (1+z), \tag{2.49}$$

   where $v_{\rm BC}$ is the input streaming velocity at $z = 0$, $c_{\rm s} = \sqrt{k_{\rm B}T/\mu m_{\rm H}}$ is the sound speed, ρ is the mean dark matter density of the halo and $T =$

$0.017(1+z)^2$K is the gas temperature (Schneider, 2015). In model OHS, the final critical mass is determined by taking the maximum of $M_{\rm crit,O}$, $M_{\rm crit,H}$, and $M_{\rm crit,S}$ that

$$M_{\rm crit} = {\rm MAX}(M_{\rm crit,O}, M_{\rm crit,H}, M_{\rm crit,S}). \tag{2.50}$$

3. **F13**

The last $M_{\rm crit}$ model we consider is based on the prescription in Fialkov et al. (2013). In this model F13, the virial mass of a halo needs to exceed $M_{\rm crit}$ such that the gas cools down efficiently and starts to form stars. This critical mass is computed by

$$M_{\rm crit} = M_0(1 + 6.96(4\pi J_{21})^{0.47}), \tag{2.51}$$

where J_{21} depends on redshift via $J_{21} = 10^{2-z/5}$, and M_0 is the critical mass when there is no LW background. We show the derivation of M_0 below. Following Bryan and Norman (1998), the mean density of a halo can be written as

$$\overline{\rho}_{\rm h} = \frac{3M_{\rm vir}}{4\pi r_{\rm vir}^3} = \Delta_{\rm vir}\rho_m(z) = \Delta_{\rm vir}\Omega_{\rm m}(z)\frac{3H^2(z)}{8\pi G}, \tag{2.52}$$

where $M_{\rm vir}$ is the virial mass of the halo, $\Delta_{\rm vir} = \overline{\rho}_{\rm h}/\rho_m(z)$ is the over density, $\Omega_{\rm m}(z)$ is the redshift dependent matter density, $H(z)$ is the Hubble constant, and G is the gravitational constant. We have the following equations:

$$\rho_{\rm m}(z) = \Omega_{\rm m}(z)\rho_{\rm c}(z) = \rho_{\rm m,0}(1+z)^3 = \Omega_{\rm m,0}\frac{3H_0^2}{8\pi G}(1+z)^3, \tag{2.53}$$

and

$$r_{\rm vir}^3 = h^{-2}M_{\rm vir}\Delta_{\rm vir}^{-1}\Omega_{\rm m,0}^{-1}(1+z)^{-3}\frac{3}{4\pi}\frac{8\pi G}{3H_0^2}, \tag{2.54}$$

where $H_0 = 67.8$ kms^{-1} Mpc^{-1} (Planck Collaboration et al., 2016). We can rewrite Eq. 2.54 into

$$\begin{aligned} r_{\rm vir} \simeq & 210h^{-1}{\rm kpc}\left(\frac{\rm M_{vir}}{10^{12}{\rm h^{-1}M_\odot}}\right)^{1/3} \\ & \times \left(\frac{\Delta_{\rm vir}}{200}\right)^{-1/3}\Omega_{\rm m,0}^{-1/3}(1+z)^{-1} \end{aligned} \tag{2.55}$$

Therefore, the circular velocity at virial radius is

$$\begin{aligned} v_{\rm cir} = \sqrt{\frac{GM_{\rm vir}}{r_{\rm vir}}} \simeq 146.6{\rm kms^{-1}} \\ \left(\frac{M_{\rm vir}}{10^{12}{\rm h^{-1}1M_\odot}}\right)^{1/3} \left(\frac{\Delta_{\rm vir}}{200}\right)^{1/6} \Omega_{\rm m,0}^{1/6}(1+z)^{1/2} \end{aligned} \tag{2.56}$$

Finally, we have $M_{\rm vir}$ as a function of $v_{\rm cir}$, over density $\Delta_{\rm vir}$, and redshift z,

$$\begin{aligned} \frac{M_{\rm vir}}{10^{12}{\rm h^{-1}M_\odot}} = \\ \left(\frac{v_{\rm cir}}{146.6{\rm kms^{-1}}}\right)^{3} \left(\frac{\Delta_{\rm vir}}{200}\right)^{-1/2} \Omega_{\rm m,0}^{-1/2}(1+z)^{-3/2}. \end{aligned} \tag{2.57}$$

In Fialkov et al. (2012), they assumed that a halo starts to form Pop III stars if its circular velocity exceeds the threshold,

$$v_{\rm cool}(z) = \sqrt{(3.714)^2 + (4.015 v_{\rm BC}(z))^2}, \tag{2.58}$$

where the streaming velocity is dependent on redshift $v_{\rm BC}(z) = 0.0298(1+z)v_{\rm BC}$ and $v_{\rm BC}$ is the initial streaming velocity. Here we assume that $M_{\rm vir}$ is at $\Delta_{\rm vir} = 200$ and substitute $M_{\rm vir} = M_0$ and $v_{\rm cir} = v_{\rm cool}$ in Eq. 2.57 to compute M_0 in Eq. 2.51.

Finally, as described in Section 2.2.2, we take the minimum of $M_{\rm crit}, i$ and $M_{\rm crit,10^4K}$ to be the final critical mass $M_{\rm crit,fin}$ in model i. In total we have 3 different $M_{\rm crit}$ approaches: S21, OHS, and F13. We compare the results between them while varying the initial value of streaming velocity, $v_{\rm BC} = [0, 0.8, 2, 3]\sigma_{\rm rms}$. Other parameters are fixed at the fiducial values ($\eta_{\rm II} = 2, \alpha_{\rm out} = 0.72, M_{\rm norm} = 10^{10.5}M_\odot$). Kulkarni et al. (2021) also propose a new fitting formula for the critical mass. Due to the recency of their results, we were not able to include their proposed critical mass in our comparison.

We perform the same analysis as in Section 2.3. Despite the difference in the $M_{\rm crit}$ models, the influence of LW background and streaming velocity is negligible on the mean MW stellar mass as well as the satellite-based χ^2 and p-values. This indicates that we cannot tell the three $M_{\rm crit}$ models apart with the observables used in Section 2.3. We show the cumulative SMF, halo occupation fraction, and SMHM reltaion in Figure 2.9. The largest impact of LW background and streaming velocity is on smaller haloes, which is shown by the cumulative SMF and the halo occupation fraction. Model OHS produces a factor of few more ultra-faint dwarf galaxies than

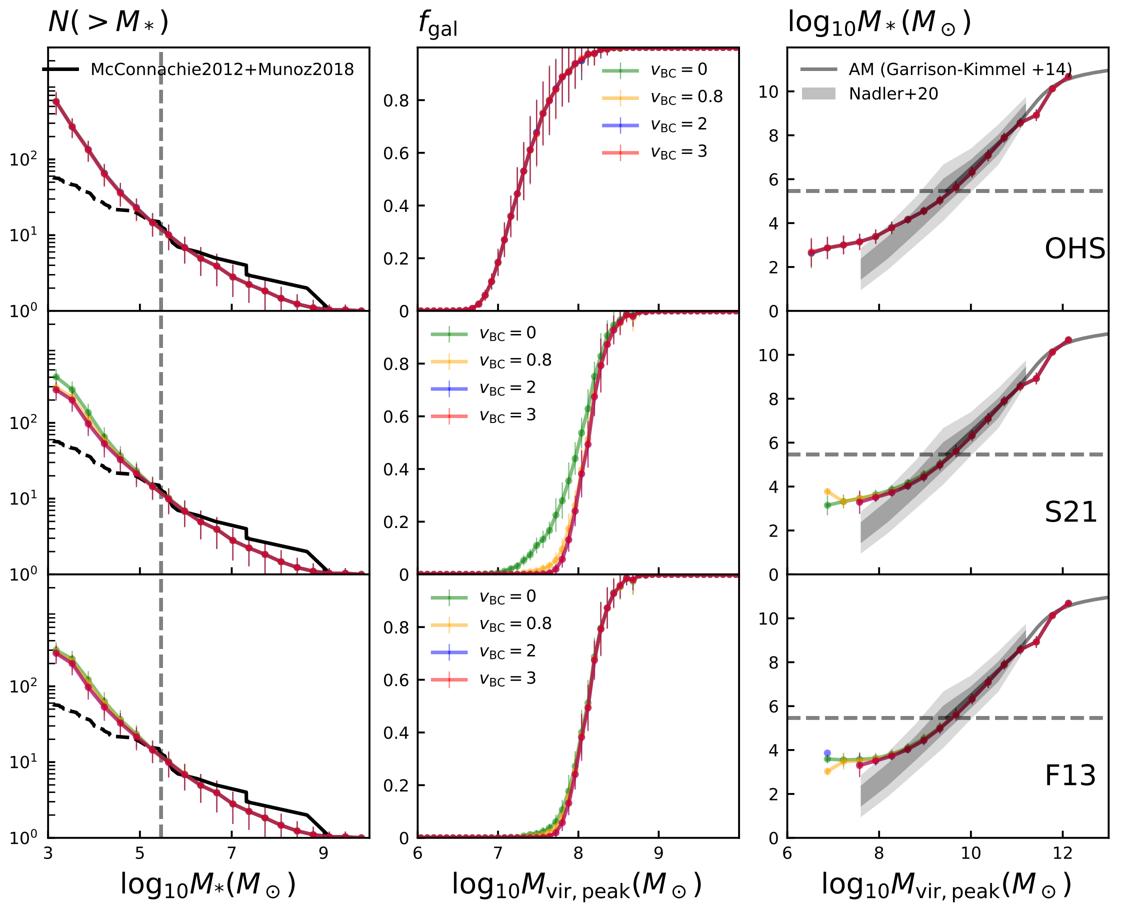

Figure 2.9: Similar to Figure 2.5. Here we show the cumulative SMF, halo occupation fraction, and SMHM relation from simulations where we adopt different $M_{\rm crit}$ models and different $v_{\rm BC}$. From top to bottom: OHS, S21, and F13.

the other two models, regardless of the value of $v_{\rm BC}$. In model S21 we find that the number of ultra-faint dwarf galaxies $N_{\rm UFD}$ decreases as $v_{\rm BC}$ increases but saturates at $v_{\rm BC} = 2\sigma_{\rm rms}$. There is a similar dependence of $N_{\rm UFD}$ on $v_{\rm BC}$ in model F13 and it produces the fewest ultra-faint dwarf galaxies among the four models when $v_{\rm BC} = 0$. In Figure 2.10, we show $M_{\rm crit}$ v.s. z for different $M_{\rm crit}$ models with different values of $v_{\rm BC}$. In our fiducial model ($v_{\rm BC} = 0.8\sigma_{\rm rms}$, F13 gives the highest $M_{\rm crit}$ at $z = 10-15$, followed S21, and finally OHS. This is consistent with the difference we find in $N_{\rm UFD}$. The fraction of haloes hosting a galaxy decreases slower as $M_{\rm vir,peak}$ decreases in model OHS, whereas in models S21 and F13, this fractions experiences a plummet at $M_{\rm vir,peak} \approx 10^8 M_\odot$.

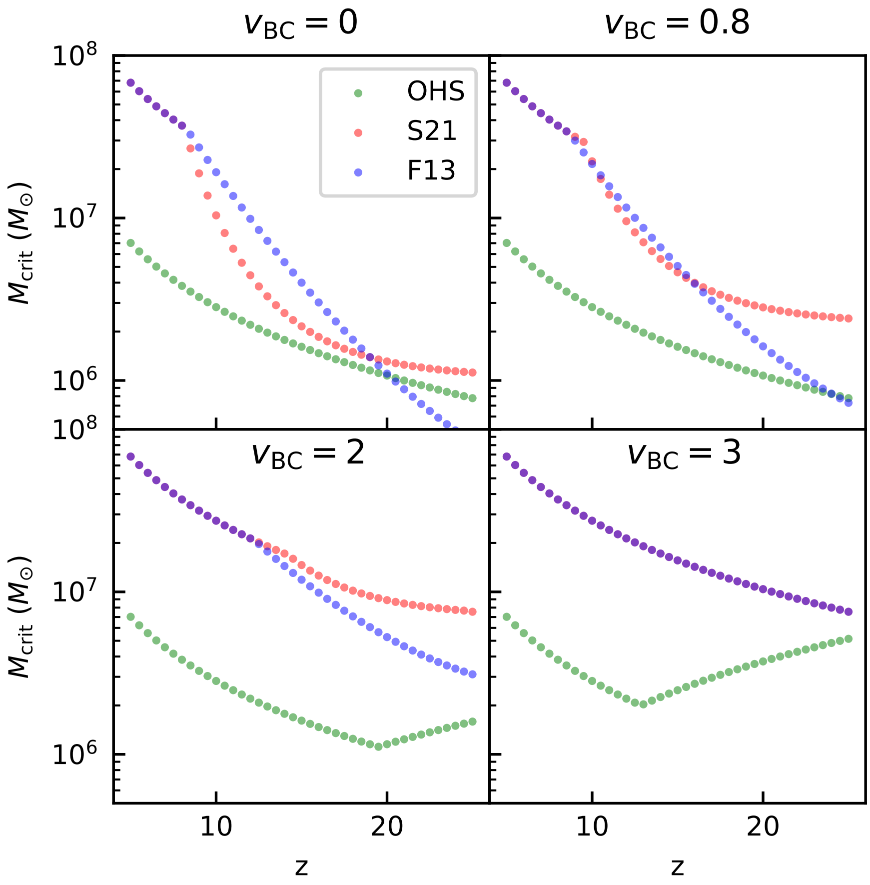

Figure 2.10: $M_{\rm crit}$ v.s. redshift from different $M_{\rm crit}$ models and different $v_{\rm BC}$.

2.5 Discussion

2.5.1 A low-mass plateau in the stellar mass-to-halo mass relation.

The right column of Figure 2.5 shows our prediction that the SMHM does not continue as a single power-law to low masses, but instead reaches a plateau of roughly constant stellar mass. In A-SLOTH, this plateau is primarily due to a minimum mass scale imposed by supernova feedback: low-mass haloes able to self-quench once they form a certain amount of stars. Figure 2.11 shows this in detail: we run simulations with different Pop II star formation efficiencies using only 1 *Caterpillar* tree. We compute the stellar mass form before SNe occur in each global time-step (Δt_z) $M_{*,\mathrm{pre\ SNe}}$ and the cumulative survival stellar mass $M_*(>z)$ for all haloes at various redshifts. At given survival stellar mass, we plot the mean $M_{*,\mathrm{pre\ SNe}}$ with $1\,\sigma$ among the haloes. We observe that with higher Pop II star formation efficiency, haloes are able to form more stars before SNe occur, which is expected. Once massive stars start to die as SNe, $M_{*,\mathrm{pre\ SNe}}$ quickly drops. Thus, if star formation is more efficient, more stars will form before SN feedback halts star formation. We emphasise that this plateau is *not* set by reionisation in A-SLOTH. In this way, it may support the supernova quenching scenario proposed by earlier theoretical studies and cosmological simulations that the external ionising background is not the dominant source to halt star formation in mini-haloes (Ricotti and Gnedin, 2005; Salvadori and Ferrara, 2009; Bland-Hawthorn et al., 2015; Jeon et al., 2015, 2017). Recent observational studies also stress the importance of SN feedback based on the star formation histories of dwarf galaxies (Monelli et al., 2010b,a; Hidalgo et al., 2011, 2013; Gallart et al., 2021).

A similar flattening in the SMHM relation has been observed in several previous studies, but primarily driven by reionisation. Sawala et al. (2015) found such a flattening of the SMHM relation in hydrodynamic simulations, though at much higher stellar masses ($\approx 10^5 M_\odot$). In their simulations, this effect was primarily driven by a low occupation fraction of galaxies in haloes, due to strong global reionisation at $z = 11$, as well as tidal stripping. This motivated Dooley et al. (2017) and Jethwa et al. (2018) to consider a "bent" SMHM relation, which is not required to explain the MW satellite luminosity function but may alleviate tensions with the SMHM relation around the LMC (also see Manwadkar and Kravtsov 2021). A similar plateau is also seen at lower stellar masses ($\approx 10^3 M_\odot$) by Wheeler et al. (2015, 2019), though they emphasise this plateau could be due to resolution effects as the galaxies are

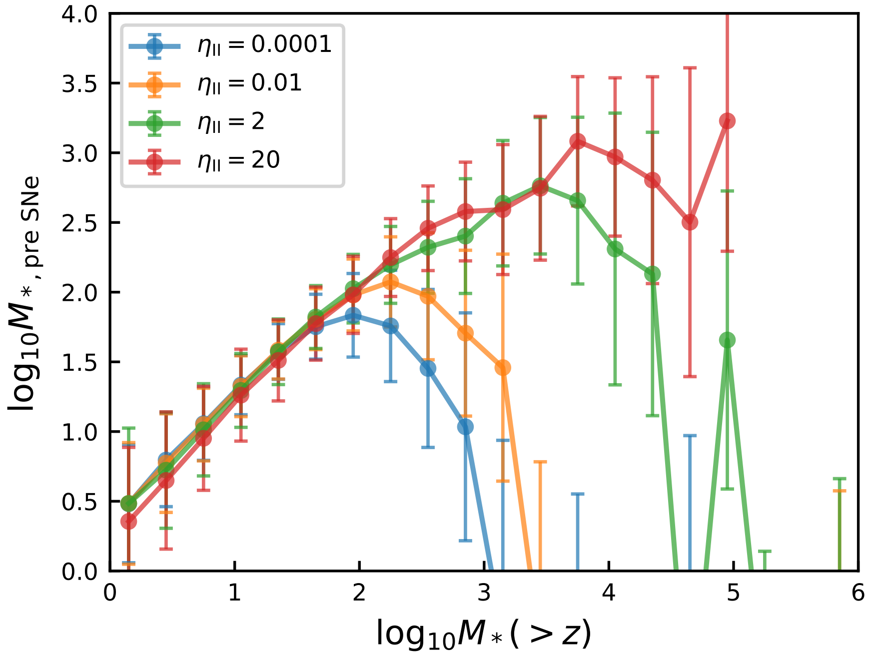

Figure 2.11: $M_{*,\text{pre SNe}}$ v.s. $M_*(>z)$ in haloes across all redsfhits from 1 *Caterpillar* tree. Results from different simulations with different η_{II} are plotted with different colours along with the standard deviation. Note that $M_{*,\text{pre SNe}}$ is computed at each redshift but $M_*(>z)$ is cumulative over redshifts.

composed of ≈10 − 100 star particles only. More recently, Applebaum et al. (2021) found such a flattening as well, but also occurring at the ≈10 star particle threshold. Other analytic models have also seen a low-mass plateau in the SMHM relation, e.g. Kravtsov and Manwadkar (2022) predict a break in the SMHM relation due to reionisation and scatter in halo mass growth histories. These previous results predict similar breaks in the SMHM as A-SLOTH, but for a fundamentally different reason: reionisation instead of supernova feedback. Note that A-SLOTH does include local reionisation through small-scale inhomogeneities, but not yet large-scale instantaneous reionisation quenching at a parameterised redshift like most of these previous models.

The presence of a stellar mass plateau has several important implications. First, we predict that the luminosity function of UFDs should experience a sharp upturn at $\approx 10^4 M_\odot$. Dooley et al. (2017) showed that such an upturn would match the luminosity function of LMC satellites, and indeed our predicted SMHM relation matches their required SMHM relation quite closely. Second, this has implications for the minimum known dark matter halo mass. If abundance matching holds, then the lowest stellar mass UFDs should reside in the lowest mass dark matter haloes, which puts constraints on the nature of dark matter (e.g., Jethwa et al., 2018;

Nadler et al., 2021; Kim and Peter, 2021). Such constraints often assume a single power-law can describe the SMHM relation at the low mass regime, but this would not be sufficient to describe the SMHM relation we predict here with A-SLOTH. By introducing a break in the SMHM relation, it changes the constraints obtained on dark matter properties. Finally, we note that A-SLOTH does not predict a very large scatter *around* the low-mass end of the SMHM relation, as suggested by several previous works (e.g., Garrison-Kimmel et al., 2017; Munshi et al., 2021). This scatter is mainly due to star formation in some haloes being suppressed by reionisation. When such large scatter is introduced, it actually *steepens* the intrinsic SMHM, opposite to our prediction of a minimum stellar mass scale from SN feedback.

2.5.2 Uncertainty in critical masses of haloes

Previous studies that did not take the large-scale streaming into account (Dijkstra et al., 2004; Susa et al., 2014; Visbal et al., 2014; Hirano et al., 2015; Skinner and Wise, 2020) found that the critical mass of haloes to form stars at high redshift are typically in the range of $10^5 - 10^6 M_\odot$. In addition, Park et al. (2021) suggested haloes that do not form stars until $\sim 10^7 M_\odot$ when the LW radiation field is strong enough. Studies that include large-scale streaming generally find suppression of star formation in haloes, but the minimum mass of haloes to host stars is still uncertain. Greif et al. (2011) found the mass of star forming mini-haloes increased from $[2-3] \times 10^5 M_\odot$ to $\sim 10^6 M_\odot$. Tseliakhovich et al. (2011) showed that the average mass of gas-rich haloes increased from $2 \times 10^4 M_\odot$ to $2 \times 10^5 M_\odot$ and the suppression of star formation by a factor of 1.4. Naoz et al. (2013) concluded that the mass of haloes that are able to retain enough gas (baryonic fraction ~ 0.1) increased from $\sim 10^5 M_\odot$ to $\sim 10^6 M_\odot$. Hirano et al. (2017) simulated supermassive black hole formation at high redshift and found that the virial mass of star forming haloes increased by 2 orders of magnitude at $z > 30$ in their most extreme case. More recently, Schauer et al. (2019) argued that with $v_{\rm BC} = 3\,\sigma_{\rm rms}$, star formation can be fully suppressed for haloes below the atomic cooling limit. Kulkarni et al. (2021) analyse a large sample of haloes from hydrodynamical simulations and find that the LW background and baryonic streaming can change the critical haloes mass for Pop III star formation by over one order of magnitude at any given redshift. These studies show the importance of the relative large-scale streaming between baryon and dark matter on the star-formation process in the early Universe. There is no fully conclusive evidence on the most likely environment that MW resides in. However, we note that regions with streaming velocities of $v_{\rm BC} = 0.8\,\sigma$ are most likely (Schauer et al., 2021), and so we adopt this in our fiducial model.

2.5.3 Caveats

The mechanical and chemical feedback of Type Ia SNe is neglected in our current model. In the lowest-mass galaxies, Type Ia SNe can be safely ignored because they only occur with a large delay after star formation and a couple of CCSNe is enough to quench or even suppress further star formation. In the MW, Type Ia SNe (Ruiter et al., 2009) are about a factor of 5 fewer than CCSNe (Li et al., 2011; Rozwadowska et al., 2021). Thus, we do not expect the mechanical feedback from Type Ia SNe to affect our simulations substantially. We note the importance of including Type Ia SNe to correctly model the chemical abundances in the MW system, which we plan to improve in future studies.

We do not include an external ionisation background in this model. The main source of ionisation in our model is the emission of the MW. This choice is made for two reasons: First, if the modelled volume was cosmologically representative, we would find a Thomson scattering optical depth of $\tau_e \approx 0.140$ from our model. We point out that we explicitly do not try to reproduce the value from the Planck observations ($\tau_e = 0.066$ Planck Collaboration et al., 2016). The fact that our optical depth is higher than the average value inferred from Planck indicates that our modelled volume experiences earlier reionisation than the Universe at large and that it is dominated by local sources. Second, except for very strong ionising radiation fields, the LW feedback completely prevents star formation in haloes below the atomic cooling limit at redshifts below $z \approx 14$. Therefore reionisation feedback is only a small effect in our model.

We adopt a uniform LW background at the same redshift and ignore contributions from nearby sources. Earlier hydrodynamical simulations (Ahn et al., 2009; Johnson et al., 2013) indicate that variations of the local LW intensity can span several orders of magnitudes. Exposure to a much higher LW radiation can further suppress star formation in mini-haloes. However, this is only important for a small fraction of haloes because they need to be in close proximity to massive star-forming galaxies. Such spatial variation in LW radiation were considered in several semi-analytic models (Agarwal et al., 2012; Chon et al., 2016; Visbal et al., 2020) to study the formation of direct collapse black holes and Pop III star formation rate at high redshift. In this work, Pop III star formation has a minor effect on the results (number counts of MW satellites and the SMHM relation), but we plan to adopt a more detailed LW radiation model in A-SLOTH in future studies.

2.6 Summary

We introduce an improved Pop II SF model in the semi-analytic code A-SLOTH, which takes dark matter merger trees as input and calculates the baryonic contents in the haloes throughout its merger history. The important physical processes include Pop III and Pop II SF, aw well as mechanical and chemical feedback from massive stars. The new feature in the Pop II SF model is that we are now able to trace individual Pop II stars, which allows us to precisely resolve stellar feedback in space and time. We take 30 merger trees from the *Caterpillar* project (Griffen et al., 2016) and use A-SLOTH to study the SMHM relation at $z = 0$ of satellites in MW-like systems.

In this work, we focus on the Pop II SF model. The main free parameters are the star formation efficiency $\eta_{\rm II}$, normalisation mass $M_{\rm norm}$ and exponent $\alpha_{\rm out}$ in the outflow efficiency $\gamma_{\rm out}$. We calibrate our model with the observed stellar mass (McMillan, 2017) and cold gas mass of MW (Ferrière, 2001), the SMHM relation derived with AM technique from GK14 and N20 above the observational completeness, and the observed cumulative stellar mass function of satellite galaxies McConnachie (2012); Muñoz et al. (2018). We find $\eta_{\rm II} = 2$, $M_{\rm norm} = 10^{10.5} M_\odot$, and $\alpha_{\rm out} = 0.72$ gives the most consistent results with the observation and adopt these as fiducial values.

Our fiducial model produces a mean MW stellar mass of $4.84 \times 10^{10} M_\odot$ and mean cold gas mass of $5 \times 10^9 M_\odot$, which are consistent with the observed values of $[4.86 - 6] \times 10^{10} M_\odot$ and $[3.1 - 6] \times 10^9 M_\odot$, respectively. The cumulative stellar mass function of MW satellite galaxies from A-SLOTH simulation is consistent with the observation above the observational completeness. We also find that the cumulative SMF has an upturn when M_* is below observational completeness and the difference between merger trees decreases. Below $M_* \approx 10^3 - 10^4 M_\odot$ the cumulative SMF flattens. The fraction of haloes that host a galaxy (halo occupation fraction) increases rapidly above $M_{\rm vir,peak} \approx 10^8 M_\odot$, and it is insensitive to the free parameters in our Pop II SF model. Our fiducial SMHM relation is consistent with the ones in GK14 and N20. We find that the slope of the SMHM relation for stellar masses is determined by the exponent $\alpha_{\rm out}$ and normalisation mass $M_{\rm norm}$ in the outflow efficiency. We also observe a plateau in the SMHM relation at $M_{\rm vir,peak} \leq 10^9 M_\odot$. This plateau represents a minimum stellar mass that forms before SNe occur and quench further star formation, which is mainly determined by the Pop II star formation efficiency $\eta_{\rm II}$.

We further examine how $\alpha_{\rm II}$, the slope of Pop II IMF at the high mass end

($M_{\rm star} > 0.5 M_\odot$), influences the results. For a top-heavy IMF, with $\alpha_{\rm II}$ below the Kroupa (2001) value, the fraction of SNe at given stellar mass is lower, leading to weaker feedback. On the contrary, for a more bottom-heavy IMF, the fraction of SNe at given stellar mass is higher and the resulting stellar feedback is stronger. Therefore, galaxies have higher stellar mass in simulations with steeper $\alpha_{\rm II}$ than in those with shallower $\alpha_{\rm II}$. Finally, we examine the impact of different $M_{\rm crit}$ models and of the streaming velocity. We compare three different $M_{\rm crit}$ approaches: 1) the default model from Eqs. 9 and 10 in Schauer et al. (2021), which we denote as S21, 2) a combination of $M_{\rm crit}$ formulae from O'Shea and Norman (2008), Hummel et al. (2012), and Stacy et al. (2011), which we denote as OHS, and 3) $M_{\rm crit}$ formula from Fialkov et al. (2013), which we denote as F13. We find that model OHS produces a factor of few more ultra-faint dwarf galaxies and the effect of streaming velocity is negligible. Models S21 and F13 show similar dependence on streaming velocity that $N_{\rm UFD}$ decreases as $v_{\rm BC}$ increases and stays constant after $v_{\rm BC} = 2\sigma_{\rm rms}$. In model OHS, the halo occupation fraction experiences a slower decrease as $M_{\rm vir,peak}$ decreases, whereas in models S21 and F13, the halo occupation fraction expreiences a plummet at $M_{\rm vir,peak} \approx 10^8 M_\odot$.

The newly implemented Pop II SF model in A-SLOTH provides us an efficient and reliable framework to follow the formation of individual stars and their corresponding feedback at appropriate timings. This new model also enables us to examine the properties of surviving stars individually. We plan to perform follow-up studies on the properties of metal-poor stars in MW dwarf satellite galaxies at $z = 0$.

3

Analyse the simulated data with unsupervised clustering algorithms

This chapter is based on a paper that has been submitted to MNRAS. I am the first author and conduct the simulation and the analysis. The proposed method is primarily developed together with Tilman Hartwig. The text is majorly written by me and the listed coauthors provide physical insights and suggestions.

Abstract

We develop a new analysis method that allows us to compare multi-dimensional observables to a theoretical model. The method is based on unsupervised clustering algorithms which assign the observational and simulated data to clusters in high dimensionality. From the clustering result, a goodness of fit (the p-value) is determined with the Fisher-Freeman-Halton test. We first show that this approach is robust for 2D Gaussian distributions. We then apply the method to the observed MW satellites and simulated satellites from the fiducial model of our semi-analytic code A-SLOTH. We use the following 5 observables of the galaxies in the analysis: stellar mass, virial mass, heliocentric distance, mean stellar metallicity [Fe/H], and stellar metallicity dispersion $\sigma_{[\mathrm{Fe/H}]}$. A low p-value returned from the analysis tells us that our A-SLOTH fiducial model does not reproduce the mean stellar metallicity of the observed MW satellites well. We implement an ad-hoc improvement to the physical model and show that the p-value improves by a factor of 2. This method can be extended to data with higher dimensionality easily. We plan to further improve the physical model in A-SLOTH using this method to study elemental abundances of stars in the observed MW satellites.

3.1 Motivation

Dwarf galaxies formed most of their stars at high redshift and are therefore important to understanding star formation in the early universe. Due to the shallow gravitational potential of their host haloes, the star formation in dwarf galaxies is thought to have stopped during the epoch of reionisation ($z > 6$; see Brown et al., 2014; Weisz et al., 2015). In other words, stars that we observe in the dwarf galaxies today are most likely old (formed > 12 Gyr ago). Many studies of dwarf galaxies focus on the ones in the MW system or in the Local Group (Belokurov et al., 2010; Drlica-Wagner et al., 2015; Koposov et al., 2015; Ji et al., 2021). Different properties of the dwarf galaxies are reported: from the observed populations (Koposov et al., 2009; Muñoz et al., 2018), the magnitudes, the heliocentric distances, the sizes, and the stellar velocity dispersions (McConnachie, 2012; Simon, 2019; Wang et al., 2021, and the references therein), to stellar dynamics (Kirby et al., 2017; McConnachie and Venn, 2020; Battaglia et al., 2022; Battaglia and Nipoti, 2022), detailed chemical information (Ji et al., 2016; Reichert et al., 2020; Yoon et al., 2020; Chiti et al., 2018, 2022), and the star formation history (Weisz et al., 2014; Gallart et al., 2021).

From a theoretical perspective, numerical simulations and semi-analytic modelling of the formation and evolution of dwarf galaxies have been carried out in the past decades (Ricotti and Gnedin, 2005; Font et al., 2011; Jeon et al., 2017; Sanati et al., 2022). Among numerous works, various observables or physical quantities are used to calibrate the models. For example, Starkenburg et al. (2013) reproduced the luminosity function and spatial distributions of the MW satellites. Salvadori et al. (2015) successfully reproduced the metallicity distribution functions and star formation histories of the dwarf galaxies with their semi-analytic model. Wheeler et al. (2019) matched their simulated dwarf galaxies with the observed stellar mass-to-halo mass relation and the 2D half-stellar-mass radii. Other works aim to study individual dwarf galaxies with higher numerical resolution. For instance, Safarzadeh and Scannapieco (2017) studied the r-process enrichment in ultra-faint dwarf galaxies and found one of their simulated haloes being similar to Reticulum II. Romano et al. (2019) simulated an isolated dwarf galaxy to understand the importance of stellar feedback in the formation of Boötes I.

The amount of data coming from either observations or simulations increases drastically as observational and computational technology continues to improve. To maximise the information gain from this data, machine learning has been proved to be a powerful tool in many astronomical fields. To give a few examples, Garcia-Dias et al. (2018) used K-Means unsupervised clustering to classify over 150,000 spectra. Reis et al. (2019) developed a data visualisation portal to help researchers spot anomalies in high dimensional astronomical data and dimensionality reduction. Logan and Fotopoulou (2020) used Hierarchical Density-Based Spatial Clustering of Applications with Noise to distinguish stars, galaxies and quasars. Ksoll et al. (2021a,b) used the algorithm RANSAC to determine the reddening properties of massive stars in giant molecular clouds and built a catalog for > 450,000 stars. Kang et al. (2022) used conditional invertible neural network to study properties of young massive stars with emission lines. Wang et al. (2022) utilised a convolutional neural network to recover the cosmic microwave background signal.

In this work, we introduce a different analysis method to help us analyse the results produced by our semi-analytic code A-SLOTH (Hartwig et al., 2022; Magg et al., 2022). A-SLOTH has been used to make predictions of Population III survivors in the MW, (Hartwig et al., 2015), Population III supernovae rate (Magg et al., 2016), to study the inhomogeneous mixing (Tarumi et al., 2020), and the properties of the MW satellites (Chen et al., 2022). With the help of unsupervised clustering algorithms, we do not compare individual properties of the observed and simulated galaxies separately as it is done in most of the earlier works, but consider multiple physical quantities altogether.

3.2 Method

We aim to compare our simulated data with observables in high-dimensional data space. One value should determine whether the simulated data and the observational data come from the same underlying distribution. In 1D, a renowned test to compare two data distributions is the Kolmogorov–Smirnov test Kolmogorov (1933, K-S) test. It computes the maximal Euclidean distances between the two distributions and return a p-value, which helps us reject the null hypothesis. Generalisation of the K-S test to 2D data is shown in the 1980s (Peacock, 1983; Fasano and Franceschini, 1987). In the following sections, we first describe the observed galaxies and the simulated galaxies used in the analysis. We then describe how we determine whether the physical model in A-SLOTH is successful at reproducing the observed properties of the MW satellites.

3.2.1 Observational data

Among the properties of the MW satellites, we are most interested in the stellar mass (M_*), virial mass ($M_{\rm vir}$), distance to the Sun ($D_\odot$), the mean stellar metallicity

([Fe/H]) and the stellar metallicity dispersion ($\sigma_{\rm [Fe/H]}$). We collect the following values of the observed MW satellites from Simon (2019) and the references therein: the V-band absolute magnitude $M_{\rm V}$, distance to the Sun $D_\odot$, the stellar velocity dispersion σ_*, and the half light radius $R_{\rm half}$. We compute $\langle$[Fe/H]$\rangle$ and $\sigma_{\rm [Fe/H]}$ from individual detections in the SAGA database[1] (Suda et al., 2008, 2017), except for Horologium I, Tucana III, Grus I, and Pisces II. These four galaxies have ≤ 3 detections available in the SAGA database. Therefore, we obtain $\langle$[Fe/H]$\rangle$ and $\sigma_{\rm [Fe/H]}$ for these galaxies again from Simon (2019). For Reticulum II, we add 5 newly detected stars reported by Chiti et al. (2022) and compute the mean [Fe/H] and the standard deviation along with the data from the SAGA database. To obtain the stellar mass of the observed satellites from $M_{\rm V}$, we simply assume a stellar mass-to-light ratio of 1 (McConnachie, 2012).

It is observationally challenging to estimate the virial masses of dark matter haloes in which the observed galaxies reside, because we cannot observe dark matter directly. On top of that, there is also no clear boundary of the dark matter halo. Some researchers utilise the observed stellar velocity dispersion and model the dark matter haloes of observed MW satellites (Muñoz et al., 2006; Walker et al., 2007; Chiti et al., 2021b). Errani et al. (2018) provided an estimate of mass enclosed in $1.8R_{\rm half}$ for dwarf spheroidal galaxies

$$M(< 1.8R_{\rm half}) = 3.5 \times 1.8R_{\rm half}\sigma_*^2{\rm G}^{-1}, \tag{3.1}$$

where G is gravitational constant and $R_{\rm half}$ is the half-light radius. We adopt virial masses of the observed MW satellites if they are provided in the literature, otherwise we simply take $M_{\rm vir} = 10M(< 1.8R_{\rm half})$. This factor of 10 is relatively arbitrary. From the 8 galaxies that have literature values, the difference between $M_{\rm vir}$ and $M(< 1.8R_{\rm half})$ is on the order of 10. Therefore we adopt 10 as the fiducial value but this is to be improved with more precise computation of the virial mass for each observed MW satellite. The physical quantities of observed MW satellites are listed in Table 3.1.

---

[1] http://sagadatabase.jp/

(1) Galaxy	(2) M_* $\log_{10} M_\odot$	(3) $D_\odot$ kpc	(4) σ_* km s^{-1}	(5) $\langle[\mathrm{Fe/H}]\rangle$	(6) $\sigma_{[\mathrm{Fe/H}]}$	(7) R_{half} pc	(8) $M_{\mathrm{halo}}(< 1.8 R_{\mathrm{half}})$ $\log_{10} M_\odot$	(9) M_{vir} $\log_{10} M_\odot$	(10) References
Bootes I	4.33	66.9	4.6	-2.60	0.42	191	6.77	7.00	1,1,1,2,2,1,,5
Bootes II	3.10	42.0	10.5	-2.34	0.65	42	6.83	7.83	1,1,1,2,2,1,,
Canes Venatic I	5.41	211.0	7.6	-1.91	0.54	211	7.25	8.25	1,1,1,2,2,1,,
Canes Venatic II	4.00	160.0	4.6	-2.21	0.60	162	6.70	7.70	1,1,1,2,2,1,,
Carina	5.70	106.0	6.6	-1.46	0.55	311	7.30	8.30	1,1,1,2,2,1,,4
Coma Berenices	3.63	42.0	4.6	-2.72	0.36	69	6.33	7.33	1,1,1,2,2,1,,
Draco	5.47	82.0	9.1	-1.97	0.46	231	7.44	9.60	1,1,1,2,2,1,,4
Fornax	7.26	139.0	11.7	-1.10	0.49	792	8.20	9.00	1,1,1,2,2,1,,4
Grus I	3.31	120.0	2.9	-1.42	0.41	28	5.53	6.53	1,1,1,1,1,1,,
Hercules	4.25	132.0	5.1	-2.43	0.40	216	6.92	7.92	1,1,1,2,2,1,,
Horologium I	3.42	87.0	4.9	-2.76	0.17	40	6.15	7.15	1,1,1,1,1,1,,
Leo I	6.63	254.0	9.2	-1.32	0.34	270	7.52	9.00	1,1,1,2,2,1,,4
Leo II	5.82	233.0	7.4	-1.56	0.40	171	7.14	8.60	1,1,1,2,2,1,,4
Leo IV	3.92	154.0	3.3	-2.47	0.50	114	6.26	7.26	1,1,1,2,2,1,,

(1) Galaxy	(2) M_* $\log_{10} M_\odot$	(3) $D_\odot$ kpc	(4) σ_* km s^{-1}	(5) $\langle[\mathrm{Fe/H}]\rangle$	(6) $\sigma_{[\mathrm{Fe/H}]}$	(7) R_{half} pc	(8) $M_{\mathrm{halo}}(< 1.8 R_{\mathrm{half}})$ $\log_{10} M_\odot$	(9) M_{vir} $\log_{10} M_\odot$	(10) References
Pisces II	3.61	183.0	5.4	-2.45	0.48	60	6.41	7.41	1,1,1,1,1,1,,
Reticulum II	3.51	31.6	3.3	-2.88	0.52	51	5.91	6.91	1,1,1,2+3,2+3,1,,
Sagittarius	7.32	26.7	9.6	-0.54	0.31	2662	8.56	9.56	1,1,1,2,2,1,,
Sculptor	6.25	86.0	9.2	-1.86	0.61	279	7.54	9.00	1,1,1,2,2,1,,4
Segue 1	2.44	23.0	3.7	-2.52	0.88	24	5.68	6.68	1,1,1,2,2,1,,
Segue 2	2.71	37.0	2.2	-2.24	0.40	40	5.45	6.45	1,1,1,2,2,1,,
Sextans	5.50	95.0	7.9	-2.12	0.54	456	7.62	8.48	1,1,1,2,2,1,,4
Triangulum II	2.56	28.4	3.4	-2.43	0.49	16	5.43	6.43	1,1,1,2,2,1,,
Tucana II	3.48	58.0	8.6	-2.94	0.29	121	7.12	8.12	1,1,1,2,2,1,,
Tucana III	2.52	25.0	1.2	-2.42	0.19	37	4.89	5.89	1,1,1,1,1,1,,
Ursa Major	3.97	97.3	7.0	-2.04	0.56	295	7.32	8.32	1,1,1,2,2,1,,
Ursa Major II	3.70	34.7	5.6	-2.13	0.68	139	6.80	7.80	1,1,1,2,2,1,,
Ursa Minor	5.53	76.0	9.5	-2.04	0.48	405	7.73	8.73	1,1,1,2,2,1,,
William I	3.08	45.0	4.0	-1.40	0.40	33	5.89	6.89	1,1,1,2,2,1,,

Table 3.1: Physical quantities of the observed MW satellites that are used in the analysis. From left to right: Galaxy name, stellar mass, heliocentric distance, velocity dispersion, mean stellar metallicity, scatter of stellar metallicity, half light radius, halo mass with in 1.8 R_{half}, virial mass estimate. Refereces: (1) Simon (2019) and the references therein, (2) SAGA database (Suda et al., 2008), (3) Chiti et al. (2022), (4) Walker et al. (2007), (5) Muñoz et al. (2006). Note that the stellar mass is derived from V-band magnitude assuming stellar-to-light ratio of 1 and the halo mass with in 1.8 R_{half} is derived from Eq. 3.1. If there is no reference for the virial mass, we simply adopt $M_{\mathrm{vir}} = 10 M_{\mathrm{halo}}(< 1.8 R_{\mathrm{half}})$.

Note that the Small Magenllanic Cloud (SMC) and the Large Magellanic Cloud (LMC) are excluded in this analysis because there is no implementation of Type Ia Supernovae in A-SLOTH, which is required to explain the chemical features of SMC and LMC (Tsujimoto et al., 1995; Rolleston et al., 2003; Van der Swaelmen et al., 2013). In addition, we do not consider Leo T in the sample because it is located at > 400 kpc from the MW and the merger trees that we use only consider galaxies within the virial radius (~ 300 kpc) of the MW as satellites (Sec. 3.2.2). Finally, we apply a selection function to the galaxies based on their heliocentric distances and V-band absolute magnitudes (Koposov et al., 2009),

$$\log_{10}(D_{\odot}/1\mathrm{kpc}) < 1.1 - 0.228 M_{\mathrm{V}}, \tag{3.2}$$

to account for the observational incompleteness and to make fair comparison with the simulation.

3.2.2 Simulated MW satellites

We generate simulated MW satellites by running the fiducial model of A-SLOTH (Hartwig et al., 2022; Magg et al., 2022). We briefly summarise the model here. A-SLOTH is a semi-analytic model that takes dark matter merger trees as input. It assigns the baryonic content inside the haloes based on the included physical models. The physical processes include stochastic star formation of metal-free and metal-poor stars, kinematic and chemical feedback from Type II SNe and Pair instability SNe, tracing of elemental abundances of the SNe yields in the ISM and individual stars. We utilise 30 dark matter merger trees from the *Caterpillar* project (Griffen et al., 2016). Note that in the *Caterpillar* project, they only consider galaxies within 300 kpc from the MW as satellites. We apply the same selection function as in Sec. 3.2.1 to filter out small, distant galaxies.

Since the location of the Sun is not known from the dark matter only simulation, we randomly pick the solar position in the MW at a radius of 8.5 kpc (Koposov et al., 2009) and compute the the distance to the Sun for A-SLOTH simulated satellites with

$$D_{\odot} = \sqrt{8.5^2 + D_{\mathrm{MW}}^2 - 2 \times 8.5 \times D_{\mathrm{MW}} \times \cos(\phi)}, \tag{3.3}$$

where D_{MW} is the distance to the MW centre (in kpc) from the simulations, $\cos(\phi)$ is a random number uniformly distributed between -1 and 1, and ϕ is the angle between the vectors from the MW centre to Sun and to the satellite. We only consider satellites with stellar masses $< 10^8 M_\odot$ since we do not aim to compare with SMC and LMC. Due to the uncertainty in the solar position, we determine the final p-value of our fiducial model by running the analysis 100 times and take the geometric mean of these 100 p-values as the final p-value.

3.2.3 Unsupervised clustering algorithm

The fiducial unsupervised clustering that we use is the Agglomerative clustering. Agglomerative is a bottom-up hierarchical clustering algorithm. It starts by pairing the data points and then merge the pairs into clusters, eventually leading to a tree-like diagram, the dendrogram (Pedregosa et al., 2011). In principle, the algorithm does not aim to find “n clusters”, therefore, a pre-assigned number of clusters is not required. When the user assigns the number of clusters they want to find, the algorithm stops the merging when the number of clusters is reached. Data points are then returned with labels, indicating which cluster they belong to. We discuss other unsupervised clustering algorithms and the dependence of the result on the number of clusters in Sec. 3.3.

3.2.4 Goodness of fit

Once the clusters are found by the unsupervised clustering algorithm, we construct a contingency table that shows how many observed galaxies and simulated galaxies are assigned to the clusters. In Table 3.2, we show an example. There are two subsets with uneven sizes drawn from two Gaussian distributions, which are separated by $1\,\sigma$. We apply different unsupervised clustering algorithms to find 4 clusters. The actual numbers of data points from each subset that are assigned to the clusters are listed.

To determine the p-value from the contingency table, there is the Pearson’s chi-squared test (Pearson, 1916). It computes the differences between the expected values and the actual outcome. The difference then corresponds to a p-value. There is no limitation on data dimensionality to apply the Pearson’s chi-squared test. However, one has to make sure that the expected frequency is larger than 5. It is therefore not suitable to use the Pearson’s chi-squared test when the number of data points is small. Since we aim to compare two datasets in high dimensional space and there are only a handful of observed MW satellites, it is likely that there are very few observed MW satellites in the clusters, leading to small expected frequencies. Therefore, we decide to use the Fisher-Freeman-Halton exact test (Fisher, 1934; Freeman and Halton, 1951), as the fiducial test. It computes the probability of

KMeans	Cl. 1	Cl. 2	Cl. 3	Cl. 4	**p-value**
Small subset	22	0	7	1	1.33×10^{-7}
Large subset	1668	1606	1398	1298	
Agglomerative					**p-value**
Small subset	8	22	0	0	3.85×10^{-8}
Large subset	2203	1469	1210	1088	
Spectral					**p-value**
Small subset	23	0	6	1	1.04×10^{-5}
Large subset	2311	1643	1050	966	
BIRCH					**p-value**
Small subset	29	0	0	0	$5.93\ \times10^{-9}$
Large subset	2572	2526	712	160	

Table 3.2: Exemplary contingency tables: we draw two subsets from two 2D Gaussian distributions and apply four different unsupervised clustering algorithms to find four clusters. The underlying Gaussian distributions are separated by $1\,\sigma$. The listed p-values are computed with the null hypothesis that both subsets are drawn from the same distribution. All of the unsupervised clustering algorithms yield small p-values and allow us to (correctly) reject the null hypothesis.

the observed outcome (the contingency table) based on the ratio of the sizes of the two datasets. For example, in Table 3.2, the size ratio of the Small subset to the Large subset is 30:5570. The KMeans clustering assigns 0 data points from the Small subset to Cluster 2. It is expected that the probability of observing this is small, which leads to a small p-value. The Fisher-Freeman-Halton exact test is not dependent on the number of data points in each cluster and has no limitation of data dimensionality.

If the two datasets do not come from the same underlying distributions (whether it's Gaussian-like distribution or the real data), we expect the unsupervised clustering algorithm to assign data points from different subsets to different clusters and a low p-value from the Fisher-Freeman-Halton exact test. This is illustrated in Table 3.2.

3.3 Results

In this section, we first show results from test cases where we use datasets sampled from Gaussian distributions to show that our method works. Next we present the main results from our analysis: the p-value of our fiducial model where we consider all MW satellites in 30 *Caterpillar* trees as one dataset (the Ensemble) and the p-values where we consider MW satellites in individual *Caterpillar* trees as individual datasets. We compare results from different unsupervised clustering algorithms and discuss the dependence of our results on the number of clusters and justify our choice of fiducial value.

3.3.1 Application to Gaussian distributions

To illustrate that our method can distinguish good models from bad models, we test it with two-dimensional Gaussian distributions first. Most importantly, we are interested in the dependence of the p-value on the number of clusters. In Fig. 3.1 we show p-value vs. the number of clusters for three test cases. In case 1, we sample 2 subsets from two identical two-dimensional Gaussian distributions. In case 2 (3), we shift one of the Gaussian distributions by 0.5 (1.0) σ before we sample data points from it. Subset 1 has 30 data points and subset 2 has 5570 data points, which is roughly the ratio of observed satellites to simulated satellites that we will use later.

1. **Different unsupervised algorithms**

   Here we compare different unsupervised clustering algorithms: KMeans, Agglomerative hierarchical clustering, Spectral clustering, and Balanced Iterative Reducing and Clustering using Hierarchies (BIRCH).

   We briefly summarise the concept in these algorithms: in KMeans, the user assigns the desired number of clusters. The algorithm assigns the centres of the clusters and iterates to minimise the variance within each cluster. In Agglomerative hierarchical clustering, each data point starts as an individual clusters and clusters are then merged based on the distance between them. Spectral clustering first computes the similarity matrix, which estimates the similarity between the data points from the original input data. It then clusters the data points with higher similarities using existing methods such as KMeans. BIRCH does not use the distances in the original parameter space but first builds clustering features (CFs) for the input data. These CFs are then organised into a height-balanced CF tree. It then applies the Agglomerative algorithm to cluster the leaves in the CF trees. The description of these unsupervised clustering algorithms and their usage can be found in Pedregosa et al. (2011).

   From Table 3.2, we observe that KMeans finds clusters with even sizes, whereas BIRCH finds clusters with the most uneven sizes. The p-values obtained from these four clustering algorithms range from 10^{-5} to 10^{-9}. Although the range in values is large, all of the p-values are sufficiently small such that we can reject the null hypothesis that the data come from the same underlying distribution. Although KMeans is the easiest-to-understand algorithm, it has some limitations. KMeans is not good at handling outliers or identifying clusters with non-convex shapes and there is an assumption of the number of clusters to be found. Therefore, as mentioned in Sec. 3.2.3, we choose Agglomerative as the fiducial clustering algorithm and apply it to our data.

2. **Dependence of p-value on the number of clusters**
   The four unsupervised algorithms all allow or require a user-defined number of clusters. Here we show the dependence of the p-value on the number of clusters. When we draw the subsets from two identical Gaussian distributions (case 1), the p-values are similar regardless of the number of clusters. When the Gaussian distributions are separated by 0.5 σ, we observe a small decrease in the p-value when the number of cluster increases from 2 to 3, but the value stays almost constant afterwards. When the Gaussian distributions are separated by 1.0 σ, the decrease in p-value continues until 5 clusters and we start to observe distinctive p-values from the 4 unsupervised cluster algorithms. At $1\,\sigma$ apart, our method returns p-values below 0.01 which gives us confidence to reject the null hypothesis that the two subsets come from the same underlying distribution. Ideally, the p-value should be independent of the number of clusters. However, if the number of clusters is small, it is likely that most of the data points are in any case assigned to only one or two of the clusters, which could lead to a p-value that is biased towards the higher value. Thus, we choose 5 clusters as the fiducial value.

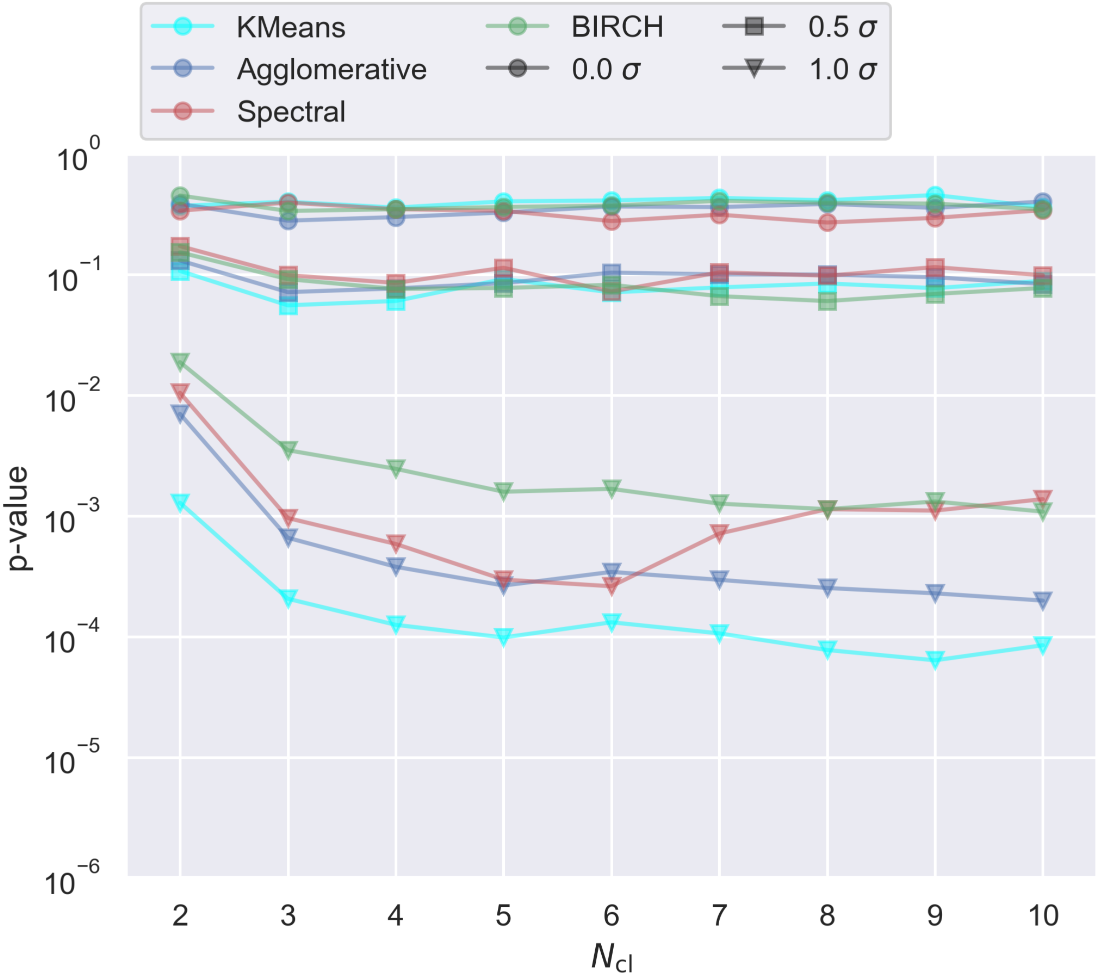

Figure 3.1: p-value vs. number of clusters with different unsupervised clustering algorithms. There are three test cases: In case 1, we draw two subsets from two identical Gaussian distributions. In case 2 (3), we shift one of the Gaussian distributions by 0.5 (1.0) σ before sampling the subsets. Subset 1 has 30 data points and subset 2 has 5570 data points, which is roughly the ratio of observed MW satellites to simulated satellites. The colours indicate different unsupervised clustering algorithms. The circles, squares, and triangles show results from case 1, 2 and 3 (0, 0.5, and 1.0 σ), respectively.

3.3.2 Clustering result and the p-value from our fiducial model

We show an example of the clustering result from our A-SLOTH fiducial model in Fig. 3.2. All simulated galaxies from 30 *Caterpillar* trees are considered (the Ensemble). The data in each dimension is normalised before applying the Agglomerative clustering with 5 clusters. The clustering result is projected onto the $\langle[\mathrm{Fe/H}]\rangle$-$M_*$ space and the mean values are shown in bold font. Galaxies that are assigned to different clusters are shown with different colours. The observed and the A-SLOTH simulated satellites are shown with squares and circles, respectively.

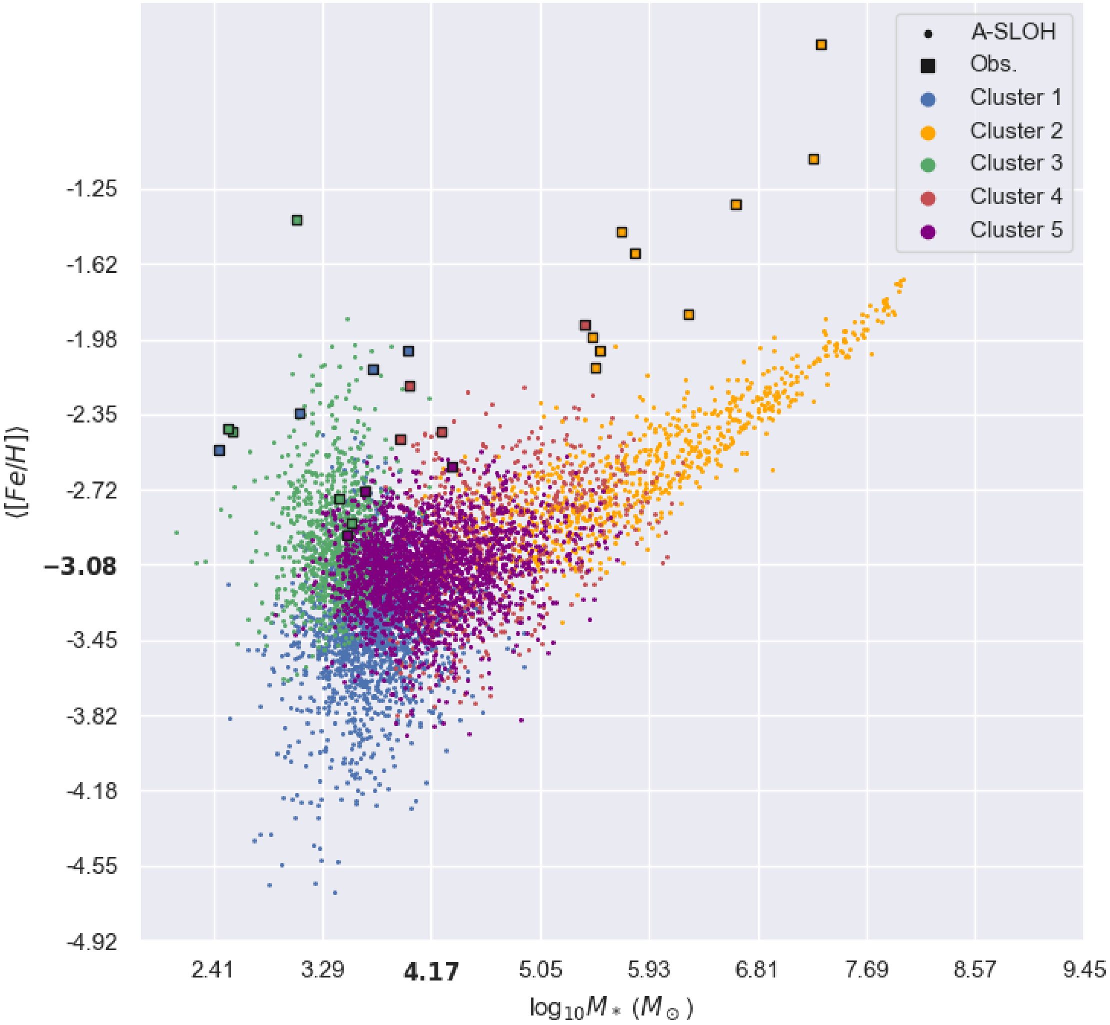

Figure 3.2: An example of unsupervised clustering from the fiducial model of A-SLOTH and the observed satellites, which is projected onto the $\langle[\mathrm{Fe/H}]\rangle$-$M_*$ space. The data is normalised in each dimension before we apply the unsupervised clustering and the means are shown in bold font. In this analysis we use Agglomerative with 5 clusters. Galaxies that are classified in different clusters are plotted with different colours. Observed MW satellites are shown in squares and A-SLOTH simulated MW satellites are shown in circles. The p-value for this example is $10^{-2.2}$.

As mentioned in Sec. 3.2.2, we run the same analysis 100 times to take into account of the randomness in the solar position and obtain 100 p-values. We compute the geometric mean of the 100 p-values that we obtain with the Ensemble and take it as the final p-value for our fiducial model, which is $10^{-3.5\pm1.4}$. In Fig. 3.3, we show the mean p-values with 1 standard deviation of 30 *Caterpillar* trees individually along with the p-value from the Ensemble. We find that the p-values from individual *Caterpillar* trees span a wide range. For example, in one specific run for Tree H1631582, the algorithm finds two clusters that only consist of the simulated galaxies (Fig. 3.4), which leads to a p-value of $10^{-9.6}$. This differences of the p-values from individual *Caterpillar* trees indicate that some *Caterpillar* trees are more similar to the MW than the others. Further analysis of the merger histories of the individual *Caterpillar* trees with high p-values could potentially tell us more about the merger history of the MW.

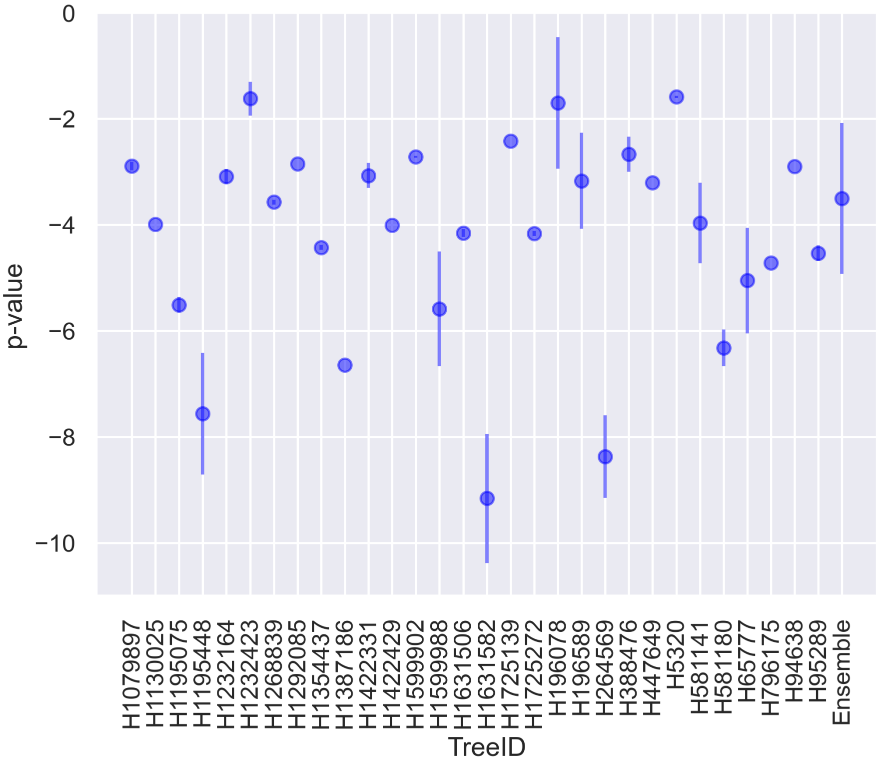

Figure 3.3: The p-values from 30 *Caterpillar* trees as individual dataset and the p-value from the Ensemble (data from 30 trees combined before conducting the analysis). Mean and 1 standard deviation from 100 runs of the analysis are shown with error bars.

Similar to Sec. 3.3.1, we test the dependence of the p-value on the number of clusters and different unsupervised clustering algorithms. The results are shown in Fig. 3.5. We observe a decrease in the p-value as the number of clusters increases among all four algorithms. With the observed and simulated MW satellites, we do not observe a clear flattening in the p-value, compared to the test data with Gaussian distributions. The scatter across the 100 runs is the smallest with the Spectral algorithm. Nevertheless, with $N_{\rm cl} = 5$, the p-value from the Agglomerative algorithm is sufficiently low, which allows us to reject the null hypothesis that the observed satellites and simulated satellites come from the same underlying distribution.

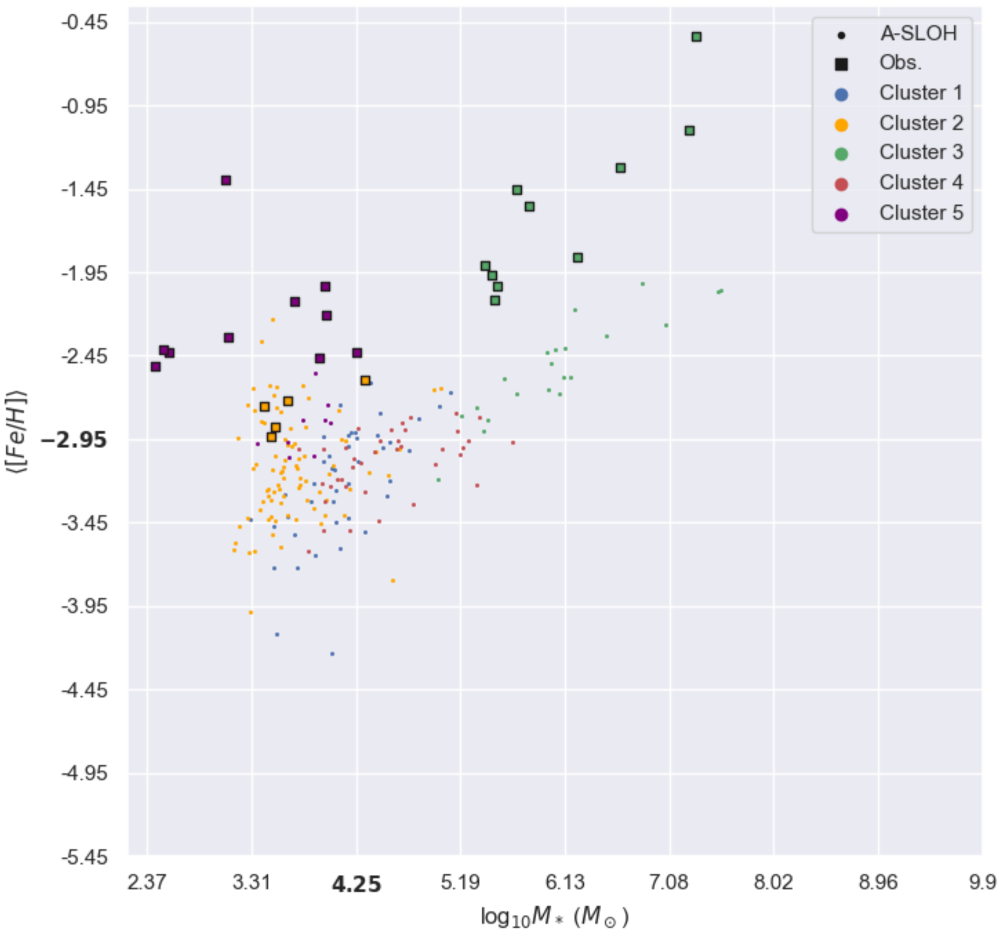

Figure 3.4: Similar to Fig. 3.2 but for one specific tree H1631582, which has the lowest p-value among the 30 *Caterpillar* trees. Two clusters only consist of simulated satellites and the p-value for this specific run is $10^{-9.6}$.

3.4 Discussion

3.4.1 Properties of the simulated MW satellites

In this section we discuss the reason why our A-SLOTH fiducial model does not reproduce the observables of interest in more details. In Fig. 3.6, we show histograms of the five physical quantities that are used in our analysis from both the observed and simulated satellites (fiducial and improved model). The A-SLOTH fiducial model reproduces the stellar mass of the MW satellites well. This is expected because we use the stellar mass of MW satellites explicitly to calibrate our model in Hartwig et al. (2022). The biggest difference between the observed MW and simulated satellites from the lies in the mean stellar [Fe/H], where we observe a difference of ∼ 1 dex. The overall distribution of the standard deviation of stellar [Fe/H] among the

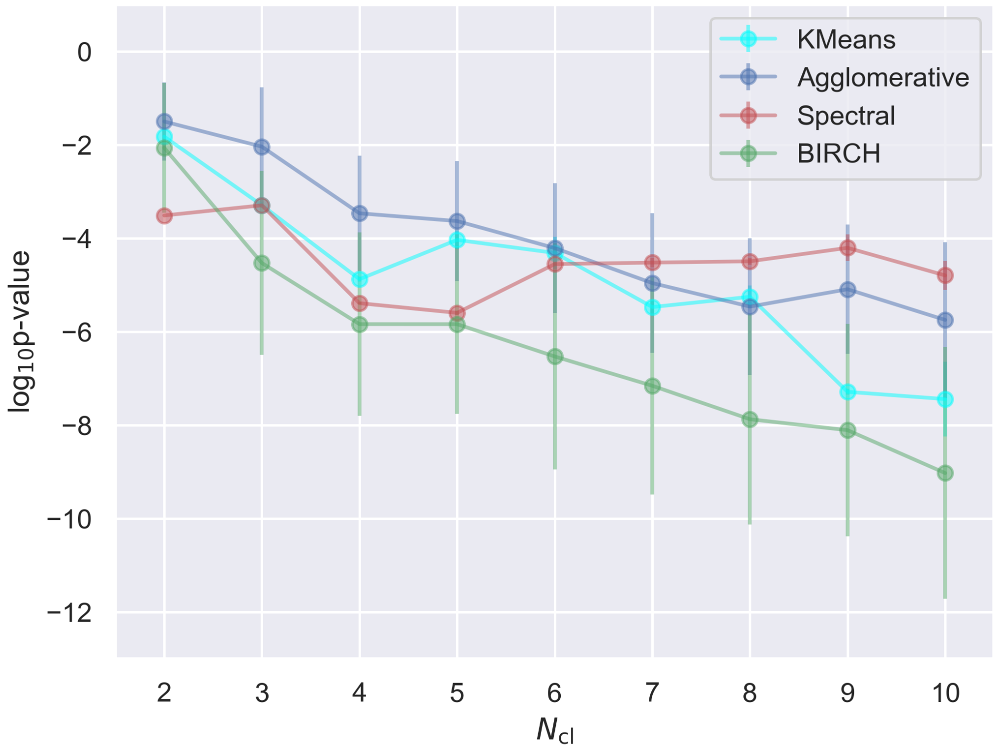

Figure 3.5: p-value v.s. number of clusters from our fiducial model. We show the mean and 1 standard deviation from 100 runs of analysis with error bars. Results from the four clustering algorithms are plotted with different colours.

satellites is similar between the observed one and the fiducial model. There are a small number of simulated satellites that have scatter larger than 1 dex among the stars.

In the fiducial model of A-SLOTH, we assume that the metals ejected from the halo mix with the inter-galactic medium (IGM) homogeneously and instantaneously. In reality, it is more likely that the metals are mixed inhomogeneously and over a longer time-scale than the time steps in the merger trees. We here implement a temporary fix where we assume that the metals ejected from the host halo of the galaxy mix with the IGM inhomogeneously and remain in proximity to the halo. The re-accreted gas therefore has a higher metallicity than simply assuming homogeneous mixing in a volume much larger than the accretion volume. In Fig. 3.7, we show the p-values from both the fiducial (blue) and improved (brown) models. The p-value from the Ensemble improves from $10^{-3.50\pm1.42}$ to $10^{-2.70\pm0.97}$.

The dynamic range of p-value is much smaller compared to Fig. 3.3. This is likely because of the improvement in our physical model. In addition, there are now 5 *Caterpillar* trees with p-values $\gtrsim 0.05$, below which is the typical value that one can reject the null hypothesis. Whereas from the fiducial model, there are only 3

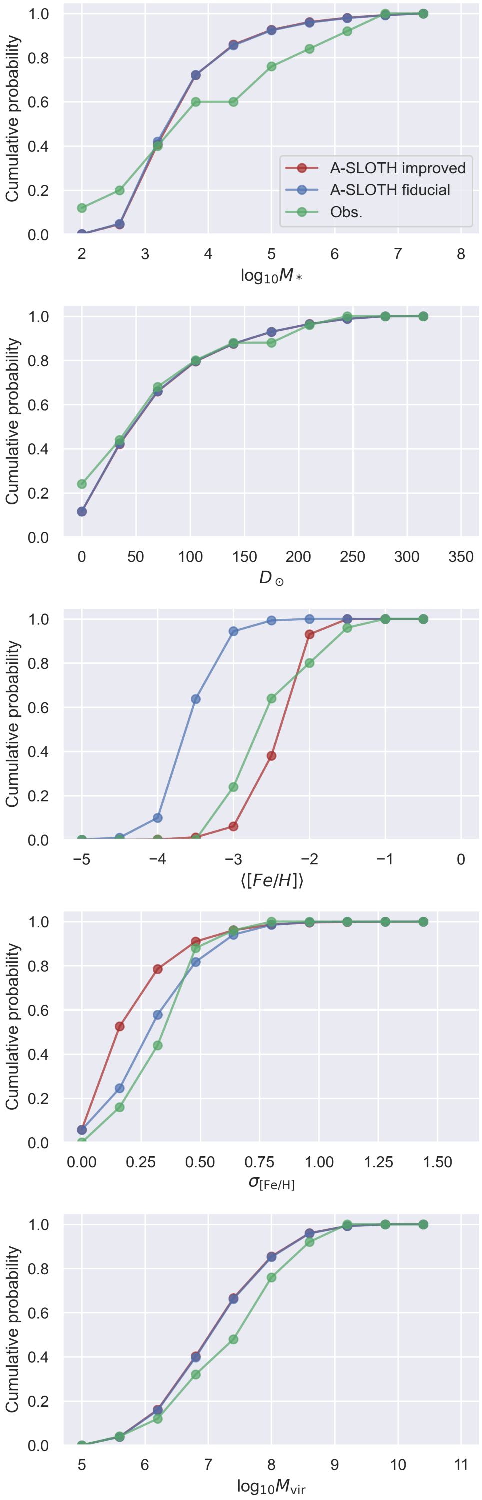

Figure 3.6: Normalised, cumulative histogram of the five physical quantities used in the analysis from our fiducial model, improved model, and the observation. From top to bottom: stellar mass, helicentric distance, mean stellar [Fe/H], standard deviation of stellar [Fe/H], and the virial mass of the halo. The observation is plotted in green, the A-SLOTH fiducial model is plotted in blue, and the improved model is plotted in brown.

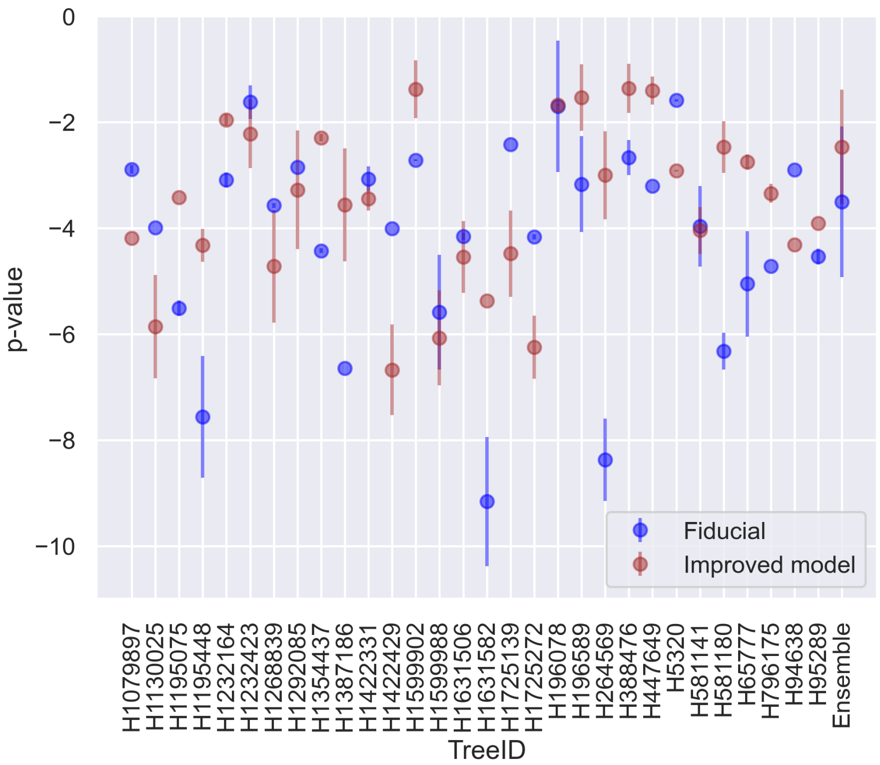

Figure 3.7: Similar to Fig. 3.3 but we add the p-values from the improved model in brown. The p-values from the fiducial model is shown in blue.

Caterpillar trees with p-values $\gtrsim 0.05$. The cumulative distribution of mean stellar metallicity $\langle[\mathrm{Fe/H}]\rangle$ from the improved model is shown in Fig. 3.6. This illustrates that the change of the p-value does reflect the improvement of the model. However, we also find some of the *Caterpillar* trees actually have lower p-values from the improved model than from the fiducial one. Despite the fact that the overall range of $\langle[\mathrm{Fe/H}]\rangle$ is now more similar between the observation and the improved model (see Fig. 3.6). The improved model still does not reproduce the cumulative distribution completely, which is why not p-values from all 30 *Caterpillar* trees improve. Note that this is only a temporary fix of the problem and we plan to further look into the metal mixing model in A-SLOTH and improve it.

3.4.2 p-value vs. properties of the MW-like galaxies

We show the p-values of individual *Caterpillar* trees vs. some properties of the main galaxies (the MWs) in the trees, e.g. the virial mass of the halo at $z = 0$, the stellar mass at $z = 0$, number of Pop II progenitors, number of satellites after applying the selection function, number of major halo growth ($\Delta M/M > 30\%$), and the redshift of most recent major halo growth in Fig. 3.8. The number of Pop II progenitors is defined to be the number of branches that have undergone Pop II star formation in the merger tree of the main galaxy. We find no clear correlation between the p-values and the virial mass, nor the stellar mass at $z = 0$, nor number of satellites. Interestingly, there is a positive correlation between the p-value and the number of Pop II progenitors in both the fiducial model and the improved model. In addition, there is a positive correlation between the number of major growths and the p-value, while these major growths occur mostly before $z = 2$.

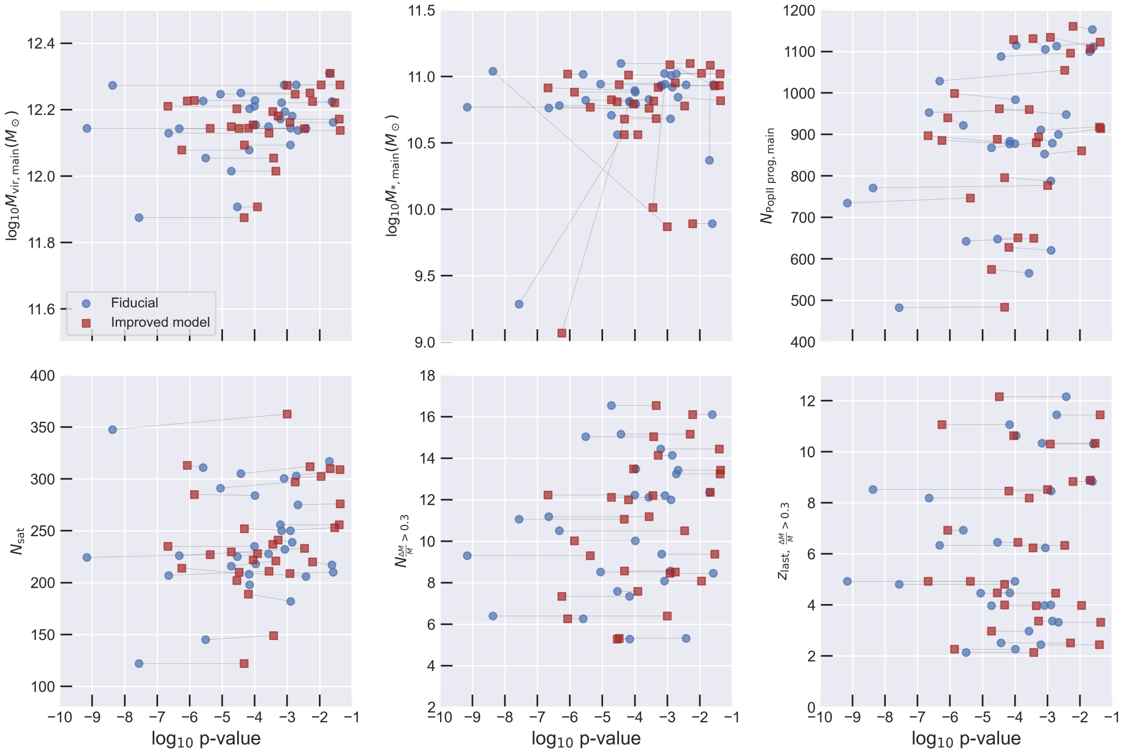

Figure 3.8: The p-values of individual *Caterpillar* trees vs. the properties of the main halo: the virial mass at $z = 0$, the stellar mass at $z = 0$, number of Pop II progenitors, number of satellites (after applying the selection function), number of major halo growths ($\Delta M/M > 30\%$), and the redshift of most recent major halo growth. Data from the fiducial model and the improved model are shown in blue and brown, respectively. The pairs of data points from the same trees are connected with thin black lines. The data is shifted slightly in the y-axis such that the pairs can be more easily identified.

3.4.3 Caveats

The stars listed in the SAGA database do not come from one survey or one group and may not be complete. As discussed in Suda et al. (2017), some stars are detected by different groups and may have different abundances in the literature. Values with the highest "priority parameter" are the fiducial values, which are the ones we take in our analysis. The resolving power, the publication year, whether ionisation state or molucules are used, the uncertainty, and the upper/lower limit are taken into account to determine the priority parameter. We also note that there are only 29 MW satellites listed in the SAGA database, while there are more than 50 MW satellites found (Muñoz et al., 2018). We aim to extend the study to individual stars in the dwarf satellites, therefore, the SAGA database is used. After applying the selection function, there are 25 observed MW satellites and an average of > 200 MW satellites from the *Caterpillar* trees. This leads to the long-standing issue with the ΛCDM simulations, the "missing satellite problem" (Kauffmann et al., 1993; Moore et al., 1999; Klypin et al., 1999), which is beyond the scope of this analysis and the physical models in A-SLOTH.

3.5 Summary

In this work, we introduce a new analysis method that helps us analyse the results from the fiducial model of our semi-analytic code A-SLOTH. Unlike other earlier studies, we are able to calibrate the model with multiple observables in one go. The observed and simulated satellites are clustered in a 5-dimensional space using the unsupervised Agglomerative hierarchical clustering algorithm. We obtain a p-value based on the clustering result from the Fisher-Freeman-Halton exact test, which tells us whether the observed and simulated satellites come from the same underlying distribution.

We first test our method with two two-dimensional Gaussian distributions to compare results from different unsupervised clustering algorithms (KMeans, Agglomerative, Spectral, and BIRCH) and study the dependence on the number of clusters. KMeans (Spectral) is the most discriminatory algorithm. However, one needs to presume the number of clusters and the pursuit of even sizes of clusters can lead to non-intuitive result. In contrary, the algorithm of Agglomerative hierarchical clustering does not depend on the number of clusters. It builds up a dendrogram and depending on the number of clusters requested, it returns the labelled data points based on the dendrogram. When the two Gaussian distributions are separated by $1\,\sigma$, we find sufficiently low p-values that allow us to reject the null hypothesis, which assumes that the two distributions come from the same underlying distribution. We observe a decrease in p-values when the number of clusters ($N_{\rm cl}$) increases. At $N_{\rm cl} \geq 5$, we start to observe converged p-values. Therefore, we adopt Agglomerative with 5 clusters as the fiducial values.

We then apply this method to the A-SLOTH simulated MW satellites and the observed ones. There are 5 physical quantities used in the analysis: the stellar mass M_*, the heliocentric distance $D_\odot$, the virial mass $M_{\rm vir}$, mean stellar metallicity $\langle$[Fe/H]$\rangle$, and the scatter among the stellar metallicity $\sigma_{\rm [Fe/H]}$. The simulation is run with the fiducial model in the semi-analytic code A-SLOTH and we use 30 *Caterpillar* trees Griffen et al. (2016). Due to the limitation of spatial information within the halo, we sample the solar position and run the analysis 100 times. The geometric mean of the 100 p-values is taken as the final p-value, which is $10^{-3.50\pm1.42}$ from our fiducial A-SLOTH model. This tells us that the simulated MW satellites from our fiducial model do not come from the same underlying distribution of the observed ones, i.e., the physical model in A-SLOTH is not good enough.

We further analyse the simulated MW satellites and find that although the fiducial model in A-SLOTH is able to reproduce the cumulative stellar mass function and the stellar mass-to-halo mass relation at $z = 0$ well, it is not able to reproduce the chemical properties of the observed MW satellites. Most of the A-SLOTH simulated satellites have stellar metallicity almost 1 dex lower than the observed ones (Fig. 3.6). This is most likely due to the assumption of homogeneous mixing when we determine the matallicity of the accreted inter-galactic medium. We implement a temporary model that assumes inhomogeneous mixing and therefore the metallicity of the accreted gas is higher than the one when we assume homogeneous mixing. The p-value from this temporary model is improved to $10^{-2.7\pm0.97}$. We further compare the p-values from individual *Caterpillar* trees with the properties of the MW-like galaxies: the virial mass at $z = 0$, the stellar mass at $z = 0$, the number of Pop II progenitors, the number of satellites after applying the selection function, on function), number of major halo growths ($\Delta M/M > 30\%$), and the redshift of most recent major halo growth. There is a positive correlations between the p-value and the number of Pop II progenitors or the number of major halo growths, whereas the p-value is uncorrelated with the other properties. This implies that the merger histories of some of the *Caterpillar* trees are more similar to the one of the MW.

This new method of comparing observational and simulated data in high-dimensional space can distinguish a good model from a bad one easily. It has no limitation on the data size or how the data distribution looks like. We aim to further improve the physical model in A-SLOTH and continue using this method. More importantly, we plan to consider stellar information such as [C/Fe], [Ba/Fe], [Eu/Fe], etc, to study the formation of individual stars of the MW satellites in our future works.

4

Location of extremely metal-poor stars in the Milky Way/M31 analogues in TNG50

This chapter is based on a paper currently in preparation. We plan to submit the manuscript to MNRAS after the submission of this thesis. I am the first author and conduct all the analyses. The text is primarily written by me. The listed coauthors provide physical insights and suggestions on the phrasing.

Abstract

We analyse the location of extremely metal-poor stars (EMP, [Fe/H] < -3) in 198 MW/M31-like systems in the TNG50 simulation. Each main galaxy is divided into four kinematically-defined morphological stellar components based on stellar circularity and galactocentric distance, namely Bulge, Disk, Warm, and Stellar halo, in addition to Satellites (with stellar mass $\geq 5 \times 10^6\, M_\odot$). According to TNG50, the Stellar halo and Satellites have the highest fraction of M_EMP-to-M_* fraction. We also observe that the Stellar halo hosts most of the EMP stars in the system, i.e., it has the highest $M_\mathrm{EMP,comp}$-to-$M_\mathrm{EMP,all}$ ratio among the components. We examine the dependence of our results on the metallicity threshold and find that Stellar halo remains the component where one most likely finds an EMP star. The results of this work provides a theoretical prediction for the location of EMP stars from both the spatial and kinematic perspectives.

4.1 Motivation

EMP stars (Beers and Christlieb, 2005) are one of the best candidates to study the first generation, metal-free stars. Due to their low metallicity, it is likely that the gas where these EMP stars formed is polluted by only a handful of or even one Pop III star (Ishigaki et al., 2014; Keller et al., 2014; Tominaga et al., 2014; Ji et al., 2015; Placco et al., 2015, 2016; Fraser et al., 2017; Ishigaki et al., 2018; Magg et al., 2018; Hartwig et al., 2018). Previous numerical simulations showed a wide range of stellar metallicity of the second generation stars. Yoshida et al. (2004) found that gas metallicity can reach to $10^{-4}Z_{\odot}$ by pair instability supernovae at $z \sim 15 - 20$ already. Smith and Sigurdsson (2007) observed a distinct transition of star formation mechanism at $10^{-3}Z_{\odot}$. Greif et al. (2010) found that the metallicity of the gas in their recollapsing galaxies reached up to [Fe/H] ~ -3. Jeon et al. (2014) showed that a single core-collapse Pop III supernova can enrich the gas to [Fe/H] ~ -4. Smith et al. (2015) found the gas having [Fe/H] ~ -5 in their externally enriched, second generation star-forming halo. Chiaki et al. (2018, 2020) reported [Fe/H] < -5 in externally enriched halos, $-5 <$ [Fe/H] $- 3$ in internally enriched halos, and an extreme case of [Fe/H] ~ -9.25.

In the past few decades, many researchers have devoted to the search of (extremely) metal-poor stars in the system of our own galaxy (Lai et al., 2008; Norris et al., 2013; Frebel and Norris, 2015; Ji et al., 2016; Hansen et al., 2020). For example, Yong et al. (2013) reported 190 metal-poor stars, where 10 of them have [Fe/H] ≤ -3.5. Roederer et al. (2014) analysed 313 metal-poor stars including 19 stars with [Fe/H] ≤ -3.5. Rare stars with [Fe/H] ≤ 6 were also discovered in recent years (Keller et al., 2014; Nordlander et al., 2019). On the other hand, large surveys help build up statistical understanding of stars in the MW. Hayden et al. (2014) analysed 20,000 stars and derived the mean metallicity map of the MW from the stellar spectroscopic APOGEE survey, where the lowest metallicity is $\sim 0.01Z_{\odot}$. Chiti et al. (2021c,a) studied the metallicity distribution function (MDF) of the MW and presented metallicities of $\sim 28,000$ stars down to [Fe/H] ~ -3.75 from the SkyMapper Southern Survey. The Pristine survey (Starkenburg et al., 2017), where the Ca H&K lines are used to infer the photometric metallicity, covers ~ 1000 deg^2 of the sky. Spectroscopic studies were followed up for some of the metal-poor stars (Youakim et al., 2017; Lardo et al., 2021) and a metallicity floor of [Fe/H] = -4.66 (Starkenburg et al., 2018) was reached.

EMP stars are identified almost everywhere in our Galaxy. The Galactic Bulge is considered to be a potential site of possible Pop III survivors (Schlaufman and

Casey, 2014) and many very metal-poor ([Fe/H] < -2) stars have been discovered there (Howes et al., 2015; García Pérez et al., 2016; Lamb et al., 2017; Arentsen et al., 2020, 2021). Venn et al. (2020) performed spectroscopic analysis of metal-poor stars and found various types of orbital features. Some EMP stars are found to have near-circular orbits (Caffau et al., 2012; Schlaufman et al., 2018; Di Matteo et al., 2020; Sestito et al., 2020). Lucey et al. (2021) conducted orbital analysis on stars that are identified in the Galactic Bulge spatially and found that half of their samples have $> 50\%$ possibility of being halo stars that happen to be crossing the Galactic Bulge. The fraction of such halo stars increases with decreasing metallicity (in the range of $-3 <$ [Fe/H] < 0.5). Kielty et al. (2021) presented high-resolution spectra of 30 metal-poor stars and most of them are in the Galactic halo.

In this work, we follow Zhu et al. (2022) and employ an adapted morphological decomposition of the Galaxy, where both the spatial and kinematic information of the stars are taken into account. We then analyse the fraction of EMP stars identified in each component of MW/M31-like systems in the TNG50 simulation. Earlier, Pakmor et al. (2022) studied the locations and rates of star formation rates for low-metallicity stars ($Z < 0.1Z_\odot$) in TNG50 but did not extend their study below $z = 0.01Z_\odot$. We describe the TNG50 simulation and how the MW/M31-like systems are chosen in Secs. 4.2.1 and 4.2.2. We define morphological components of the system in Sec. 4.2.3 and show the results in Sec. 4.3. We discuss about the dependence of our results on the metallicity threshold in Sec. 4.4. Finally, we conclude this work and our findings in Sec. 4.5.

4.2 Method

In the following sections, we describe the TNG50 simulation and how the MW/M31-like systems are identified. We also explain the post-processing procedure along with the definition of morphological components in the system.

4.2.1 The TNG50 simulation

TNG50 (Nelson et al., 2019a; Pillepich et al., 2019) is the highest resolution simulation in the IllustrisTNG[1] simulation suite (Marinacci et al., 2018; Naiman et al., 2018; Nelson et al., 2019b; Pillepich et al., 2018a; Springel et al., 2018). The simulation starts at $z = 127$ and runs until $z = 0$ following the Planck Collaboration et al. (2016) cosmology ($h = 0.6774$, $\Lambda_{\Omega,0} = 0.6911$, $\Lambda_{\mathrm{m},0} = 0.3089$,

---

[1] The simulations of the IllustrisTNG project are fully publically available at https://www.tng-project.org/(Nelson et al., 2019b).

$\Lambda_{\mathrm{b},0} = 0.0486$, $\sigma_8 = 0.8159$, and $n_\mathrm{s} = 0.9667$). It has a dark matter mass resolution of $3.1 \times 10^5 M_\odot \mathrm{h}^{-1}$ and a baryonic mass resolution of $5.8 \times 10^4 M_\odot \mathrm{h}^{-1}$ with a comoving volume of $35^3 \mathrm{Mpc}^3 \mathrm{h}^{-3}$.

TNG50 is run with the moving mesh code AREPO (Springel, 2010). It includes a large number of physical processes such as primordial and metal-line cooling, heating by the extragalactic UV background, stochastic, gas-density threshold-based star formation, evolution of stellar populations represented by star particles, chemical feedback from supernovae and AGB stars, and supermassive black hole formation and feedback. The details of the model are described in Weinberger et al. (2017) and Pillepich et al. (2018b).

4.2.2 MW/M31-like systems in TNG50

To identify analogues of the MW and M31 in TNG50, we use the following criteria (Engler et al., 2021; Pillepich et al., 2021):

1. the galaxy has a stellar mass, $M_*(< 30\mathrm{kpc})$, in the range of $10^{10.5-11.2} M_\odot$,
2. its 3D minor-to-major axial ratio s of the stellar mass distribution is less than 0.45 or it appears disky by visual inspection.
3. there are no other galaxies with $M_* > 10^{10.5} M_\odot$ at a distance of less than 500 kpc,
4. the mass of the host halo is $< 10^{13} M_\odot$.

This leads to identification of 198 MW/M31-like galaxies in TNG50 at $z = 0$. For each of these galaxies, we only consider satellites that fulfill the following criteria (Engler et al., 2021):

1. it is within 300 pkpc (3D) from the main galaxy,
2. it has a stellar mass $> 5 \times 10^6 M_\odot$ within 2 times of the stellar half-mass radius.

We limit the distance of satellites to the main galaxy to reflect that the virial radii of MW and M31 are approximately 300 pkpc. Due to the mass resolution in TNG50, a minimum stellar mass of $5 \times 10^6 M_\odot$ is equivalent to resolving a galaxy with at least 63 star particles. In addition, this mass corresponds to where the bending of the stellar mass-to-halo mass relation in TNG50 starts. The bending is artificial and is caused by the mass resolution limit (See Fig. A2 in Engler et al., 2021). The number of satellites varies among the 198 MW/M31 analogues, from 0 to nearly 20 (see Fig. 3 in Engler et al., 2021).

4.2.3 Morphological decomposition with kinematics

We classify stars in the main galaxy into four components based on their circularity ϵ_z (defined below) and distance from the centre of the galaxy r_*:

1. Disk: $\epsilon_z > 0.7$ and $r_* \leq r_{\rm disk}$;
2. Bulge: $\epsilon_z \leq 0.7$ and $r_* < r_{\rm cut}$;
3. Warm: $0.5 < \epsilon_z < 0.7$ and $r_{\rm cut} \leq r_* < r_{\rm disk}$;
4. Stellar halo: $\epsilon_z \leq 0.5$ and $r_{\rm cut} \leq r_* \leq r_{\rm sys}$ plus $\epsilon_z > 0.5$ and $r_{\rm disk} < r_* \leq r_{\rm sys}$.

Here, $r_{\rm cut} = 3.5\,{\rm kpc}$, $r_{\rm disk} = 6r_{\rm disk\,scale\,length}$ is the disk radius, $r_{\rm disk\,scale\,length}$ is the disk scale length computed by Sotillo Ramos et al. (in preparation), and $r_{\rm sys} = 300\,{\rm kpc}$ is the maximum distance that we consider. In other words, we only take into account of stars that are within 300 kpc of the centre of the main galaxy. We follow Zhu et al. (2022) and adopt $r_{\rm cut} = 3.5\,{\rm kpc}$. Zhu et al. (2022) showed that the distribution of stars with $\epsilon_z < 0.5$ peaks at $< 1.5\,{\rm kpc}$ for most galaxies in TNG50 and most of the stars with $\epsilon_z < 0.5$ are at $r < 3.5\,{\rm kpc}$ (see their Fig. 3). The decomposition of the main galaxy is shown with a cartoon plot in Fig. 4.1.

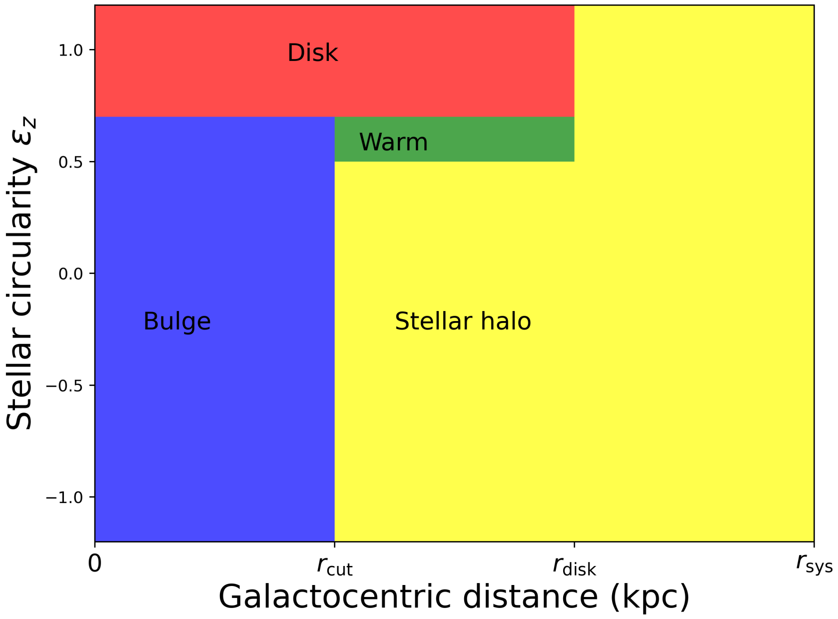

Figure 4.1: Cartoon plot of the morphological decomposition of the main galaxy (not to scale). We adopt $r_{\rm cut} = 3.5\,{\rm kpc}$, $r_{\rm disk} = 6r_{\rm disk\,scale\,length}$, and $r_{\rm sys} = 300\,{\rm kpc}$.

Below, we list the steps of how we obtain the stellar circularity $\epsilon_{\rm z}$:

1. Shift the origin to the centre of the main galaxy such that $\mathbf{r}_* = \mathbf{r}_{*,\rm ini} - \mathbf{r}_{\rm main,ini}$ and remove the bulk velocity that $\mathbf{v}_* = \mathbf{v}_{*,\rm ini} - \mathbf{v}_{\rm main,ini}$.
2. Compute the un-rotated angular momentum of each star in the main galaxy, $\mathbf{j}_* = \mathbf{r}_* \times \mathbf{v}_*$.
3. Sum up orbital angular momenta of all stars in the main galaxy $\mathbf{J}_{\rm gal} = \Sigma_i \mathbf{j}_*$.
4. Rotate the coordinate system such that the new z-axis is parallel to the angular momentum of the main galaxy; i.e. $\hat{\rm z} \parallel \mathbf{J}_{\rm gal}$.
5. Take the z-component of specific stellar angular momentum after coordinate rotation for each star in the system, $\mathbf{j}_{\rm z,rot}$.
6. Calculate the value of circular velocity for each star $v_{\rm c} = \sqrt{GM(< r_{*,\rm rot})/r_{*,\rm rot}}$, where $r_{*,\rm rot}$ is the stellar distance from the centre of the galaxy after coordinate rotation.
7. Compute the magnitude of the angular momentum that the star would have if it were in a circular orbit at the stellar distance from the centre of the galaxy, namely $j_{\rm c} = r_{*,\rm rot} v_{\rm c}$.
8. Finally, we obtain the circularity by $\epsilon_{\rm z} \equiv \mathbf{j}_{\rm z,rot}/j_{\rm c}$.

The fifth component of the system is the Satellites, where we sum up the stellar masses in all satellites that belong to the main galaxy. We discuss the scatter across individual satellites in Section 4.4. Finally, there are five components in a system, which are Disk, Bulge, Warm, Stellar Halo, and Satellites.

4.2.4 EMP stars in TNG50

The TNG50 simulation traces individual abundances of 9 species: H, He, C, N, O, Ne, Mg, Si, Fe other than the overall metallicity. We label star particles as EMP stars if their [Fe/H] is < -3. Note that the mass of star particles in TNG50 is of the order of $10^4 M_\odot$ and they therefore do not represent individual stars but star clusters that form at the same time in the same environment. All star particles that survive until $z = 0$ are considered. We compute the EMP mass and stellar mass in each component to study in which component we are more likely to find EMP stars. There are two different fractions that we use in this work. The first one is the $M_{\rm EMP}$-to-M_* fraction, where we compute with the EMP and stellar masses in each of the components in the system. The other important fraction is the EMP mass in each component to total EMP mass in the system ($M_{\rm EMP,comp}$-to-$M_{\rm EMP,all}$).

4.3 Results

Here we present the results of our analysis. We discuss direct outputs such as the spatial distribution and radial profiles of EMP stars and derived results such as the EMP fraction in different morphological components.

4.3.1 Metallicity distribution function

We show the normalised metallicity distribution functions (MDFs) for MW-mass galaxies only ($M_*(< 30{\rm kpc})/M_\odot = 10^{10.5-10.9}$, thin grey lines) and compare them with the observed MW MDF in Fig. 4.2. In the top panel, we overplot the MDF of the MW from Bonifacio et al. (2021) in magenta and the MDF from Youakim et al. (2020) in green. Youakim et al. (2020) aimed to study the metallicity distribution in the Galactic halo. They analysed ~ 80000 main sequence turnoff stars that have heliocentric distances between 6 and 20 kpc. The stellar metallicity falls in the range of $-4 <$ [Fe/H] < -1.05. Bonifacio et al. (2021) analysed ~ 140000 stars from SDSS data release 12. These stars locate at ≤ 6 kpc from the Galactic plane and have distances ≤ 14 kpc from the Galactic centre. The observed MDFs that we are comparing here do not cover all the stars of the MW, whereas we take all of the stars in the main galaxy to plot the MDFs of MW analogues in TNG50. To make a fairer comparison, we normalise the distribution with total number of stars that have $-4 \leq$ [Fe/H] < -1.05. The peak of the MDF from Bonifacio et al. (2021) is lower than the one from TNG50. Both MDFs from Bonifacio et al. (2021) and Youakim et al. (2020) show convex curves, whereas the MDF from TNG50 appears to be concave.

In addition, we compare the MDFs at different distances from the Galactic plane ($|z|$/kpc) to the MDFs in Hayden et al. (2015). Due to the observational selection bias, we cannot directly combine their MDFs and compare it to our overall MDFs. In the bottom three panels of Fig. 4.2, we plot the MDFs from Hayden et al. (2015) with coloured dashed line, where different lines represent subsets of their sample. In this comparison, the probability is normalised to the total number of stars. The overall shape of the MDFs in MW analogues are wider than the ones in Hayden et al. (2015) at $|z| \leq 1.0\,$kpc. The widths of the MDFs are more comparable only at $1.0 < |z|\,kpc \leq 2$. Overall, TNG50 is able to reproduce the MDFs at high [Fe/H] well. To compare the MDF at lower metallicity (e.g. [Fe/H] < -4), we would need a more complete observational sample.

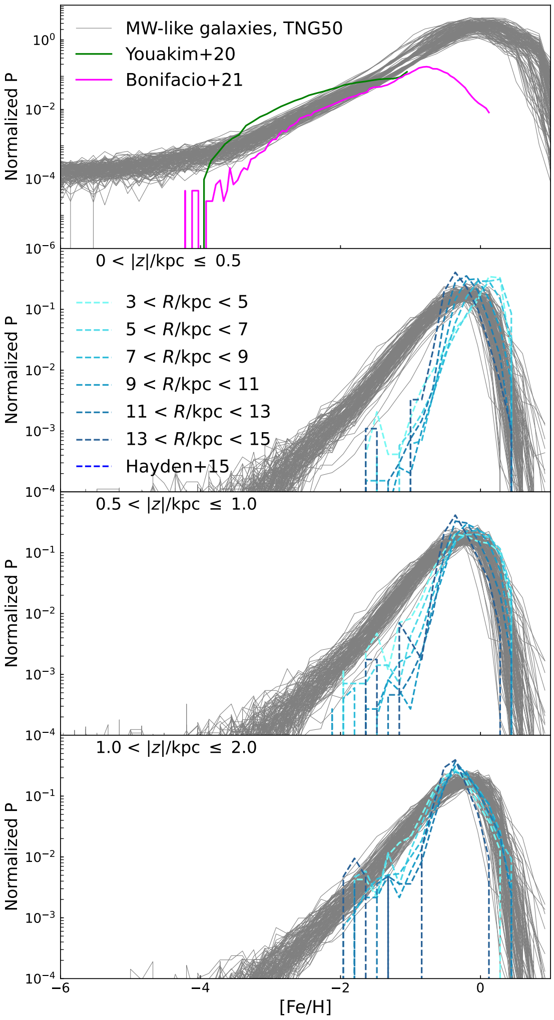

Figure 4.2: We show the metallicity distribution functions from MW-mass galaxies ($M_*(< 30\text{kpc})/M_\odot = 10^{10.5-10.9}$) in thin grey lines. In the top panel, we compare the MDFs with the ones from Youakim et al. (2020) (green) and Bonifacio et al. (2021) (magenta). The probability is normalised to the total number of stars that have $-4 <$ [Fe/H] ≤ -1.05. In the bottom three panels, we compare the MDFs of the MW analgoes in TNG50 with the one from Hayden et al. (2015). Stars are grouped at different distances from the Galactic plane ($|z|$/kpc) in order to take into account the observational bias. The probability in the bottom three panels is normalised to the total number of stars.

4.3.2 Spatial distribution of EMP stars

Spatially, most of the EMP stars are located in a central region of the system and we do not observe a clear disk. We show the spatial distributions of EMP stars from 16 MW/M31-like systems with different masses in Fig. 4.3 (edge-on projection). For comparison, we show the spatial distribution of all stars in Fig. 4.4, where structures like Bulge and Disk can be clearly seen with visual inspection.

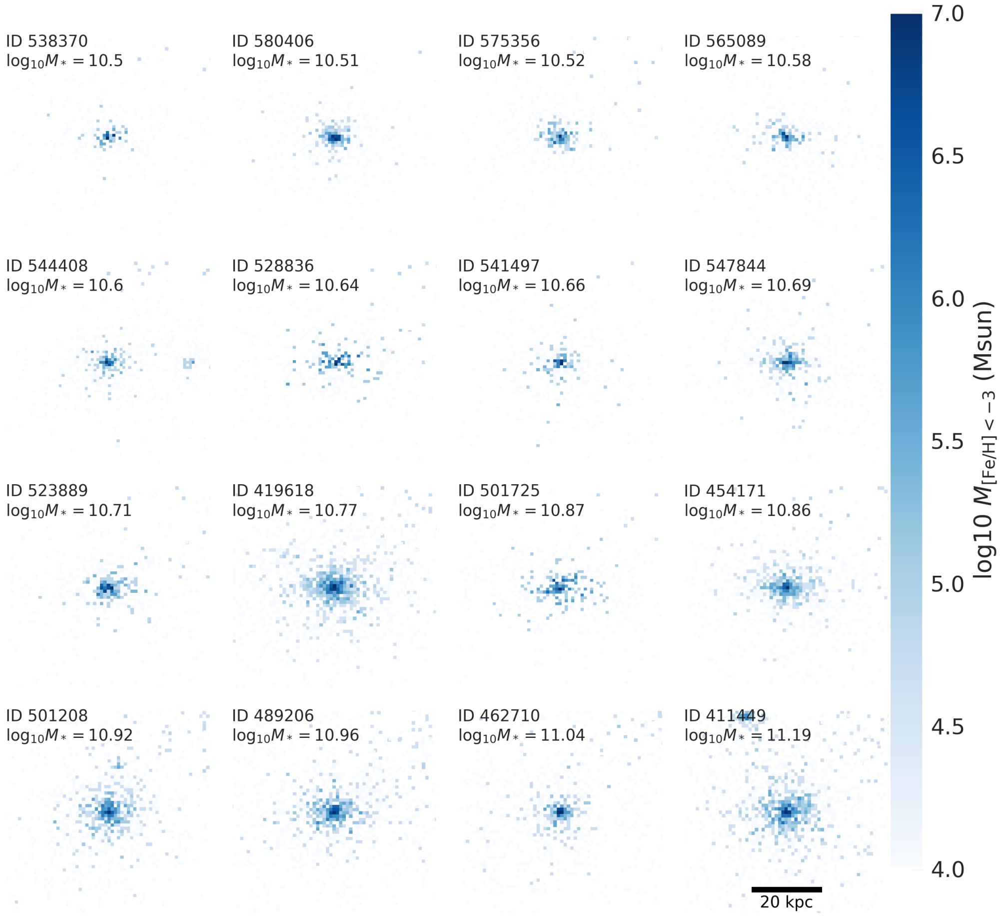

Figure 4.3: Spatial distribution of EMP stars in 16 MW/M31-like systems from the x-direction (edge-on). The colourbar shows the cumulative stellar mass in each phase-space cell and a 20 kpc scale bar is shown. The ID is an unique identifier of the galaxy in TNG50.

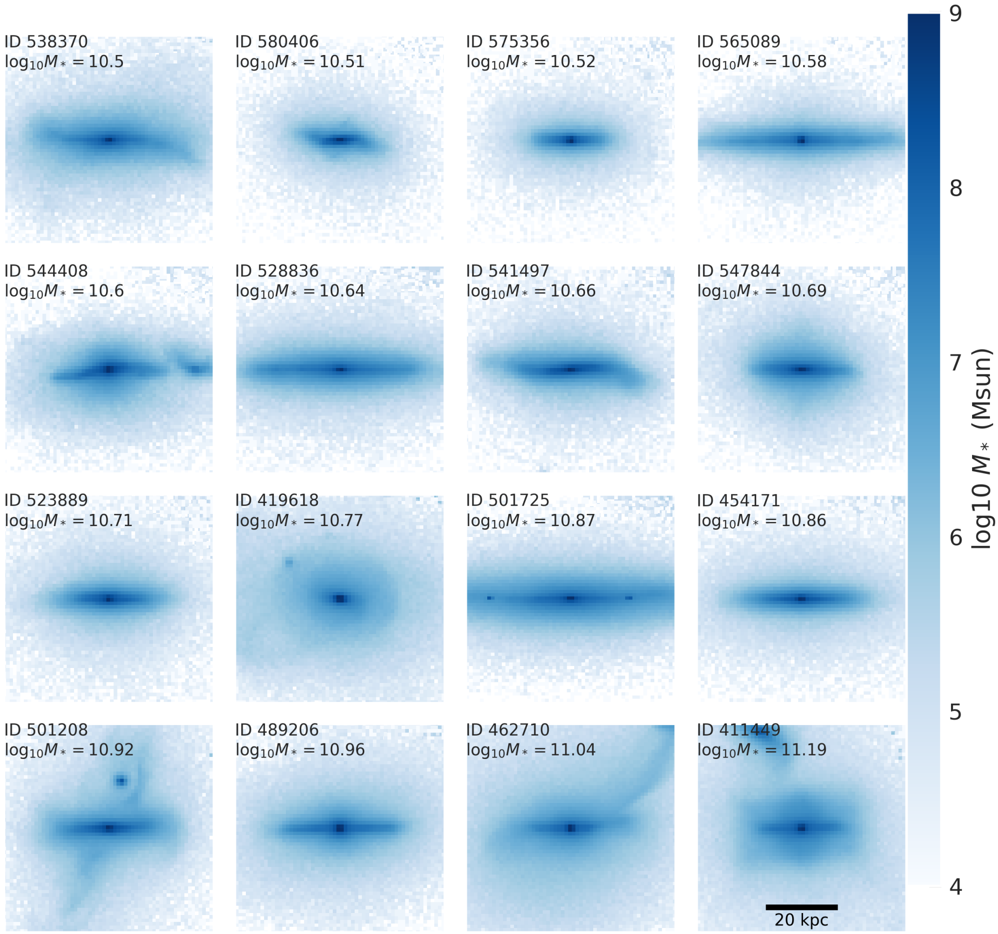

Figure 4.4: Similar to Fig. 4.3 but we show all stars in the system here.

The stellar circularity ϵ_z-galactocentric distance phase diagram is shown as an example in Fig 4.5. Note that stars in Satellites are excluded in this plot. We overplot the boundaries of different components as in Fig. 4.1 in red. For galaxies with disks from the visual inspection (Fig. 4.4), we observe over-density around $\epsilon_z = 1$ and for bulges in the galaxies, we find over-density around $\epsilon_z = 0$ and at small distances, as expected.

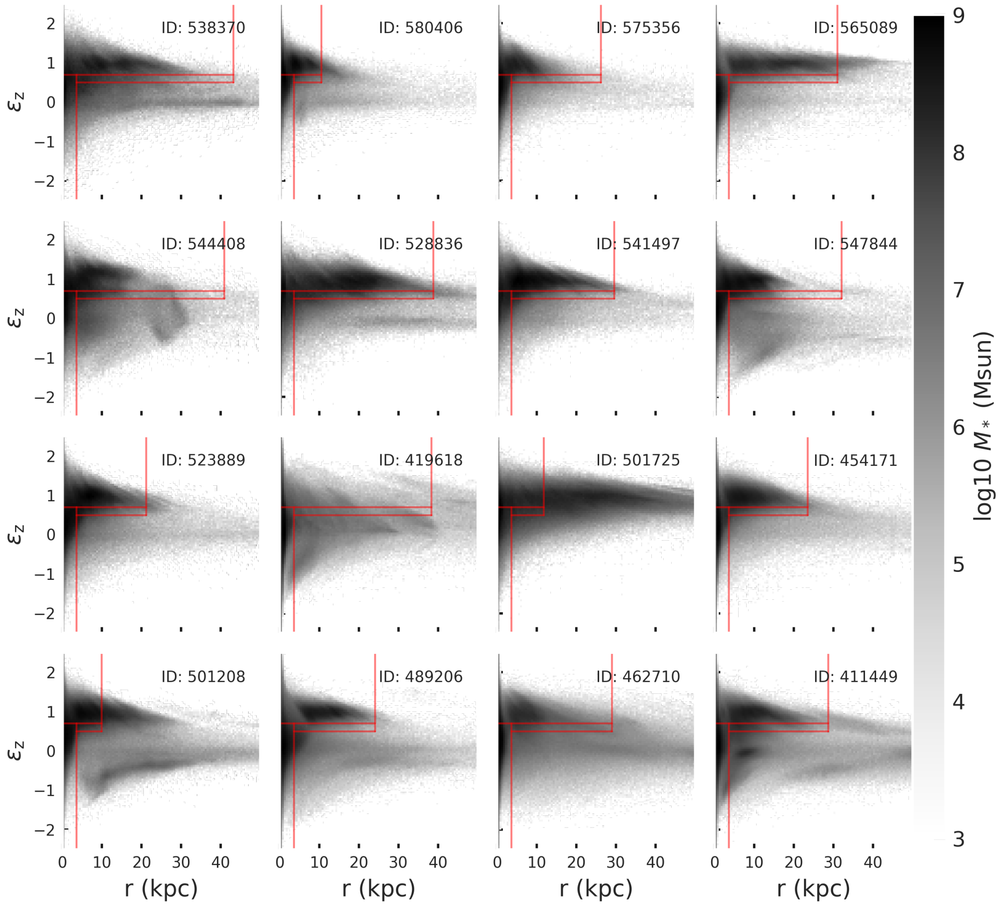

Figure 4.5: Stellar circularity ϵ_z v.s the distance from the centre of the galaxy in the same 16 MW/M31 analogues as in Fig. 4.3. The red lines show the boundaries of different components as in Fig. 4.1.

Next we show the radial distributions of all stars and EMP stars in Fig. 4.6. We divide the 198 systems into 2 groups: MW-mass where $M_*(<30\mathrm{kpc})/M_\odot = 10^{10.5-10.9}$ (McMillan, 2017) and M31-mass where $M_*(<30\mathrm{kpc}))/M_\odot = 10^{10.9-11.2}$ (Tamm et al., 2012). These two groups are plotted in red and green, respectively. In the left panel, we plot the mass density of all stars (star symbols) and EMP stars (squares) at different radii. The mean and 1 standard deviation among the 198 systems are shown. In the right panel, we show the radial profiles of the $M_{\mathrm{EMP}}(r)$-to-M_* fraction (circles) and $M_{\mathrm{EMP}}(r)$-to-$M_{\mathrm{EMP,all}}$ (triangles) at different radii. The $M_{\mathrm{EMP}}(r)$-to-M_* fraction increases as r increases and we observe a clear trend that MW-mass group shows higher $M_{\mathrm{EMP}}(r)$-to-M_* fraction than the M31-mass group. On the other hand, the fraction of EMP stars located at a certain radius to the total EMP mass ($M_{\mathrm{EMP}}(r)$-to-$M_{\mathrm{EMP,all}}$) decreases as r increases and there is no significant difference between the two groups.

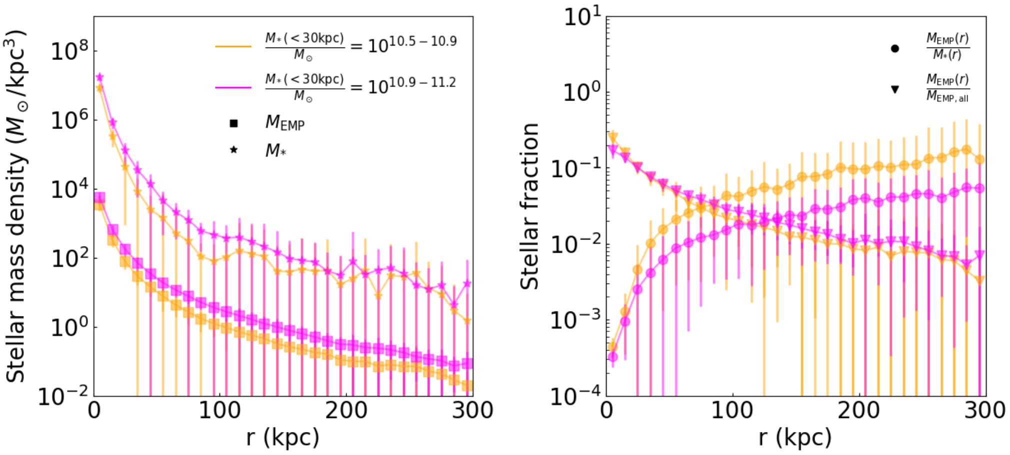

Figure 4.6: In the left panel, we show radial profiles of the total stellar mass (star symbols) and the stellar mass of EMP populations (squares) in 198 TNG50 MW/M31-like systems. In the right panel, we show radial profiles of the mean $M_{\mathrm{EMP}}(r)$-to-M_* fraction (circles) and $M_{\mathrm{EMP}}(r)$-to-$M_{\mathrm{EMP,all}}$ fraction (triangles). We plot the means along with the 1 standard deviation among the 198 systems. The orange and magenta lines show galaxies in different groups: MW-mass ($M_*(<30\mathrm{kpc})/M_\odot = 10^{10.5-10.9}$)and M31-mass ($M_*(<30\mathrm{kpc}))/M_\odot = 10^{11.9-11.2}$), respectively.

4.3.3 EMP frequency in different components

In this section we show the M_{EMP}-to-M_* fraction of each component v.s. the stellar mass of the main galaxy in the left panel of Fig. 4.7. The fraction of EMP mass in each component to total EMP mass ($M_{\mathrm{EMP,comp}}$-to-$M_{\mathrm{EMP,all}}$) is shown in the right panel of Fig. 4.7. We find that the M_{EMP}-to-M_* fraction decreases in Stellar halo and Satellites as the stellar mass of the main galaxy increases. There is no clear trend in Bulge, Disk or Warm. We observe that the Stellar halo hosts most of the EMP stars in the system while the fraction of EMP stars residing in Bulge decreases as the stellar mass of the main galaxy increases. There is no clear trend in the other three components and they have a much larger scatter among the 198 systems.

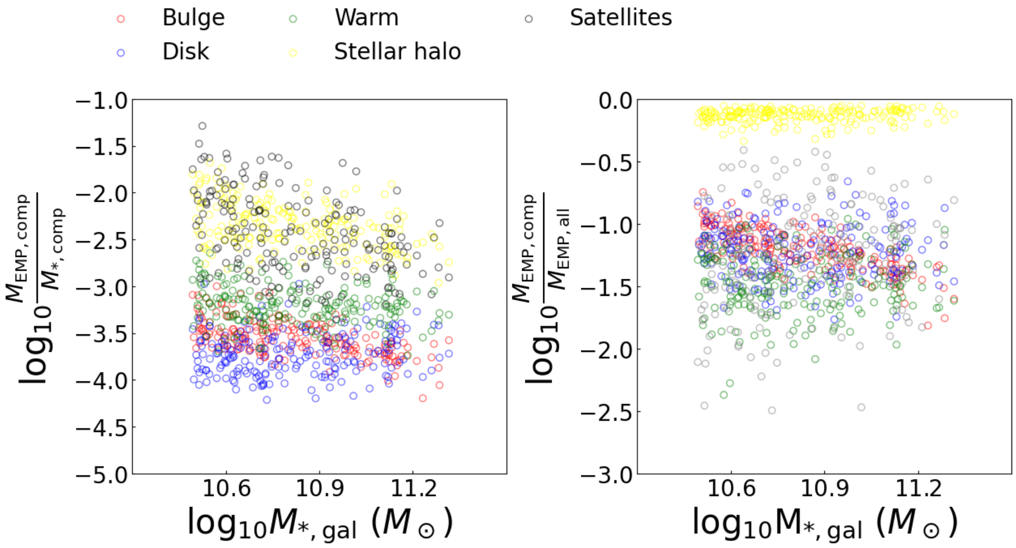

Figure 4.7: Mass fraction of EMP stars in 198 TNG50 MW/M31-like systems in different morphological components. In the left panel, we show the M_{EMP}-to-M_* fraction and in the right panel, we show the $M_{\mathrm{EMP,comp}}$-to-$M_{\mathrm{EMP,all}}$ fraction. Satellites belonged to one main galaxy is considered as one component in the system. Bulge, Disk, Warm, Stellar halo, and Satellites in each system are shown in blue, red, green, yellow, and black circles, respectively.

4.4 Discussion

As mentioned in Sec. 4.2.3, we consider all satellite stars in a system as one component. Here we show the $M_{\rm EMP}$-to-M_* fraction for individual satellites in Fig. 4.8. We find a clear trend that the fraction decreases as the stellar mass of the satellite increases. The scatter also increases as we go to higher stellar mass.

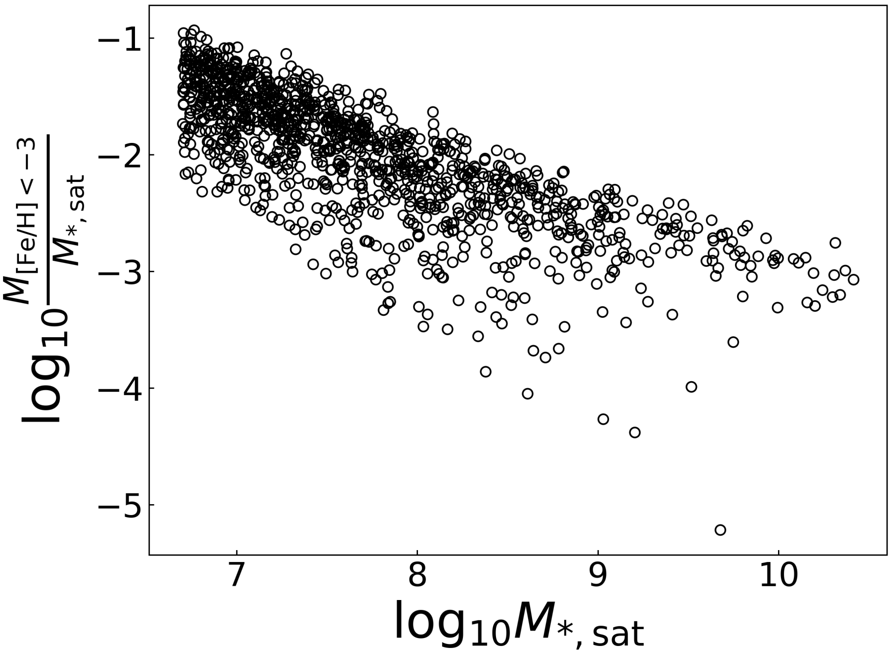

Figure 4.8: The mass fraction of EMP stars vs. the stellar mass of individual satellites for all 198 MW/M31-like systems.

Next, we study whether the $M_{\rm EMP,comp}$-to-$M_{\rm EMP,all}$ fraction changes with different definitions of EMP stars (different metallicity thresholds $[{\rm Fe/H}]_{\rm th}$). In addition to the fiducial value of $[{\rm Fe/H}]_{\rm th} = -3$, we plot three cases where $[{\rm Fe/H}]_{\rm th} = -4, -5,$ and -6 in Fig. 4.9. The Stellar halo still hosts the most metal-poor stars and the difference among the four cases is negligible. We find that the $M_{\rm EMP,comp}$-to-$M_{\rm EMP,all}$ fraction decreases in Bulge, Disk and Warm as we lower the threshold, whereas the $M_{\rm EMP,comp}$-to-$M_{\rm EMP,all}$ fraction in Satellites increases. For comparison, we perform the same analysis but increase the threshold. In Fig. 4.10, we show $M_{\rm EMP,comp}$-to-$M_{\rm EMP,all}$ fraction for $[{\rm Fe/H}]_{\rm th} = -1, -2,$ and -3. We notice that the $M_{\rm EMP,comp}$-to-$M_{\rm EMP,all}$ fraction drops from ~ 0.7 to ~ 0.6 in the Stellar halo when $[{\rm Fe/H}]_{\rm th} = -1$.

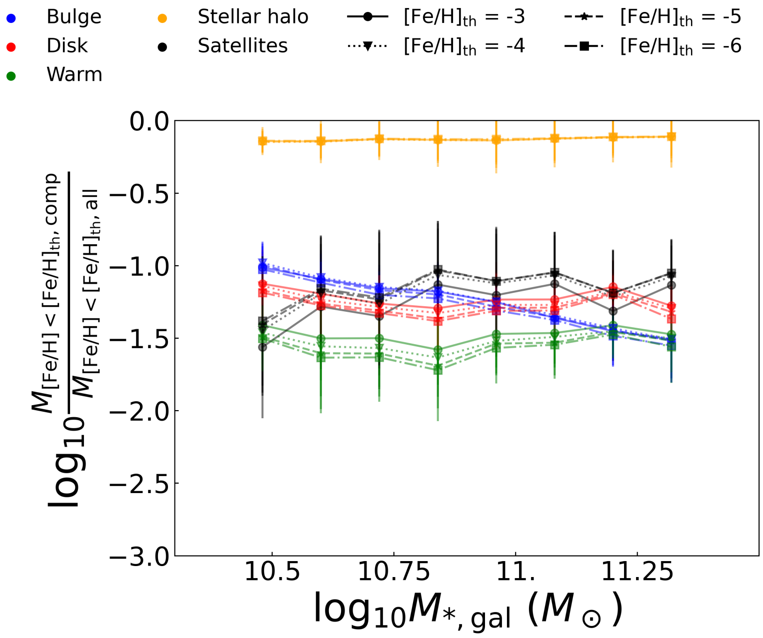

Figure 4.9: $M_{\rm EMP,comp}$-to-$M_{\rm EMP,all}$ fraction in different morphological components with different metallicity threshold $[{\rm Fe/H}]_{\rm th}$. We show $[{\rm Fe/H}]_{\rm th} = -3, -4, -5, -6$ with solid lines, dotted lines, dashed lines, and dot-dashed lines, respectively. The components are coloured as in Fig. 4.7.

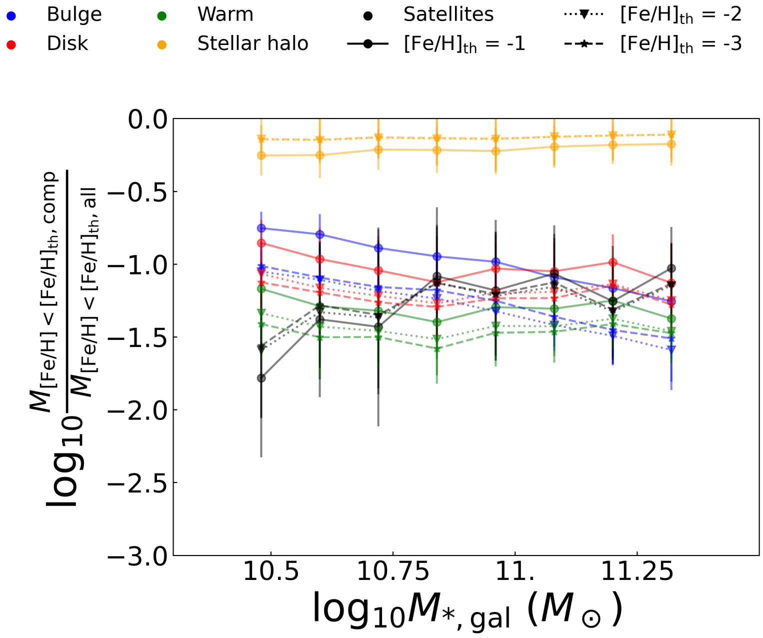

Figure 4.10: Similar to Fig. 4.9 but we show $[{\rm Fe/H}]_{\rm th} = -1, -2, -3$ with solid lines, dotted lines, and dashed lines, respectively.

Despite being the highest resolution simulation among the suite, TNG50 still cannot resolve mini-haloes ($M_{\rm halo} = 10^5 - 10^6 M_\odot$) properly. Therefore, some star formation in mini-haloes, especially at high redshift, may be ignored or delayed in the simulation. This leads to an underestimate of EMP stars by a small fraction, which is more relevant for the satellites. For the main galaxies, $M_{\rm EMP}$ can easily reach $10^7 - 10^8$, whereas stellar mass formed inside mini-haloes are on the order of $10^3 - 10^4$.

4.5 Summary

In this work, we analyse the location of EMP stars in 198 MW/M31-like systems with the TNG50 simulation. The satellites are selected to be within 300 kpc from the main galaxy and with stellar masses larger than $5 \times 10^6 M_\odot$ at $z = 0$. We decompose the main galaxies into four components, Disk, Bulge, Warm, and Stellar halo based on the stellar circularity and galactocentric distance. The fifth component of the system is the Satellites, where we sum up the stellar masses of all satellites in one MW/M31-like galaxy.

Firstly, we show the metallicity distribution functions of MW-like galaxies and compare with the existing observed MW MDF from three groups: Hayden et al. (2015) , Youakim et al. (2020), and Bonifacio et al. (2021). Overall, TNG50 is able to reproduce the observed MW MDF well at the high metallicity end. To extend the comparison to [Fe/H] < -4, we need a more complete observational sample. Next, we show the spatial distribution of EMP stars and their radial profiles. We find that EMP stars occupy the central region of the system. However, we do not observe obvious structures such as Disk or Bulge visually, compared to spatial distribution of all stars (Figs. 4.3 and 4.4). The EMP mass density decreases as the galactocentric distance increases with some bumps, which illustrate contributions from the Satellites. We also observe that the $M_{\rm EMP}(r)$-to-M_* ratio increases, whereas the $M_{\rm EMP}(r)$-to$M_{\rm EMP,all}$ ratio decreases, as the galactocentric distance increases. We further divide the 198 analogues into two groups: MW-mass ($M_*(< 30{\rm kpc})/M_\odot = 10^{10.5-10.9}$) and M31-mass ($M_*(< 30{\rm kpc})/M_\odot = 10^{11.9-11.2}$). The noticeable difference between the two groups lies in the $M_{\rm EMP}(r)$-to-M_* ratio, where this fraction is higher in the MW-mass group.

We define two important fractions in this analysis, which are the $M_{\rm EMP}$-to-M_* fraction and the $M_{\rm EMP,comp}$-to-$M_{\rm EMP,all}$ fraction, where ”comp” refers to the morphological components: Bulge, Disk, Warm, Stellar halo and Satellites. The former fraction tells us, when we look at a certain component, how much fraction of stars we expect to be EMP stars. The latter tells us when given a total EMP mass, in which component we find the most EMP stars. We show in Fig. 4.7 that the Stellar halo and the Satellites have the highest $M_{\rm EMP}$-to-M_* fraction while there is a larger scatter in the Satellites. The Stellar halo hosts most EMP stars at a given total EMP mass and is ~ 1 dex higher than all the other components. There is a non-obvious trend in the Bulges that the $M_{\rm EMP,comp}$-to-$M_{\rm EMP,all}$ fraction decreases as the stellar mass of the main galaxy increases. We further show the $M_{\rm EMP}$-to-M_* ratio of individual satellites. This ratio decreases as the stellar mass of the satellite increases and we observe larger scatter at higher masses.

Finally, we discuss about the dependence of our results on the metallicity threshold $[\mathrm{Fe/H}]_{\rm th}$ of defining EMP stars (Figs. 4.9 and 4.10). Other than the fiducial value $[\mathrm{Fe/H}]_{\rm th} = -3$, we tested 5 cases where $[\mathrm{Fe/H}]_{\rm th} = -1, -2, -4, -5, -6$. We find that the Stellar halo always hosts most of the EMP stars at a given total EMP mass. The fraction of EMP stars residing in the Stellar halo shows a noticeable decrease when the threshold is increased to $[\mathrm{Fe/H}]_{\rm th} = -1$. The $M_{\rm EMP,comp}$-to-$M_{\rm EMP,all}$ fraction decreases in the Bulge, Disk and Warm when $[\mathrm{Fe/H}]_{\rm th}$ is lower, whereas the $M_{\rm EMP,comp}$-to-$M_{\rm EMP,all}$ fraction increases in the Satellites. The results of this work provides theoretical predictions for future search of EMP stars and stars with even lower metallicity: the chance of finding EMP stars is the highest in the Stellar halo.

5

Conclusion and outlook

The aim of this thesis is to understand the formation of stars and their properties in the MW and its satellite galaxies. In Chapter 1, I describe the theoretical background of galaxy formation, star formation, kinetic and chemical feedback of stars, stellar populations and our current understanding of the MW system. In particular, I am most interested in the dwarf galaxies and the EMP stars. There are more than 50 MW satellites detected to date. However, it is believed that the observation is not complete. The increase amount of EMP star detections and detailed elemental abundances of them provide constraints to the models and improve our understanding of star formation in the early Universe.

In Chapter 2, I describe the work where I develop and implement a new Pop II SF model in the semi-analytic code A-SLOTH. This new SF model allows us to track individual Pop II stars, input the corresponding stellar feedback at appropriate time, and stellar elemental abundances. This changes the overall SF scenario, compared to older Pop II SF model in A-SLOTH. The SF used to be cluster-based and the stellar feedback is considered with IMF-average values. With the new Pop II SF model, we observe more sporadic SF events. We utilise 30 *Caterpillar* dark matter merger trees and study the SMHM relation at $z = 0$ in the MW-like systems down to the ultra-faint regime. The SMHM relation is consistent with the current observation above the completeness limit ($\sim 10^5\,M_\odot$ in stars). There is a flattening of the SMHM relation and the plateau is determined by the Pop II SF efficiency. This efficiency determines how much stellar mass forms before the stellar feedback kicks in and regulate further SF. We compare different models of LW background and baryonic streaming velocity $v_{\rm bc}$. We find that the inclusion of $v_{\rm bc}$ suppresses the star formation in low-mass ($< 10^8\,M_\odot$) haloes and therefore, the number of MW satellites with stars at $z = 0$ decreases.

To follow up on the study of dwarf galaxies in the MW system, I introduce a new method to analyse the simulated galaxies and compare them with the observed galaxies. This is discussed in Chapter 3. The idea is to use unsupervised clustering to find clusters of galaxies in high-dimensional space and obtain a goodness-of-fit (p-value) from the Fisher-Freeman-Halton test. If the simulated and the observed galaxies occupy different regions in the data space, a low p-value (< 0.05) is returned. This would reject the null hypothesis that the observed galaxies and the simulated galaxies come from the same underlying distribution. This method has no limitation on the shape of data or dimension. To analyse the results from A-SLOTH fiducial model, we collect five quantities of both the observed and the simulated MW satellites: stellar mass, virial mass, heliocentric distance, mean stellar metallicity $\langle[\mathrm{Fe/H}]\rangle$, and the scatter of stellar metallicity $\sigma_{[\mathrm{Fe/H}]}$. With this new method, we find a discrepancy between the observed MW satellites and the simulated ones. The mean stellar metallicity $\langle[\mathrm{Fe/H}]\rangle$ of A-SLOTH simulated MW satellites is 1 dex below the observed values. An ad-hoc solution is temporarily implemented in A-SLOTH and we find that the p-value improves by a factor of 2.

Lastly in Chapter 4, I study the location of EMP stars in 198 MW/M31-like systems in the hydrodynamical cosmological simulation TNG50. We decompose the system based on the spatial and kinematic information of stars into 5 components: Disc, Bulge, Warm, Stellar halo, and Satellites. Due to the resolution of dark matter and star particles in TNG50, satellites are defined to have stellar masses larger than $5 \times 10^6\,M_\odot$ at $z = 0$. We quantify two fractions: the fraction of EMP mass to stellar mass (M_EMP-to-M_*) in each component and the fraction of EMP mass in the component to total EMP mass in the system ($M_\mathrm{EMP,comp}$-to-$M_\mathrm{EMP,all}$). We find that Stellar halo has the highest M_EMP-to-M_* ratio and this ratio decreases as the stellar mass of the main galaxy increases. Most of the EMP mass in the system resides in Stellar halo ($\sim 70\%$) and $M_\mathrm{EMP,comp}$-to-$M_\mathrm{EMP,all}$ ratio of Stellar halo stays almost constant among the 198 MW/M31-like systems. In other components, there is a large scatter in the $M_\mathrm{EMP,comp}$-to-$M_\mathrm{EMP,all}$ ratio and a decrease when the stellar mass of the main galaxy increases. Only if we change the definition of EMP stars to $[\mathrm{Fe/H}] < -1$, the $M_\mathrm{EMP,comp}$-to-$M_\mathrm{EMP,all}$ ratio of Stellar Halo shows a noticeable difference. This analysis provides a theoretical prediction that it is easier to find EMP stars in the Stellar halo in MW/M31-like systems.

The newly developed star formation model in A-SLOTH has not reached its full potential. An extension of the work presented in Chapter 2 is to study the elemental abundances of EMP stars that survive to $z = 0$. By studying the assembly history of the their host haloes, we can identify which ones are directly influenced by the Pop III stars. The comparison with observation is now possible thanks to many researcher who are devoted to the expansion of individual star samples in the dwarf MW satellites. Moreover, the successful launch of the James Webb Space Telescope indicates an exciting new era. The frontier of observation is pushed to $z > 6$ for individual stars or multi-star systems (Welch et al., 2022) and to $z > 10$ for galaxies (Castellano et al., 2022; Harikane et al., 2022; Cullen et al., 2022; Furtak et al., 2022). Now we have reliable constraints directly from the high redshift Universe. This is particularly helpful since our current calibration relies on low redshift observations whereas our research interests lie in the high redshift Universe.

The advantage of semi-analytic model is that it is computationally cheap, which allows us to perform parameter studies efficiently. However, if we aim to study the stellar spatial distribution, we need to resort to hydrodynamical simulations. Therefore, in order to study the EMP stars in the UFDs, we need to improve the numerical resolution in the hydrodynamical simulations. There are some further improvements that we can consider for A-SLOTH. At the moment, we do not consider Type Ia SNe, which are less important to the SF at high redshift because of the their time-scales. However, they do influence the SF at low redshift, which the model is calibrated to. In addition, A-SLOTH currently does not include the metal production from either AGB stars or neutron star mergers. As discussed in Sec. 1.4.2, they are important to understand the peculiar abundance patterns for some metal-poor stars. The formation of supermassive black holes and feedback from the AGN are also neglected. AGN is thought to quench star formation by creating massive outflows and heating up surrounding gas. It can thus change the star formation history of our simulated galaxies. We aim to further improve the physical models in A-SLOTH to have a more complete understanding of the MW system.

Acknowledgement

First and foremost, I would like to express my gratitude toward my family, who is always supportive and understanding. Especially during the tough times in the pandemic, I would not have survived without their support. I would like to thank my two amazing supervisors, Ralf Klessen and Simon Glover, for their patient guidance in the past three years. It is an honour to be part of the group and I have learned a lot from their knowledge and experiences. Numerous people have provided valuable suggestions to polish the works that are presented in this thesis. Specifically, I would like to thank the team behind A-SLOTH: Mattis Magg, Tilman Hartwig, and Yuta Tarumi. I would like to thank Annalisa Pillepich for the opportunity to work with TNG50 data and the insightful feedback. Despite the challenges given by the pandemic, it has been a pleasure to enjoy the off-work moments with my colleagues at ITA and my IMPRS-HD fellows. The exchange of different cultural experiences is truly inspiring. Finally, I would like to thank my friends outside of astronomy: Pu-Sheng, Charlotte, Yi-Shan and Jasmine, who cheer me up from different corners of the world. Meng-Chiao, Wei-Ting, Cheng-Wei and Chia-He, who are always there when I need a distraction from work.

I am grateful for the financial support from the German Research Foundation (DFG) via the Collaborative Research Center (SFB 881, Project-ID 138713538) ’The Milky Way System’ (subprojects A1, B1, B2, B8), the HPC resources and data storage service SDS@hd supported by the Ministry of Science, Research and the Arts Baden-Württemberg (MWK) and DFG through grant INST 35/1314-1 FUGG and INST 35/1503-1 FUGG, the computing clusters ISAAC and VERA at the Max Planck Computing and Data Facility (MPCDF), and the German Space Agency (DLR) and the Federal Ministry for Economic Affairs and Climate Action (BMWK) in project ‘MAINN’ (grant number 50OO2206).

List of publications

Here I list works that I have contributions to during the course of this PhD program and are directly used in this thesis. These works have been published in or submitted to a peer-reviewed journal:

1. **L.-H. Chen**, T. Hartwig, R. S. Klessen, and S. C. O. Glover, Comparing simulated Milky Way satellite galaxies with observations using unsupervised clustering, submitted to Monthly Notices of the Royal Astronomical Society, Aug. 2022

2. **L.-H. Chen**, M. Magg, T. Hartwig, S. C. O. Glover, A. P. Ji, and R. S. Klessen, Tracing stars in Milky Way satellites with A-SLOTH, Monthly Notices of the Royal Astronomical Society, Apr. 2022, 513, 934–950

Below are publication of works that I have contributions to but are not used in this thesis:

1. T. Hartwig, M. Magg, L.-H. Chen, Y. Tarumi, V. Bromm, S. C. O. Glover, A. P. Ji, R. S. Klessen, M. A. Latif, M. Volonteri, N. Yoshida, Public Release of A-SLOTH: Ancient Stars and Local Observables by Tracing Halos, The Astrophysical Journal, arXiv e-prints, arXiv:2206.00223

2. M. Magg, I. Reis, A. Fialkov, R. Barkana, R. S. Klessen, S. C. O. Glover, L.-H. Chen, T. Hartwig, A. T. P. Schauer, Effect of the cosmological transition to metal-enriched star-formation on the hydrogen 21-cm signal, The Astrophysical Journal, Aug. 2022, 514, 4433-4449

3. M. Magg, T. Hartwig, L.-H. Chen, Y. Tarumi, A-SLOTH: Ancient Stars and Local Observables by Tracing Halos, Journal of Open Source Software, June 2022, 7(74), 4417

Appendices

A List of commonly used acronyms

A-SLOTH	Ancient Stars and Local Observables by Tracing Haloes
CMB	Cosmic Microwave Background
EMP	extremely metal-poor
IMF	initial mass function
LW	Lyman-Werner
MW	Milky Way
MDF	metallicity distribution function
Pop III/II	Population III/II
SFR	star formation rate
SN	supernova
UFD	ultra faint dwarf
ZAMS	zero-age main-sequence

B List of softwares

A-SLOTH	Magg et al. (2022)
illustris_python	https://github.com/illustristng/illustris_python
matplotlib	Hunter (2007)
numpy	Harris et al. (2020)
pandas	Wes McKinney (2010); Reback et al. (2022)
python	Van Rossum and Drake (2009)
Scikit-learn	Pedregosa et al. (2011)
scipy	Virtanen et al. (2020)
stats in R	R Core Team (2013, 2021)

References

Abate, C., Stancliffe, R. J., and Liu, Z.-W.: 2016, *A&A* **587**, A50

Abbott, B. P., Abbott, R., Abbott, T. D., et al.: 2017, *Phys. Rev. Lett.* **119(16)**, 161101

Agarwal, B., Khochfar, S., Johnson, J. L., et al.: 2012, *MNRAS* **425(4)**, 2854

Ahn, K., Shapiro, P. R., Iliev, I. T., et al.: 2009, *ApJ* **695(2)**, 1430

Aoki, W., Beers, T. C., Christlieb, N., et al.: 2007, *ApJ* **655(1)**, 492

Aoyama, S., Hirashita, H., and Nagamine, K.: 2020, *MNRAS* **491(3)**, 3844

Applebaum, E., Brooks, A. M., Christensen, C. R., et al.: 2021, *ApJ* **906(2)**, 96

Arentsen, A., Starkenburg, E., Aguado, D. S., et al.: 2021, *MNRAS* **505(1)**, 1239

Arentsen, A., Starkenburg, E., Martin, N. F., et al.: 2020, *MNRAS* **496(4)**, 4964

Asplund, M., Grevesse, N., Sauval, A. J., and Scott, P.: 2009, *ARA&A* **47(1)**, 481

Avedisova, V. S.: 1972, *Soviet Ast.* **15**, 708

Battaglia, G. and Nipoti, C.: 2022, *Nature Astronomy* **6**, 659

Battaglia, G., Taibi, S., Thomas, G. F., and Fritz, T. K.: 2022, *A&A* **657**, A54

Beers, T. C. and Christlieb, N.: 2005, *ARA&A* **43**, 531

Beers, T. C., Preston, G. W., and Shectman, S. A.: 1992, *AJ* **103**, 1987

Behroozi, P. S., Conroy, C., and Wechsler, R. H.: 2010, *ApJ* **717(1)**, 379

Behroozi, P. S., Wechsler, R. H., and Conroy, C.: 2013, *ApJ* **770(1)**, 57

Belokurov, V., Walker, M. G., Evans, N. W., et al.: 2010, *ApJ* **712(1)**, L103

Bisnovatyi-Kogan, G. S., Zel'dovich, Y. B., and Novikov, I. D.: 1967, *Soviet Ast.* **11**, 419

Bland-Hawthorn, J., Sutherland, R., and Webster, D.: 2015, *ApJ* **807(2)**, 154

Bonifacio, P., Monaco, L., Salvadori, S., et al.: 2021, *A&A* **651**, A79

Bromm, V. and Larson, R. B.: 2004, *ARA&A* **42**, 79

Brown, T. M., Tumlinson, J., Geha, M., et al.: 2014, *ApJ* **796(2)**, 91

Bryan, G. L. and Norman, M. L.: 1998, *ApJ* **495(1)**, 80

Busso, M., Gallino, R., and Wasserburg, G. J.: 1999, *ARA&A* **37**, 239

Caffau, E., Bonifacio, P., François, P., et al.: 2012, *A&A* **542**, A51

Cain, M., Frebel, A., Ji, A. P., et al.: 2020, *ApJ* **898(1)**, 40

Calura, F., Few, C. G., Romano, D., and D'Ercole, A.: 2015, *ApJ* **814(1)**, L14

Carollo, D., Freeman, K., Beers, T. C., et al.: 2014, *ApJ* **788(2)**, 180

Castellano, M., Fontana, A., Treu, T., et al.: 2022, *arXiv e-prints* p. arXiv:2207.09436

Castor, J., McCray, R., and Weaver, R.: 1975, *ApJ* **200**, L107

Chabrier, G.: 2003, *PASP* **115(809)**, 763

Chandrasekhar, S.: 1931, *ApJ* **74**, 81

Chen, L.-H., Magg, M., Hartwig, T., et al.: 2022, *MNRAS* **513(1)**, 934

Chiaki, G., Susa, H., and Hirano, S.: 2018, *MNRAS* **475(4)**, 4378

Chiaki, G. and Wise, J. H.: 2019, *MNRAS* **482**, 3933

Chiaki, G., Wise, J. H., Marassi, S., et al.: 2020, *MNRAS* **497(3)**, 3149

Chiti, A., Frebel, A., Ji, A. P., et al.: 2018, *ApJ* **857(1)**, 74

Chiti, A., Frebel, A., Ji, A. P., et al.: 2022, *arXiv e-prints* p. arXiv:2205.01740

Chiti, A., Frebel, A., Mardini, M. K., et al.: 2021a, *ApJS* **254(2)**, 31

Chiti, A., Frebel, A., Simon, J. D., et al.: 2021b, *Nature Astronomy* **5**, 392

Chiti, A., Mardini, M. K., Frebel, A., and Daniel, T.: 2021c, *ApJ* **911(2)**, L23

Chomiuk, L. and Povich, M. S.: 2011, *AJ* **142(6)**, 197

Chon, S., Hirano, S., Hosokawa, T., and Yoshida, N.: 2016, *The Astrophysical Journal* **832(2)**, 134

Christlieb, N.: 2003, *Reviews in Modern Astronomy* **16**, 191

Conroy, C. and Wechsler, R. H.: 2009, *ApJ* **696(1)**, 620

Conroy, C., Wechsler, R. H., and Kravtsov, A. V.: 2006, *ApJ* **647(1)**, 201

Correa, C. A., Wyithe, J. S. B., Schaye, J., and Duffy, A. R.: 2015, *MNRAS* **452(2)**, 1217

Cowie, L. L., McKee, C. F., and Ostriker, J. P.: 1981, *ApJ* **247**, 908

Cullen, F., McLure, R. J., McLeod, D. J., et al.: 2022, *arXiv e-prints* p. arXiv:2208.04914

de Bennassuti, M., Salvadori, S., Schneider, R., et al.: 2017, *MNRAS* **465(1)**, 926

de Bennassuti, M., Schneider, R., Valiante, R., and Salvadori, S.: 2014, *MNRAS* **445(3)**, 3039

Dessart, L., Waldman, R., Livne, E., et al.: 2013, *MNRAS* **428(4)**, 3227

Di Matteo, P., Spite, M., Haywood, M., et al.: 2020, *A&A* **636**, A115

Dijkstra, M., Haiman, Z., Rees, M. J., and Weinberg, D. H.: 2004, *ApJ* **601(2)**, 666

Dooley, G. A., Peter, A. H. G., Carlin, J. L., et al.: 2017, *MNRAS* **472(1)**, 1060

Draine, B. T.: 2011, *Physics of the interstellar and intergalactic medium*, Princeton Univ. Press

Drlica-Wagner, A., Bechtol, K., Mau, S., et al.: 2020, *ApJ* **893(1)**, 47

Drlica-Wagner, A., Bechtol, K., Rykoff, E. S., et al.: 2015, *ApJ* **813(2)**, 109

Ekström, S., Meynet, G., Chiappini, C., et al.: 2008, *A&A* **489(2)**, 685

Engler, C., Pillepich, A., Pasquali, A., et al.: 2021, *MNRAS* **507(3)**, 4211

Erkal, D., Belokurov, V., Laporte, C. F. P., et al.: 2019, *MNRAS* **487(2)**, 2685

Errani, R., Peñarrubia, J., and Walker, M. G.: 2018, *MNRAS* **481(4)**, 5073

Ezzeddine, R., Rasmussen, K., Frebel, A., et al.: 2020, *ApJ* **898(2)**, 150

Fasano, G. and Franceschini, A.: 1987, *Monthly Notices of the Royal Astronomical Society* **225(1)**, 155

Federrath, C. and Klessen, R. S.: 2012, *ApJ* **761(2)**, 156

Ferrière, K. M.: 2001, *Reviews of Modern Physics* **73(4)**, 1031

Fialkov, A., Barkana, R., Tseliakhovich, D., and Hirata, C. M.: 2012, *MNRAS* **424(2)**, 1335

Fialkov, A., Barkana, R., Visbal, E., et al.: 2013, *MNRAS* **432(4)**, 2909

Fisher, R. A.: 1934, *Statistical Methods for Research Workers, Fifth Edision*, Oliver and Boyd, Edingburgh

Font, A. S., Benson, A. J., Bower, R. G., et al.: 2011, *MNRAS* **417(2)**, 1260

Font, A. S., McCarthy, I. G., and Belokurov, V.: 2021, *MNRAS* **505(1)**, 783

Font, A. S., McCarthy, I. G., Poole-Mckenzie, R., et al.: 2020, *MNRAS* **498(2)**, 1765

Fowler, W. A. and Hoyle, F.: 1964, *ApJS* **9**, 201

Fraser, M., Casey, A. R., Gilmore, G., et al.: 2017, *MNRAS* **468(1)**, 418

Frebel, A.: 2018, *Annual Review of Nuclear and Particle Science* **68(1)**, 237

Frebel, A. and Norris, J. E.: 2015, *ARA&A* **53**, 631

Freeman, G. H. and Halton, J. H.: 1951, *Biometrika* **38(1/2)**, 141

Friedmann, A.: 1922, *Zeitschrift fur Physik* **10**, 377

Furtak, L. J., Shuntov, M., Atek, H., et al.: 2022, *arXiv e-prints* p. arXiv:2208.05473

Gaia Collaboration, Brown, A. G. A., Vallenari, A., et al.: 2016, *A&A* **595**, A2

Gaia Collaboration, Recio-Blanco, A., Kordopatis, G., et al.: 2022a, *arXiv e-prints* p. arXiv:2206.05534

Gaia Collaboration, Vallenari, A., Brown, A. G. A., et al.: 2022b, *arXiv e-prints* p. arXiv:2208.00211

Gallart, C., Monelli, M., Ruiz-Lara, T., et al.: 2021, *ApJ* **909(2)**, 192

Galli, D. and Palla, F.: 1998, *A&A* **335**, 403

Garcia-Dias, R., Allende Prieto, C., Sánchez Almeida, J., and Ordovás-Pascual, I.: 2018, *A&A* **612**, A98

García Pérez, A. E., Allende Prieto, C., Holtzman, J. A., et al.: 2016, *AJ* **151(6)**, 144

Garrison-Kimmel, S., Boylan-Kolchin, M., Bullock, J. S., and Lee, K.: 2014, *MNRAS* **438(3)**, 2578

Garrison-Kimmel, S., Bullock, J. S., Boylan-Kolchin, M., and Bardwell, E.: 2017, *MNRAS* **464(3)**, 3108

Gould, R. J. and Salpeter, E. E.: 1963, *ApJ* **138**, 393

Greif, T. H. and Bromm, V.: 2006, *MNRAS* **373(1)**, 128

Greif, T. H., Glover, S. C. O., Bromm, V., and Klessen, R. S.: 2010, *ApJ* **716**, 510

Greif, T. H., White, S. D. M., Klessen, R. S., and Springel, V.: 2011, *ApJ* **736(2)**, 147

Griffen, B. F., Ji, A. P., Dooley, G. A., et al.: 2016, *ApJ* **818**, 10

Guo, Q., White, S., Li, C., and Boylan-Kolchin, M.: 2010, *MNRAS* **404(3)**, 1111

Haid, S., Walch, S., Seifried, D., et al.: 2018, *MNRAS* **478(4)**, 4799

Hansen, C. J., Hansen, T. T., Koch, A., et al.: 2019, *A&A* **623**, A128

Hansen, C. J., Koch, A., Mashonkina, L., et al.: 2020, *A&A* **643**, A49

Hansen, T. T., Holmbeck, E. M., Beers, T. C., et al.: 2018, *ApJ* **858(2)**, 92

Harikane, Y., Ouchi, M., Oguri, M., et al.: 2022, *arXiv e-prints* p. arXiv:2208.01612

Harris, C. R., Millman, K. J., van der Walt, S. J., et al.: 2020, *Nature* **585(7825)**, 357

Hartwig, T., Bromm, V., Klessen, R. S., and Glover, S. C. O.: 2015, *MNRAS* **447**, 3892

Hartwig, T., Ishigaki, M. N., Klessen, R. S., and Yoshida, N.: 2019, *MNRAS* **482**, 1204

Hartwig, T., Magg, M., Chen, L.-H., et al.: 2022, *arXiv e-prints* p. arXiv:2206.00223

Hartwig, T., Yoshida, N., Magg, M., et al.: 2018, *MNRAS* **478**, 1795

Hayden, M. R., Bovy, J., Holtzman, J. A., et al.: 2015, *ApJ* **808(2)**, 132

Hayden, M. R., Holtzman, J. A., Bovy, J., et al.: 2014, *AJ* **147(5)**, 116

Heger, A., Fryer, C. L., Woosley, S. E., et al.: 2003, *ApJ* **591(1)**, 288

Heger, A. and Woosley, S. E.: 2002, *ApJ* **567**, 532

Heger, A. and Woosley, S. E.: 2010, *ApJ* **724**, 341

Hidalgo, S. L., Aparicio, A., Skillman, E., et al.: 2011, *ApJ* **730(1)**, 14

Hidalgo, S. L., Monelli, M., Aparicio, A., et al.: 2013, *ApJ* **778(2)**, 103

Hirano, S. and Bromm, V.: 2017, *MNRAS* **470**, 898

Hirano, S., Hosokawa, T., Yoshida, N., and Kuiper, R.: 2017, *Science* **357(6358)**, 1375

Hirano, S., Hosokawa, T., Yoshida, N., et al.: 2015, *MNRAS* **448**, 568

Hirashita, H. and Ferrara, A.: 2002, *MNRAS* **337**, 921

Hirashita, H. and Ferrara, A.: 2005, *MNRAS* **356**, 1529

Hollenbach, D. and McKee, C. F.: 1979, *ApJS* **41**, 555

Hollenbach, D. and Salpeter, E. E.: 1970, *J. Chem. Phys.* **53(1)**, 79

Holmbeck, E. M., Hansen, T. T., Beers, T. C., et al.: 2020, *ApJS* **249(2)**, 30

Hopkins, P. F., Kereš, D., Oñorbe, J., et al.: 2014, *MNRAS* **445**, 581

Hou, K.-C., Hirashita, H., Nagamine, K., et al.: 2017, *MNRAS* **469**, 870

Howes, L. M., Casey, A. R., Asplund, M., et al.: 2015, *Nature* **527(7579)**, 484

Hummel, J. A., Pawlik, A. H., Milosavljević, M., and Bromm, V.: 2012, *ApJ* **755(1)**, 72

Hunter, J. D.: 2007, *Computing in Science & Engineering* **9(3)**, 90

Ishigaki, M. N., Tominaga, N., Kobayashi, C., and Nomoto, K.: 2014, *ApJ* **792(2)**, L32

Ishigaki, M. N., Tominaga, N., Kobayashi, C., and Nomoto, K.: 2018, *ApJ* **857**, 46

Jeans, J. H.: 1902, *Philosophical Transactions of the Royal Society of London Series A* **199**, 1

Jeon, M., Besla, G., and Bromm, V.: 2017, *ApJ* **848**, 85

Jeon, M., Bromm, V., Pawlik, A. H., and Milosavljević, M.: 2015, *MNRAS* **452**, 1152

Jeon, M., Pawlik, A. H., Bromm, V., and Milosavljević, M.: 2014, *MNRAS* **444**, 3288

Jethwa, P., Erkal, D., and Belokurov, V.: 2018, *MNRAS* **473(2)**, 2060

Ji, A. P., Frebel, A., and Bromm, V.: 2015, *MNRAS* **454(1)**, 659

Ji, A. P., Frebel, A., Chiti, A., and Simon, J. D.: 2016, *Nature* **531(7596)**, 610

Ji, A. P., Koposov, S. E., Li, T. S., et al.: 2021, *ApJ* **921(1)**, 32

Ji, A. P., Simon, J. D., Roederer, I. U., et al.: 2022, *arXiv e-prints* p. arXiv:2207.03499

Johnson, J. L., Dalla Vecchia, C., and Khochfar, S.: 2013, *MNRAS* **428(3)**, 1857

Kang, D. E., Pellegrini, E. W., Ardizzone, L., et al.: 2022, *MNRAS* **512(1)**, 617

Karakas, A. I. and Lattanzio, J. C.: 2014, *Publ. Astron. Soc. Australia* **31**, e030

Kauffmann, G., White, S. D. M., and Guiderdoni, B.: 1993, *MNRAS* **264**, 201

Keller, S. C., Bessell, M. S., Frebel, A., et al.: 2014, *Nature* **506**, 463

Kielty, C. L., Venn, K. A., Sestito, F., et al.: 2021, *MNRAS* **506(1)**, 1438

Kim, S. Y. and Peter, A. H. G.: 2021, *arXiv e-prints* p. arXiv:2106.09050

Kim, S. Y., Peter, A. H. G., and Hargis, J. R.: 2018, *Phys. Rev. Lett.* **121(21)**, 211302

Kirby, E. N., Cohen, J. G., Simon, J. D., et al.: 2017, *ApJ* **838(2)**, 83

Klessen, R. S. and Glover, S. C. O.: 2016, *Saas-Fee Advanced Course* **43**, 85

Klypin, A., Gottlöber, S., Kravtsov, A. V., and Khokhlov, A. M.: 1999, *ApJ* **516(2)**, 530

Kobayashi, C., Karakas, A. I., and Lugaro, M.: 2020, *ApJ* **900(2)**, 179

Kobayashi, C., Tominaga, N., and Nomoto, K.: 2011, *ApJ* **730(2)**, L14

Kolmogorov, A. N.: 1933, *Giornale dell'Istituto Italiano degli Attuari* **4(1)**, 83

Koposov, S. E., Belokurov, V., Torrealba, G., and Evans, N. W.: 2015, *ApJ* **805(2)**, 130

Koposov, S. E., Yoo, J., Rix, H.-W., et al.: 2009, *ApJ* **696(2)**, 2179

Kravtsov, A. and Manwadkar, V.: 2022, *MNRAS* **514(2)**, 2667

Kravtsov, A. V., Berlind, A. A., Wechsler, R. H., et al.: 2004, *ApJ* **609(1)**, 35

Kroupa, P.: 2001, *MNRAS* **322**, 231

Ksoll, V. F., Gouliermis, D., Sabbi, E., et al.: 2021a, *AJ* **161(6)**, 256

Ksoll, V. F., Gouliermis, D., Sabbi, E., et al.: 2021b, *AJ* **161(6)**, 257

Kulkarni, M., Visbal, E., and Bryan, G. L.: 2021, *ApJ* **917(1)**, 40

Lacey, C. and Cole, S.: 1993, *MNRAS* **262(3)**, 627

Lai, D. K., Bolte, M., Johnson, J. A., et al.: 2008, *ApJ* **681(2)**, 1524

Lamb, M., Venn, K., Andersen, D., et al.: 2017, *MNRAS* **465(3)**, 3536

Lardo, C., Mashonkina, L., Jablonka, P., et al.: 2021, *MNRAS* **508(2)**, 3068

Li, W., Chornock, R., Leaman, J., et al.: 2011, *MNRAS* **412(3)**, 1473

Libeskind, N. I., Carlesi, E., Grand, R. J. J., et al.: 2020, *MNRAS* **498(2)**, 2968

Licquia, T. C. and Newman, J. A.: 2015, *ApJ* **806(1)**, 96

Logan, C. H. A. and Fotopoulou, S.: 2020, *A&A* **633**, A154

Lucatello, S., Tsangarides, S., Beers, T. C., et al.: 2005, *ApJ* **625(2)**, 825

Lucey, M., Hawkins, K., Ness, M., et al.: 2021, *MNRAS* **501(4)**, 5981

Lucy, L. B. and Solomon, P. M.: 1970, *ApJ* **159**, 879

Magg, M., Hartwig, T., Agarwal, B., et al.: 2018, *MNRAS* **473**, 5308

Magg, M., Hartwig, T., Chen, L.-H., and Tarumi, Y.: 2022, *A-SLOTH: Ancient Stars and Local Observbles by Tracing Haloes*, https://doi.org/10.21105/joss.04417

Magg, M., Hartwig, T., Glover, S. C. O., et al.: 2016, *MNRAS* **462**, 3591

Manwadkar, V. and Kravtsov, A.: 2021, *arXiv e-prints* p. arXiv:2112.04511

Marigo, P., Girardi, L., Chiosi, C., and Wood, P. R.: 2001, *A&A* **371**, 152

Marinacci, F., Vogelsberger, M., Pakmor, R., et al.: 2018, *MNRAS* **480(4)**, 5113

Massey, Frank J., J.: 1951, *Journal of the American Statistical Association* **46(253)**, 68

McConnachie, A. W.: 2012, *AJ* **144(1)**, 4

McConnachie, A. W. and Venn, K. A.: 2020, *AJ* **160(3)**, 124

McMillan, P. J.: 2017, *MNRAS* **465(1)**, 76

Mokiem, M. R., de Koter, A., Vink, J. S., et al.: 2007, *A&A* **473(2)**, 603

Monelli, M., Gallart, C., Hidalgo, S. L., et al.: 2010a, *ApJ* **722(2)**, 1864

Monelli, M., Hidalgo, S. L., Stetson, P. B., et al.: 2010b, *ApJ* **720(2)**, 1225

Moore, B., Ghigna, S., Governato, F., et al.: 1999, *ApJ* **524(1)**, L19

Muñoz, R. R., Carlin, J. L., Frinchaboy, P. M., et al.: 2006, *ApJ* **650(1)**, L51

Muñoz, R. R., Côté, P., Santana, F. A., et al.: 2018, *ApJ* **860(1)**, 66

Munshi, F., Brooks, A. M., Applebaum, E., et al.: 2021, *ApJ* **923(1)**, 35

Nadler, E. O., Banerjee, A., Adhikari, S., et al.: 2021, *ApJ* **920(1)**, L11

Nadler, E. O., Wechsler, R. H., Bechtol, K., et al.: 2020, *ApJ* **893(1)**, 48

Naiman, J. P., Pillepich, A., Springel, V., et al.: 2018, *MNRAS* **477(1)**, 1206

Naoz, S., Yoshida, N., and Gnedin, N. Y.: 2013, *ApJ* **763(1)**, 27

Navarro, J. F., Frenk, C. S., and White, S. D. M.: 1996, *ApJ* **462**, 563

Nelson, D., Pillepich, A., Springel, V., et al.: 2019a, *MNRAS* **490(3)**, 3234

Nelson, D., Springel, V., Pillepich, A., et al.: 2019b, *Computational Astrophysics and Cosmology* **6(1)**, 2

Newton, O., Cautun, M., Jenkins, A., et al.: 2018, *MNRAS* **479(3)**, 2853

Nomoto, K., Kobayashi, C., and Tominaga, N.: 2013, *ARA&A* **51(1)**, 457

Nordlander, T., Bessell, M. S., Da Costa, G. S., et al.: 2019, *MNRAS* **488(1)**, L109

Norris, J. E., Yong, D., Bessell, M. S., et al.: 2013, *ApJ* **762(1)**, 28

Omukai, K.: 2000, *ApJ* **534(2)**, 809

O'Shea, B. W. and Norman, M. L.: 2008, *ApJ* **673(1)**, 14

Pakmor, R., Simpson, C. M., van de Voort, F., et al.: 2022, *MNRAS* **512(3)**, 3602

Park, J., Ricotti, M., and Sugimura, K.: 2021, *MNRAS* **508(4)**, 6176

Peacock, J. A.: 1983, *MNRAS* **202**, 615

Peacock, J. A., Cole, S., Norberg, P., et al.: 2001, *Nature* **410(6825)**, 169

Pearson, K.: 1916, *Philosophical Transactions of the Royal Society of London Series A* **216**, 429

Pedregosa, F., Varoquaux, G., Gramfort, A., et al.: 2011, *Journal of Machine Learning Research* **12**, 2825

Pillepich, A., Nelson, D., Hernquist, L., et al.: 2018a, *MNRAS* **475(1)**, 648

Pillepich, A., Nelson, D., Springel, V., et al.: 2019, *MNRAS* **490(3)**, 3196

Pillepich, A., Nelson, D., Truong, N., et al.: 2021, *MNRAS* **508(4)**, 4667

Pillepich, A., Springel, V., Nelson, D., et al.: 2018b, *MNRAS* **473(3)**, 4077

Placco, V. M., Frebel, A., Beers, T. C., et al.: 2016, *ApJ* **833(1)**, 21

Placco, V. M., Frebel, A., Lee, Y. S., et al.: 2015, *ApJ* **809(2)**, 136

Planck Collaboration, Ade, P. A. R., Aghanim, N., et al.: 2014, *A&A* **571**, A16

Planck Collaboration, Ade, P. A. R., Aghanim, N., et al.: 2016, *A&A* **594**, A13

Planck Collaboration, Aghanim, N., Akrami, Y., et al.: 2020a, *A&A* **641**, A6

Planck Collaboration, Akrami, Y., Ashdown, M., et al.: 2020b, *A&A* **641**, A7

Posti, L. and Helmi, A.: 2019, *A&A* **621**, A56

Press, W. H. and Schechter, P.: 1974, *ApJ* **187**, 425

R Core Team: 2013, *R: A Language and Environment for Statistical Computing*, R Foundation for Statistical Computing, Vienna, Austria, ISBN 3-900051-07-0

R Core Team: 2021, *R: A Language and Environment for Statistical Computing*, R Foundation for Statistical Computing, Vienna, Austria

Rahner, D., Pellegrini, E. W., Glover, S. C. O., and Klessen, R. S.: 2017, *MNRAS* **470(4)**, 4453

Rahner, D., Pellegrini, E. W., Glover, S. C. O., and Klessen, R. S.: 2019, *MNRAS* **483(2)**, 2547

Rakavy, G. and Shaviv, G.: 1967, *ApJ* **148**, 803

Reback, J., jbrockmendel, McKinney, W., et al.: 2022, *pandas-dev/pandas: Pandas 1.4.1*, https://doi.org/10.5281/zenodo.6053272

Reichert, M., Hansen, C. J., Hanke, M., et al.: 2020, *A&A* **641**, A127

Reis, I., Rotman, M., Poznanski, D., et al.: 2019, *arXiv e-prints* p. arXiv:1911.06823

Relaño, M., De Looze, I., Saintonge, A., et al.: 2022, *MNRAS*

Ricotti, M. and Gnedin, N. Y.: 2005, *ApJ* **629(1)**, 259

Ritter, J. S., Sluder, A., Safranek-Shrader, C., et al.: 2015, *MNRAS* **451(2)**, 1190

Robertson, B. E., Furlanetto, S. R., Schneider, E., et al.: 2013, *ApJ* **768**, 71

Roederer, I. U., Hattori, K., and Valluri, M.: 2018, *AJ* **156(4)**, 179

Roederer, I. U., Lawler, J. E., Den Hartog, E. A., et al.: 2022, *ApJS* **260(2)**, 27

Roederer, I. U., Preston, G. W., Thompson, I. B., et al.: 2014, *AJ* **147(6)**, 136

Rogers, H. and Pittard, J. M.: 2013, *MNRAS* **431(2)**, 1337

Rolleston, W. R. J., Venn, K., Tolstoy, E., and Dufton, P. L.: 2003, *A&A* **400**, 21

Romano, D., Calura, F., D'Ercole, A., and Few, C. G.: 2019, *A&A* **630**, A140

Rossi, M., Salvadori, S., and Skúladóttir, Á.: 2021, *MNRAS* **503(4)**, 6026

Rozwadowska, K., Vissani, F., and Cappellaro, E.: 2021, *New Astron.* **83**, 101498

Rubin, V. C., Ford, W. K., J., and Thonnard, N.: 1980, *ApJ* **238**, 471

Ruiter, A. J., Belczynski, K., and Fryer, C.: 2009, *ApJ* **699(2)**, 2026

Safarzadeh, M. and Scannapieco, E.: 2017, *MNRAS* **471(2)**, 2088

Sakari, C. M., Placco, V. M., Farrell, E. M., et al.: 2018, *ApJ* **868(2)**, 110

Salpeter, E. E.: 1955, *ApJ* **121**, 161

Salucci, P.: 2019, *A&ARv* **27(1)**, 2

Salvadori, S. and Ferrara, A.: 2009, *MNRAS* **395(1)**, L6

Salvadori, S., Skúladóttir, Á., and Tolstoy, E.: 2015, *MNRAS* **454(2)**, 1320

Sanati, M., Jeanquartier, F., Revaz, Y., and Jablonka, P.: 2022, *arXiv e-prints* p. arXiv:2206.11351

Sarmento, R., Scannapieco, E., and Pan, L.: 2017, *ApJ* **834(1)**, 23

Sawala, T., Frenk, C. S., Fattahi, A., et al.: 2015, *MNRAS* **448(3)**, 2941

Schaerer, D.: 2002, *A&A* **382**, 28

Schauer, A. T. P., Agarwal, B., Glover, S. C. O., et al.: 2017, *MNRAS* **467(2)**, 2288

Schauer, A. T. P., Glover, S. C. O., Klessen, R. S., and Ceverino, D.: 2019, *MNRAS* **484(3)**, 3510

Schauer, A. T. P., Glover, S. C. O., Klessen, R. S., and Clark, P.: 2021, *MNRAS* **507(2)**, 1775

Schlaufman, K. C. and Casey, A. R.: 2014, *ApJ* **797(1)**, 13

Schlaufman, K. C., Thompson, I. B., and Casey, A. R.: 2018, *ApJ* **867(2)**, 98

Schneider, P.: 2015, *Extragalactic Astronomy and Cosmology: An Introduction*, Springer-Verlag Berlin Heidelberg

Sedov, L. I.: 1946, *Journal of Applied Mathematics and Mechanics* **10**, 241

Sestito, F., Martin, N. F., Starkenburg, E., et al.: 2020, *MNRAS* **497(1)**, L7

Shankar, F., Lapi, A., Salucci, P., et al.: 2006, *ApJ* **643(1)**, 14

Simon, J. D.: 2019, *ARA&A* **57**, 375

Skinner, D. and Wise, J. H.: 2020, *MNRAS* **492(3)**, 4386

Smirnov, N. V.: 1939, *Bull. Math. Univ. Moscou* **2(2)**, 3

Smith, B. D. and Sigurdsson, S.: 2007, *ApJ* **661(1)**, L5

Smith, B. D., Wise, J. H., O'Shea, B. W., et al.: 2015, *MNRAS* **452**, 2822

Smoot, G. F., Bennett, C. L., Kogut, A., et al.: 1992, *ApJ* **396**, L1

Sneden, C., Cowan, J. J., and Gallino, R.: 2008, *ARA&A* **46**, 241

Sormani, M. C., Treß, R. G., Klessen, R. S., and Glover, S. C. O.: 2017, *MNRAS* **466(1)**, 407

Spitzer, L.: 1978, *Physical processes in the interstellar medium*, New York Wiley-Interscience

Springel, V.: 2010, *MNRAS* **401**, 791

Springel, V., Pakmor, R., Pillepich, A., et al.: 2018, *MNRAS* **475(1)**, 676

Stacy, A., Bromm, V., and Lee, A. T.: 2016, *MNRAS* **462**, 1307

Stacy, A., Bromm, V., and Loeb, A.: 2011, *ApJ* **730(1)**, L1

Stacy, A., Greif, T. H., and Bromm, V.: 2010, *MNRAS* **403**, 45

Starkenburg, E., Aguado, D. S., Bonifacio, P., et al.: 2018, *MNRAS* **481(3)**, 3838

Starkenburg, E., Helmi, A., De Lucia, G., et al.: 2013, *MNRAS* **429(1)**, 725

Starkenburg, E., Martin, N., Youakim, K., et al.: 2017, *MNRAS* **471(3)**, 2587

Strömgren, B.: 1939, *ApJ* **89**, 526

Suda, T., Hidaka, J., Aoki, W., et al.: 2017, *PASJ* **69(5)**, 76

Suda, T., Katsuta, Y., Yamada, S., et al.: 2008, *PASJ* **60**, 1159

Susa, H., Hasegawa, K., and Tominaga, N.: 2014, *ApJ* **792**, 32

Tamm, A., Tempel, E., Tenjes, P., et al.: 2012, *A&A* **546**, A4

Tarumi, Y., Hartwig, T., and Magg, M.: 2020, *ApJ* **897(1)**, 58

Tasitsiomi, A., Kravtsov, A. V., Wechsler, R. H., and Primack, J. R.: 2004, *ApJ* **614(2)**, 533

Taylor, G.: 1941, *Civil Reference Research Committee Report* 210(27)

Taylor, P. and Kobayashi, C.: 2015, *MNRAS* **448(2)**, 1835

Tominaga, N., Iwamoto, N., and Nomoto, K.: 2014, *ApJ* **785(2)**, 98

Torrealba, G., Belokurov, V., Koposov, S. E., et al.: 2018, *MNRAS* **475(4)**, 5085

Torrealba, G., Koposov, S. E., Belokurov, V., and Irwin, M.: 2016, *MNRAS* **459(3)**, 2370

Tseliakhovich, D., Barkana, R., and Hirata, C. M.: 2011, *MNRAS* **418(2)**, 906

Tsujimoto, T., Nomoto, K., Yoshii, Y., et al.: 1995, *MNRAS* **277(3)**, 945

Vale, A. and Ostriker, J. P.: 2004, *MNRAS* **353(1)**, 189

Van der Swaelmen, M., Hill, V., Primas, F., and Cole, A. A.: 2013, *A&A* **560**, A44

van Marle, A. J., Meliani, Z., and Marcowith, A.: 2015, *A&A* **584**, A49

Van Rossum, G. and Drake, F. L.: 2009, *Python 3 Reference Manual*, CreateSpace, Scotts Valley, CA

Venn, K. A., Kielty, C. L., Sestito, F., et al.: 2020, *MNRAS* **492(3)**, 3241

Vincenzo, F., Kobayashi, C., and Taylor, P.: 2018, *MNRAS* **480(1)**, L38

Virtanen, P., Gommers, R., Oliphant, T. E., et al.: 2020, *Nature Methods* **17**, 261

Visbal, E., Bryan, G. L., and Haiman, Z.: 2017, *MNRAS* **469(2)**, 1456

Visbal, E., Bryan, G. L., and Haiman, Z.: 2020, *ApJ* **897(1)**, 95

Visbal, E., Haiman, Z., and Bryan, G. L.: 2018, *MNRAS* **475(4)**, 5246

Visbal, E., Haiman, Z., Terrazas, B., et al.: 2014, *MNRAS* **445(1)**, 107

Walker, M. G., Mateo, M., Olszewski, E. W., et al.: 2007, *ApJ* **667(1)**, L53

Wang, G.-J., Shi, H.-L., Yan, Y.-P., et al.: 2022, *ApJS* **260(1)**, 13

Wang, W., Takada, M., Li, X., et al.: 2021, *MNRAS* **500(3)**, 3776

Weaver, R., McCray, R., Castor, J., et al.: 1977, *ApJ* **218**, 377

Weinberger, R., Springel, V., Hernquist, L., et al.: 2017, *MNRAS* **465(3)**, 3291

Weisz, D. R., Dolphin, A. E., Skillman, E. D., et al.: 2014, *ApJ* **789(2)**, 148

Weisz, D. R., Dolphin, A. E., Skillman, E. D., et al.: 2015, *ApJ* **804(2)**, 136

Welch, B., Coe, D., Zackrisson, E., et al.: 2022, *arXiv e-prints* p. arXiv:2208.09007

Wes McKinney: 2010, in Stéfan van der Walt and Jarrod Millman (eds.), *Proceedings of the 9th Python in Science Conference*, pp 56 – 61

Wetzel, A. R., Hopkins, P. F., Kim, J.-h., et al.: 2016, *ApJ* **827(2)**, L23

Whalen, D., van Veelen, B., O'Shea, B. W., and Norman, M. L.: 2008, *ApJ* **682(1)**, 49

Wheeler, C., Hopkins, P. F., Pace, A. B., et al.: 2019, *MNRAS* **490(3)**, 4447

Wheeler, C., Oñorbe, J., Bullock, J. S., et al.: 2015, *MNRAS* **453(2)**, 1305

Willman, B.: 2010, *Advances in Astronomy* **2010**, 285454

Yamasawa, D., Habe, A., Kozasa, T., et al.: 2011, *ApJ* **735(1)**, 44

Yong, D., Norris, J. E., Bessell, M. S., et al.: 2013, *ApJ* **762(1)**, 26

Yoon, J., Whitten, D. D., Beers, T. C., et al.: 2020, *ApJ* **894(1)**, 7

Yoshida, N., Bromm, V., and Hernquist, L.: 2004, *ApJ* **605(2)**, 579

Youakim, K., Starkenburg, E., Aguado, D. S., et al.: 2017, *MNRAS* **472(3)**, 2963

Youakim, K., Starkenburg, E., Martin, N. F., et al.: 2020, *MNRAS* **492(4)**, 4986

Zhu, L., Pillepich, A., van de Ven, G., et al.: 2022, *A&A* **660**, A20